Dmytro Ihorovych Solonenko

Vibrational properties of epitaxial silicene on Ag(111)

Dmytro Ihorovych Solonenko

# Vibrational properties of epitaxial silicene on Ag(111)

TECHNISCHE UNIVERSITÄT
CHEMNITZ

**Universitätsverlag Chemnitz**

**2017**

**Impressum**

**Bibliografische Information der Deutschen Nationalbibliothek**

Die Deutsche Nationalbibliothek verzeichnet diese Publikation in der Deutschen Nationalbibliografie;
detaillierte bibliografische Angaben sind im Internet über http://dnb.d-nb.de abrufbar.

# Vibrational properties of epitaxial silicene on Ag(111)

von der Fakultät für Naturwissenschaften der Technischen Universität Chemnitz genehmigte
Dissertation zur Erlangung des akademischen Grades

doctor rerum naturalium

(Dr. rer. nat.)

eingereicht durch Dmytro Ihorovych Solonenko, M.Sc.

geboren am 03. Dezember 1989 in Zhytomyr, Ukraine

Tag der Einreichung: 23. Dezember 2016

Gutachter:

    Prof. Dr. Dr. h. c. Dietrich R. T. Zahn

    Prof. Dr. Guy Le Lay

Tag der Verteidigung: 10. Juli 2017

## Bibliographische Beschreibung und Referat

Solonenko, Dmytro Igorovych

*Vibrational spectroscopy of epitaxial silicene on Ag(111)*

Technische Universität Chemnitz, Institut für Physik, Dissertation (in englischer Sprache), 2016

Die experimentellen Forschungsarbeiten zum Thema Silicen basieren auf den 2012 von Vogt *et al.* durchgeführten Untersuchungen zu dessen Synthese auf Silbersubstraten. Diese Untersuchungen lieferten die Grundlage, auf der zweidimensionales (2D) epitaktisches Silicen sowie weitere 2D Materialien untersucht werden konnten. In den anfänglichen Arbeiten konnte dabei gezeigt werden, dass sich die Eigenschaften von epitaktischem Silicen gegenüber den theoretischen Vorhersagen von frei-stehendem Silicen unterscheiden. Darüber hinaus verkomplizieren sich die experimentellen Untersuchungen dieses 2D Materials, da auf dem Ag(111) Wachstumssubstrat sechs verschiedene 2D Si Polytypen existieren. Eine detaillierte Darstellung dieser Untersuchungen findet sich in dem einführenden Kapitel der vorliegen Promotionsschrift.

Der zentrale Kern dieser Arbeit beschäftigt sich mit dem Wachstum und der Charakterisierung dieser 2D Silicen Monolagen auf Ag(111) Oberflächen sowie der Bildung von Silicen- Multilagen Strukturen. Die Charakterisierung dieser Materialien wurde in situ mit oberflächenempfindlichen Messmethoden wie der Raman Spektroskopie und der niederenergetischen Elektronenbeugung unter Ultrahochvakuum-Bedingungen durchgeführt. Eine zusätzliche Charakterisierung erfolgte ex situ mittels Raster-Kraft-Mikroskopie.

Die experimentell bestimmte spektrale Raman-Signatur der prototypischen epitaktischen $(3 \times 3)/(4 \times 4)$ Silicene Struktur wurde durch ab initio Rechnungen, in Zusammenarbeit mit Theoriegruppen, bestätigt. Durch diesen Vergleich wir die zweidimensionale Natur der epitaktischen Silicen-Schichten vollständig bestätigt, wodurch andere mögliche Interpretationen ausgeschlossen werden können. Darüber hinaus wurden die Ramans-Signaturen der weiteren 2D und 3D Siliziumphasen auf Ag(111) bestimmt, wodurch sich ein klares Bild der Bildung dieser Strukturen in Abhängigkeit von den Präparationsbedingungen ergibt.

Um die Möglichkeit der Funktionalisierung von Silicen und der weiteren 2D Si Strukturen zu testen, wurden diese unter UHV Bedingungen atomarem Wasserstoff ausgesetzt. Durch die Bindung zu den Wasserstoffamen wird die kristalline Struktur der Silicen-Schichten modifiziert und die Symmetrie reduziert, was sich deutlich

in der spektralen Raman-Signatur zeigt. Wie mittels Raman Spektroskopie gezeigt werden konnte, kann diese Modifikation durch thermische Desorption des Wasserstoffs rückgängig gemacht werden, ist also reversibel. Raman Messungen mit verschiedenen Anregungswellenlängen deuten darüber hinaus auf die Änderung der elektronischen Eigenschaften der Silicen-Schichten durch die Hydrierung hin. Der ursprüngliche halbmetallische Charakter der epitaktischen Silicen-Schicht geht möglicherweise in einen halbleitenden Zustand über.

Das Wachstum von Silicen Multilagen wurde ebenfalls mit *in situ* Ramanspektroskopie verfolgt. Die sich dabei ergebene Raman-Signatur wurde mit der Raman-Signatur von Ag terminiertem Si(111) verglichen. Hier zeigen sich große Ähnlichkeiten, die auf eine ähnliche atomare Struktur hindeuten und zeigen, dass Ag Atome für die Ausbildung der Oberflächenstruktur während des Wachstums der Si-Lagen verantwortlich sind. Die chemischen und physikalischen Eigenschaften dieser Struktur bestärken zusätzlich diese Äquivalenz.

Schlagwörter: Raman-Spektroskopie, Silicen, epitaktische Wachstum, Ag(111) Kristall, in situ, zweidimensionale Materialen, Hydrogenisation, Halbmetall, Oberflächenphononen.

# Contents

# Introduction

In times of fast technological progress, society anticipates its continuation and welcomes the invention of new ideas and concepts. For semiconductor technology such progress is based on the constant rise of the computational power which allows the omnipresent usage of computers. This constant improvement is possible due to the increasing number of transistors per fixed area on a chip, which is realized by lowering their dimensions. Such miniaturization is prescribed by the well-known "self-fulfilling Moore's law" [1], which also implies an inherent limit of such process, ensured by fundamental physical laws, whose impact grows when the dimensions are scaling down. The transistor with a linear size of several atoms along any dimension starts to behave as a purely quantum-mechanical system, hence, it cannot be described macroscopically. In other words, the physical properties of materials at low dimensions differ from the properties of the bulk counterparts and, therefore, require a solid description to be applied in real devices. In contrast to such "*top-down*" approaches, one can also start to study the materials at the limit itself, a two-dimensional (2D) limit, approaching from the "*bottom*".

The idea of a 2D crystal appears first to be fundamentally impossible due to the fact that the lattice fluctuations in such system would break it apart at non-zero temperature [2]. However, the discovery of graphene, a conceptual two-dimensional material [3], showed that the violations are possible. Generally, 2D materials present a rich playground for the physics and related scientific areas [4]. The reason for this is the high sensitivity of their physical properties to their structure: slight modifications of their structure lead to the simultaneous change of the related properties. This can be used for tuning the electronic, optical and chemical characteristics of the material. Unavoidably, a sufficient understanding of such

relation between structure and properties is required to control these sensitive systems. Thorough studies would then allow not only to establish the ultimate limit in semiconductor technology but also to support the discovery of the new physical effects and their applications in the future.

After the appearance of graphene and the Nobel prize for its discovery [5], the research of 2D materials is on the rise resulting in the discovery of other species. To understand the tremendous ongoing interest in other 2D materials, the properties of graphene need to be mentioned. Due to the linear electronic dispersion at the K points of the first Brillouin zone (FBZ), which consequently implies effectively massless charge carries their mobility reaches an outstanding value of $2.5 \cdot 10^5$ cm$^2$/Vs in graphene (at 2 K) [6]. As the Fermi level of pristine graphene is positioned directly at the overlap of these electronic bands, graphene exhibits no electronic band gap. This is a drawback for its applicability in devices, where the logic is based on the charge carrier crossing a band gap, hence, producing the "on" and "off" states. The proposed solutions to overcome this issue, such as graphene nanoribbons [7], bilayer graphene [8] compromise the combination of the existent bandgap and high electron mobility in graphene, *i.e.* reducing its level to a comparable one with the conventional semiconductors (Si, GaAs, InAs, etc) [9]. The overall application of graphene is not only hindered because of the absent band gap, but also because carbon-based materials are not widely accepted in the microelectronics.

Thus silicon, as the best-known semiconductor, the properties of which have been already studied for more than half a century can match the requirements of the technological pursuit. The enormous effort to study its properties has made its comprehensive application feasible. However, it continues to surprise the scientific community with new opportunities unravelled. The low-dimensional forms of silicon, such as Si nanoparticles (zero-dimensional), Si nanowires (one-dimensional), and lastly Si-containing molecules are also well-known for a long time [10]. Despite such variety of silicon forms, all of them consist of Si atoms in sp$^3$ hybridization, therefore they belong to the same Si allotrope. In contrary to that, the probable 2D Si layer would only host $sp^2$-hybridized atoms (like in graphene). Such one-atom-thin 2D crystal was predicted back in 1994 [11], showing its stability and, therefore, a possibility of its existence. Despite the fact that the observations of free-standing 2D Si layer are still absent, this idea was planted and agitated the scientific community for the last two decades. First theoretical predictions were improved by Guzman-Verri and Lew Yan Voon [12] (who also gave the name of *silicene*, similarly to graphene) and Cahangirov *et al.* [13], showing

that silicene has a buckled structure. The buckling originates from the electronic structure of the Si atoms, which, in contrast to the C atoms, do not favour purely $sp^2$ hybridization but rather accommodate an intermediate hybridization state, subsequently named as "mixed $sp^2/sp^3$ state" [13]. Neither planar, nor buckled silicene sheets, as a stand-alone material, have been confirmed experimentally up to now. In contrast to the carbon allotropes, which favour 2D forms (graphene) compared to the 3D structure (diamond) [14] and, therefore, present a global energy minimum, silicon-based materials exhibit an opposite trend: bulk Si has a lower total energy than silicene. This implies that, in the nature, silicene is much less stable than more energetically favourable bulk Si, therefore it is easy to be destroyed by the external factors such as contaminants, temperature *etc*. Nevertheless, silicene was discovered in its epitaxial form, grown on Ag(111) in 2012 by Vogt *et al.* [15]. This discovery has enormously boosted the research of elemental 2D materials beyond graphene [16] and allowed their first experimental, hands-on, investigations. The physical properties of epitaxial silicene turned out to be substantially different from the ones predicted for free-standing silicene [17]. Epitaxial silicene is also buckled and metallic despite the different atomic structure. The absence of an electronic band gap suggests that it is not applicable to the current semiconductor technology, similarly to graphene. However, in contrast to the latter, there are more ways to open the band gap in silicene. Such opportunities actually are enabled by the buckling. In contrast to the planar graphene, the electronic structure of the buckled lattice is easy to be perturbed via external influences such as an electro-magnetic field [18] or surface functionalization [19]. Apart from purely electronic application of silicene, it can host many exotic emerging physical phenomena, such as a quantum spin and anomalous Hall effects [20]. Moreover, it is possible to switch the topological properties just by varying the uniform electric field in the crystal [21]. Since the Si atoms are heavier than C atoms, silicene also exhibits a stronger spin-orbit coupling (3.9 meV) [22], which can be applied resulting in the almost ideal spin filter [23].

Clearly, silicene is an extremely promising material to be utilized in various applications. However, a free-standing form of silicene has to be discovered and, therefore, a quest for silicene is not finished. Hence the question of the identity of the epitaxial silicene is to be answered. Raman spectroscopy offers a very sophisticated way to identify a material, to retrieve its structural information as well as the electronic structure [24, 25]. In the case of epitaxial silicene on Ag(111), this is assuredly indispensable, since up to 6 possible monolayer Si structures on Ag(111) with the different physical properties were recently

discovered [26]. Moreover, the present discussion on the connection between epitaxial and free-standing silicene crystals needs to be solved. Equally, controversial debates on possible "silicite" [27], or so called "multi-layer silicene" [28], which can be grown on top of the first monolayer, can be clarified by Raman spectroscopy, which has shown the great suitability for the research of layered materials [29]. With the understanding of the pristine structures, further experimental investigations and the verification of the theoretical predictions can be carried out. Among the all interesting properties of silicene, the most technologically required one is the band gap opening. Hence, the functionalization of the silicene with different adatoms, which can open a band gap [30, 31], can be studied within the scope of the structural properties of such system. Overall, the investigation of silicene completes our knowledge of 2D materials, allowing to understand deep fundamentals of the matter in a solid state.

In this work the identification and investigation of epitaxial silicene, grown on the Ag(111) crystal, by means of *in situ* Raman spectroscopy was carried out. The first chapters focus on the known properties of silicene-related structures as well as the basics of experimental methods used to investigate epitaxial silicene. The experimental challenges of the silicene growth on Ag(111) and their solutions are disclosed in the Chapter 4, followed by the unravelling of the spectral signature of epitaxial silicene. The next chapters are devoted to the discussion of Raman fingerprints of epitaxial silicene and silicene-related phases, which can be grown on the Ag(111) surface. The functionalization of all silicene phases by atomic hydrogen is covered in the Chapter 5 showing that Raman spectroscopy is capable to identify the structural and even electronic modifications upon functionalization. The 2D Si structure, which is characteristic for the above-monolayer Si deposition, a so-called "multi-layer silicene" is studied spectroscopically and discussed in comparison to the inverse system of Ag layer on top of the Si substrate.

CHAPTER **2**

# Silicene

Silicene is an elemental two-dimensional (2D) crystal, composed of Si atoms, which are arranged in the honeycomb lattice [11]. The name "silicene" was coined in 2007 by Guzmán-Verri *et al.* [12] in accordance to the first prototypical 2D crystal, graphene [3]. Silicene, chronologically, the second elemental 2D material, has gained a great attention in the scientific community due to its electronic properties, which show advantages over graphene in many cases. Such outcome is rather unexpected considering that both graphene and silicene are 2D materials, hence, seemingly share the same properties. As known, the honeycomb structure can host a linear energy dispersion (Dirac cone) [32]. This is a well-known fact for graphene, the inherent planarity (originating from the pure $sp^2$ hybridization of the C atoms) of which ensures the ideal conditions for the emergence of linear dispersions [33]. In the case of silicene, such behaviour was not expected, since its crystal lattice is not planar but slightly buckled [13]. The buckling itself originates from the fact that the Si atoms do not favour a full $sp^2$ hybridization contrary to the C atoms. For the latter, it is actually possible to find the C atoms in every possible hybridization state [34], such as $sp$ one in acytelene, $sp^2$ - in benzene, and $sp^3$ - in methane. The Si atoms mostly prefer to resort in the $sp^3$ hydridization with an exclusion of disilene ($Si_2H_2$). On the other hand, the buckling of the silicene lattice makes it thermodynamically more stable due to a lower total energy, in comparison to a planar 2D Si layer [13]. The crystal structure and lattice parameters of a free-standing silicene are shown in Figure 2.1.

Despite the theoretical possibility of its existence, free-standing silicene has not yet been discovered. In contrast to the very stable graphene sheets, the $sp^2/sp^3$ hybridization state of the Si atoms in silicene leads to its high sensitivity/low stability against the external
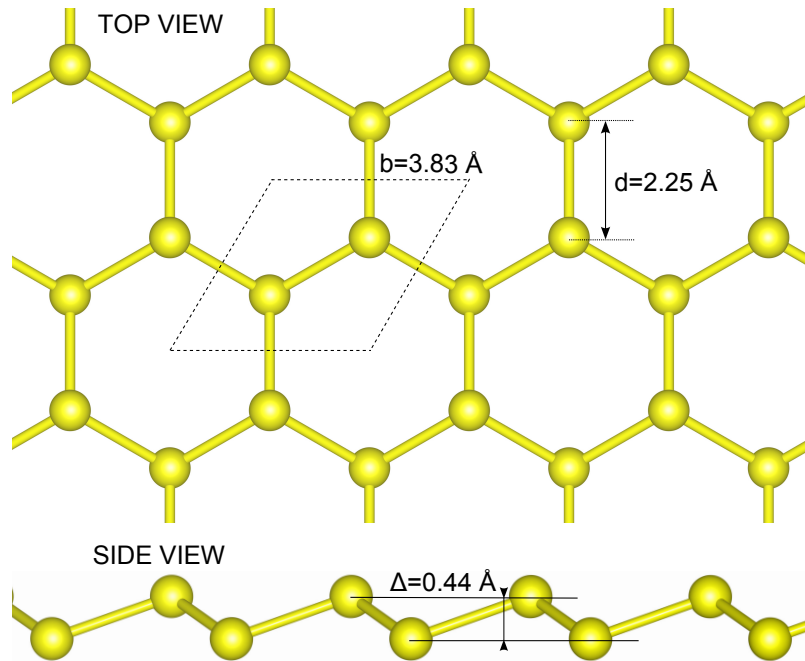
Figure 2.1: The top view and the side view of the free-standing silicene honeycomb lattice. The lattice parameters were taken from Ref. [13].

physical and chemical factors. This makes silicene unstable under ambient conditions. Moreover, silicene has a total energy higher than the one of bulk Si, which implies that the 2D allotrope is meta-stable. In other words, silicene can be easily converted into bulk Si (not necessarily crystalline phase) within a small energetic disturbance. Such situation does not allow free-standing silicene to be discovered in nature. However, it can be obtained synthetically. In this case, an additional support is needed to stabilize silicene sheets. The solution has been found in the use of the supporting substrates such as Ag(111) single crystal [15, 35, 36], $ZrB_2$ thin films [37], or Ir(111) single crystal [38]) to grow silicene epitaxially. Such epitaxial silicene was shown to adhere to these materials because of the matching lattice constants as well as a weak interaction to an adlayer. The substrates provide not only the support to keep the silicene lattice away from the collapse, but also ease the growth process itself. This can exemplified by the high diffusion length of the Si atoms on the silver surface, which allows them to find each other and form silicene [39]. This also evidences that the interaction between Si and Ag atoms is not strong, so no alloy (silicide) is formed. Such "weak" interaction between an adlayer and the substrate [15, 40–42] has not yet been fully understood though. As in the case of epitaxial graphene [43], the type of substrate matters and provides different coupling to the adlyaer, changing its structure
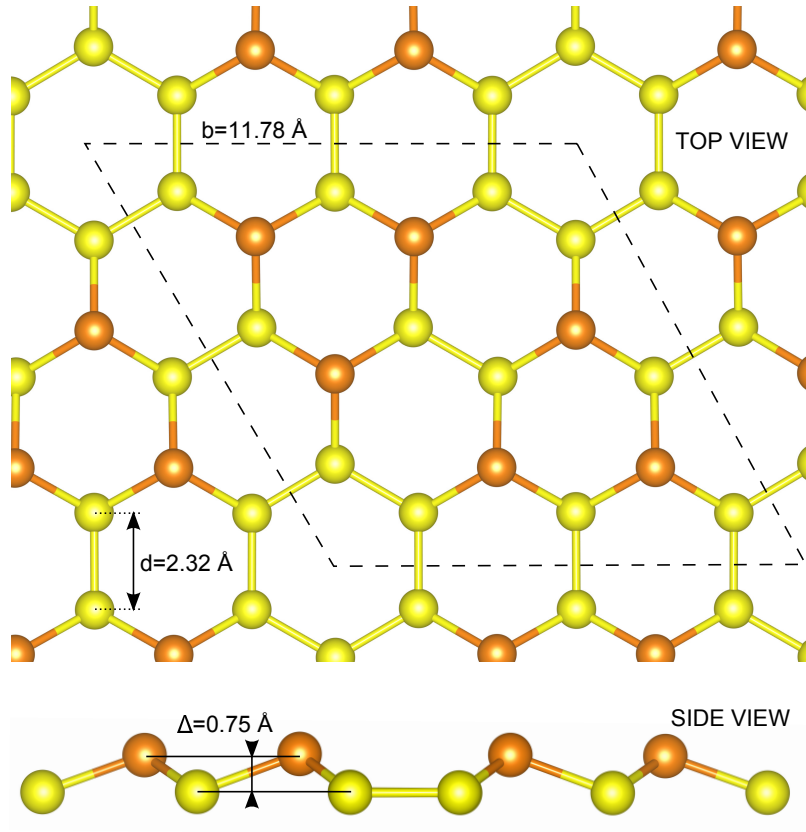
Figure 2.2: The top view and the side view of the epitaxial 3×3/4×4 silicene honeycomb lattice. The lattice parameters were taken from Ref. [15].

and electronic properties. One of the most studied, numerously reproduced, system is epitaxial silicene grown on Ag(111), which is the object of this work as well. The crystal structure and the lattice parameters of an epitaxial silicene grown on Ag(111) are shown in Figure. 2.2. The comparison between free-standing and epitaxial silicene shows that the lattice of the latter is modified (reconstructed) with respect to the free-standing form. The lattice reconstruction changes the buckling order and increases the size of the unit cell by three times in each direction. The unit cell of epitaxial silicene contains 18 Si atoms, from which 12 atoms are located in the lower sublattice (*down-buckled*) and 6 atoms are buckled in a opposite direction (*up-buckled*). The buckling and the Si-Si bond length are also enlarged in comparison to the free-standing form. All these modifications originate from the interaction between the silver surface and the silicene layer. As for the substrate, epitaxial silicene forms a commensurate lattice of the 4-fold periodicity with respect to Ag(111) unit cell [15]. The matching lattice parameters make the Ag(111) 1×1 surface suitable for

the growth of epitaxial silicene and hints towards the requirements of the substrate for the epitaxial growth of any 2D material. Overall, this epitaxial silicene phase has a periodicity of $(3 \times 3)/(4 \times 4)$, where first part refers to the one in respect to free-standing silicene and the second one - to the Ag(111) surface. Beyond the obvious structural differences, the common characteristic of both structures is their honeycomb lattice, which underlies their common origin. Consequently, the different atomic arrangement also results in different electronic properties of free-standing and epitaxial silicenes. The electronic structure of free-standing silicene is thoroughly described in the Ref. [13]. Despite the loss of the six-fold symmetry due to the buckling and, hence, the reduction of the symmetry group (from $D_{6h}$ to $D_{3d}$ [44], as shown in Fig. 2.3), one can still observe a linear energy dispersion around K and K' points, crossing the Fermi level. This implies the inherent (semi-) metallicity of silicene, which can be considered as one of the common properties of elemental 2D materials. The linear bands originate from the $\pi$ and $\pi^*$ bonding, but, in contrast to graphene, the $p_z$- and s-orbitals of the Si atoms are mixed, which weakens the $\pi$ bonding, but does not destroy the linear dispersions. Similarly to graphene [33], the electronic bands at $\Gamma$ are located at the considerable distance ($> 3$ eV).
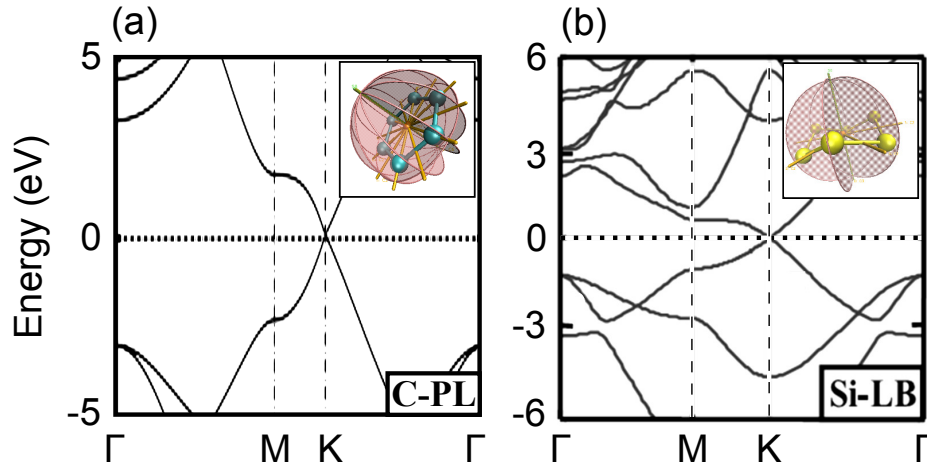


Figure 2.3: (a) Electronic band structure of graphene. The plot is adapted from Ref. [45]. Inset: The Wigner-Seitz cell of graphene. (b) Electronic band structure of free-standing silicene. The plot is adapted from Ref. [13]. Inset: The Wigner-Seitz cell of silicene. Both insets show the hexagons of the corresponding crystals, plotted together with the symmetry elements (rotation axes, reflection planes, inversion point). The Wigner-Seitz cell plots are prepared using the VMD software [46].

The electronic structure of epitaxial silicene on Ag(111) was experimentally probed by angle-resolved photoemission spectroscopy (ARPES) [15], scanning tunneling spectroscopy (STS) [47], X-Ray emission (XES) and absorption spectroscopy (XAS) [48] experiments and studied theoretically [47–49]. Due to the superstructure of epitaxial silicene, the sublattice symmetry breaking takes place, allowing the band gap opening which, thus, destroys the linear electron dispersions at the K point, according to DFT calculations (the substrate was not considered) [47]. ARPES data also suggested the presence of a band gap of the order of 0.3 eV [15]. In contradiction to this, the XES and XAS data suggested a metallic character of epitaxial silicene [48] with a non-zero density of states (DOS) over 15 eV range around the Fermi level. It was shown that if DFT simulations consider the underlying Ag(111) substrate (up to 11 Ag layers), the electronic structure of epitaxial silicene can be properly calculated [49]. Such modelling showed that the linear dispersion, observed in ARPES, turns out to be a quasilinear "silicene/Ag hybridized state", emerging from the interaction between the silicene and the silver atoms. Furthermore, the decomposition of the density of states (DOS) of epitaxial silicene simulated by DFT shows that the Ag substrate affects the $p_z$ states of the Si atoms, smearing them across the Fermi level [48]. Overall, epitaxial silicene grown on Ag(111) silver has a strong metallic character owing to the strong coupling to the substrate. Among the possible explanations, one can highlight the vdW type of interaction [15] and strong hybridization [49]. Another model of the interaction seems to be an alloy formation [50], which, however, was not proven experimentally. In order to retrieve the semi-metallic/semiconducting nature of free-standing silicene, the coupling to the substrate should be reduced by introducing a buffer layer between silicene and the substrate or by finding other (non-metallic) substrates, which could host silicene as well [51].

Along with the electronic properties of the crystals, their physical characteristics are also based on their vibrational structure. The vibrational structure of a crystal is given by the energy dispersion of the crystal vibrations over the Brillouin zone. Such characteristics are usually unique and robust, since it is mainly defined by the atomic structure and therefore less sensitive to any perturbations as much as the electronic structure. The knowledge of the vibrational structure does not only allow the identification of atomic arrangement but also allows the determination of its thermal properties. The vibrational structure of free-standing silicene has been vastly simulated using DFT [13, 52–54]. Since the different phonon dispersions reported are principally similar, Fig. 2.4 shows explicitly one exemplary dispersion, obtained in Ref.[13].

Figure 2.4: Phonon dispersion of the free-standing silicene. Notations: TO, LO, and ZO - transversal, longitudinal, and out-of-plane optical phonons, respectively; TA, LA, and ZA - transversal, longitudinal, and out-of-plane acoustic phonons, respectively. The solid black and dashed grey lines show the results, obtained via different theoretical methods, the details of which are beyond the scope of our discussion. The figure is adapted from the Ref. [13].
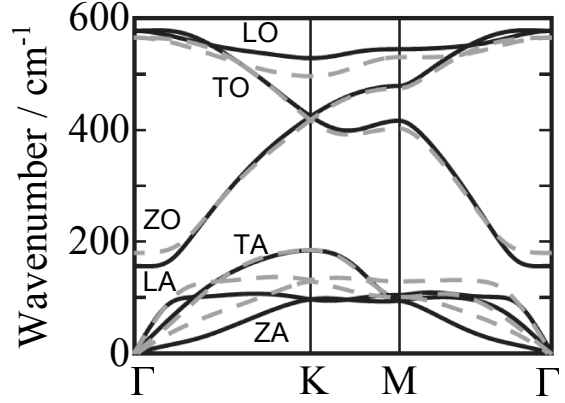
As in bulk silicon [55], free-standing silicene has two Si atoms per unit cell, therefore, the phonon energy diagram contains three acoustic as well as three optical phonon branches. While the longitudinal and both transversal optical phonons of bulk Si have the same energies, *i.e.* degenerate, in the center of the Brilluoin zone ($\Gamma$ point) according to the crystal symmetry (Fd-3m [24], p.52-58), only one of the TO phonons has an equal energy to the LO phonon in free-standing silicene. The other TO phonon acquires significantly lower energy as a result of the breaking of the translation symmetry in the direction, perpendicular to the 2D Si layer. In this case, one TO phonon is polarized in the *(x,y)* plane, while the other TO phonon, which is orthogonal to the first one, hence, it is polarized in the *(x,z)* or *(y,z)* planes, thus perpendicular to the 2D layer. This mode is referred to as a "ZO", flexural, phonon. The presence of the ZO phonons is the direct evidence of the two-dimensional character of a 2D crystal. Such situation can be encountered in many cases such as graphene [56, 57], transition metal dichalcogenides (TMDC) [53], and phosphorene [58]. Moreover, one can see that the energies of the LO and the TO phonons at $\Gamma$ are higher in silicene than in bulk Si. This is due to the fact that the Si atoms in silicene have a $sp^2$-like hybridization, which implies a stronger bonding ($\sigma + \pi$) between neighbouring Si atoms. The related increase of the force constant of the interatomic bond leads to an increase of the vibrational energy. This can be briefly explained via the classic model of an oscillator, where the eigenfrequency $\omega$ is a function of its mass $m$ and the spring constant $D$: $\omega \approx \sqrt{\frac{D}{m}}$. Indeed, in contrast to bulk Si, where the T(L)O phonons have an energy of 64.5 meV (520 cm$^{-1}$), the LO and TO phonons of free-standing silicene have an energy of 69.4 meV (560 cm$^{-1}$). A similar behaviour can be observed comparing the eigenfrequencies of diamond and graphene [25]. Overall, the vibrational structure can give a fruitful information about the crystal and its structure. Furthermore, it also reflects the electronic properties in special cases, such as 2D
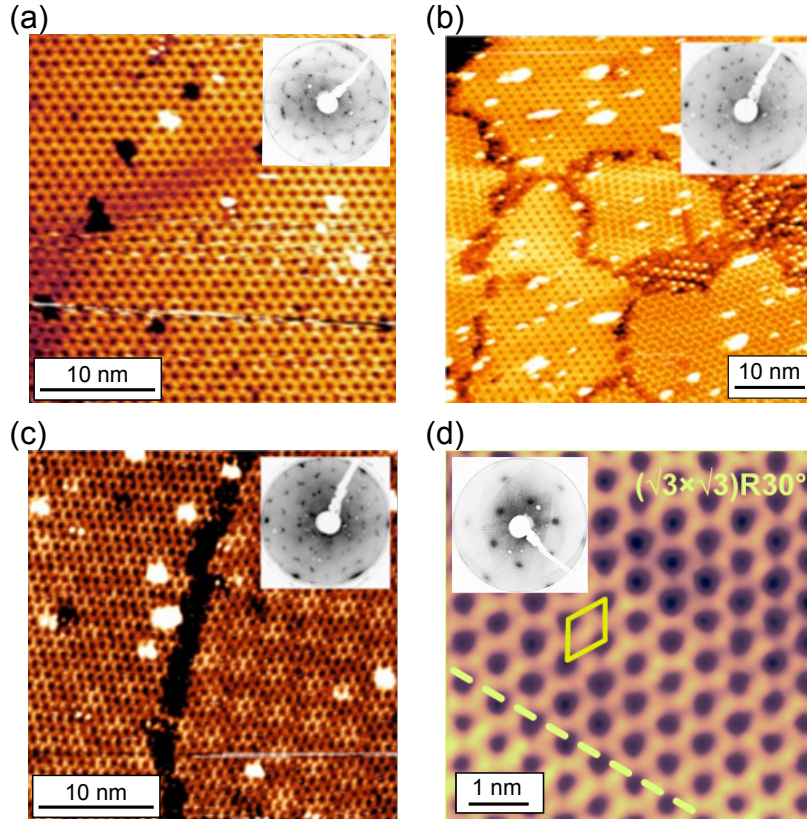
20

Figure 2.5: (a) STM topographic images ($U_{bias}$= -1.0 V, I = 1.08 nA) and corresponding LEED patterns (insets) of (a) 1 ML of Si deposited at 220°C resulting in (3×3) silicene formation, (b) 1 ML of Si deposited at 240°C showing the formation of several phases, (c) 1 ML of Si deposited at 280°C with a "$(2\sqrt{3}\times2\sqrt{3})R30°$" reconstruction, (d) 2 MLs of Si deposited at 220°C with a $(\sqrt{3}\times\sqrt{3})R30°$ periodicity. This STM topography images were adapted from Ref. [28].

materials [25]. In Fig. 2.4, it is seen that the LO and ZO phonon branches have sharp kinks at the K point. Such peculiar feature of the phonon dispersion is called a "Kohn anomaly" and appears when the screening of the phonons by the free electrons changes abruptly at the Fermi surfaces [59]. Interestingly, the Kohn anomaly is located at the K point, where the Dirac point (on the Fermi surface) in the electronic dispersions is situated (Fig. 2.3, b). Both of these effects suggest the presence of conduction electrons in the crystal (metallicity) and, moreover, their strong coupling to the phonons. Such effects were also observed in graphene [60].

The aforementioned properties of free-standing silicene and epitaxial (3×3)/(4×4) silicene on Ag(111) are the result of a comprehensive research over the last 5 years. Due to the great

interest in the topic, the experimental observations and their interpretations were rationalized quite fast. In fact, the growth of Si structures on Ag(111) yields more possible outcomes, possessing a rather complex character. It is known that epitaxial growth depends on the growth parameters such as the deposition temperature, the coverage and the growth rate. Only a precise control over these parameters allows the growth of the particular 2D structures. Apart from epitaxial $(3 \times 3)/(4 \times 4)$ silicene, the formation of other 2D structures on Ag(111) has been reported [61]. Their growth mainly depends on the temperature of the Ag substrate during Si deposition [61, 62] and $(3 \times 3)/(4 \times 4)$, $(\sqrt{7} \times \sqrt{7})R \pm 19.1°/(\sqrt{13} \times \sqrt{13})R \pm 13.9°$, and "$(2\sqrt{3} \times 2\sqrt{3})R30°$" phases appear on the surface in the narrow temperature window from 220°C to 280°C. Their STM topography images are shown together with the corresponding LEED patterns in Fig. 2.5(a-c) [28, 63]. The nature of other 2D Si structures and their correspondence to silicene were questioned due to their atomic arrangement and properties distinct from the free-standing form and highly symmetric $(3 \times 3)/(4 \times 4)$ phase. Moreover, their growth mechanism is also not fully understood. While the correspondence of the $(\sqrt{7} \times \sqrt{7})R \pm 19.1°/(\sqrt{13} \times \sqrt{13})R \pm 13.9°$ phases to epitaxial $(3 \times 3)/(4 \times 4)$ silicene can be understood through the lattice rotations and point defects [64–66], the "$(2\sqrt{3} \times 2\sqrt{3})R30°$" structure has more complex nature since it mainly consists of disordered areas [36, 39, 65]. Thus the symmetry, $(2\sqrt{3} \times 2\sqrt{3})R30°$, describes only the ordered parts, which is only 1/4 of the whole lattice, whereas the model of the complete phase is absent. Despite the higher formation temperature and thus higher stability, the "$(2\sqrt{3} \times 2\sqrt{3})$" is mainly defective, thus it cannot be described as an ideal well-ordered structure. Eventually, the phase diagram of the Si deposition on Ag(111) surface in the temperature range established for 2D layers consists of two single phases, $(3 \times 3)/(4 \times 4)$ and "$(2\sqrt{3} \times 2\sqrt{3})R30°$", and four subsidiary phases of $(\sqrt{7} \times \sqrt{7})R \pm 19.1°/(\sqrt{13} \times \sqrt{13})R \pm 13.9°$ periodicity.

Besides these phases the $(\sqrt{3} \times \sqrt{3})R30°$ structure has also been observed upon Si deposition on Ag(111). While Feng *et al.* [36] argued that this structure refers to a single layer, other works demonstrated that it only forms if more than one Si monolayer are deposited [28, 67, 68]. Due to this fact as well as its constant height, this structure has been interpreted as a "multi-layer silicene" [28] and supported by DFT simulations [69]. The ongoing discussion on the nature of this phase is due to the numerous discrepancies in the experimental observations and the absent model, which fully agrees with the experiment. Such issue arises from the complexity of the $(\sqrt{3} \times \sqrt{3})R30°$ structure, which is attempted to be interpreted by the stacking of the silicene monolayers [70, 71] or by the formation of

the bilayer structures [27]. These models, however, overestimate the layer thickness values. In STM experiments, the thickness was found to be about 0.3 nm [28], which is smaller comparing to the one, predicted in the models. Thus they cannot sufficiently describe the structure. According to other interpretations, "multi-layer silicene" forms due to the Ag atoms, which are present in the Si layer [72], or terminate the Si layer [73–76]. These ideas are reasonable, since the $(\sqrt{3}\times\sqrt{3})$ type of reconstruction is well-known for metals to form on a Si(111) surface [77]. Nevertheless, the experimental data shown are not conclusive, leaving room for many possible interpretations. Finally, the reconstructed surface of bulk Si was also suggested [78, 79] to explain the nature of "multi-layer silicene". Such claims are countered pointing to the use of wrong preparation parameters, mainly, high temperature [80]. Despite the debate on its nature, the $(\sqrt{3}\times\sqrt{3})R30°$ structure was shown to be interesting for the technological application and fundamental science. In contrast to monolayer structures, it is electronically decoupled from the Ag substrate [28]; it can host massless Dirac fermions [67] and other exotic quasiparticles [81]. Nevertheless, the successful application of this structure can be successfully reached only when the model is fully resolved.

It is noteworthy to mention that only ultrahigh vacuum-based (hereinafter, *in situ*) methods can be used for the research of silicene so far because of its low chemical stability. Such situation limits the broad investigation of the material with all experimental techniques available nowadays. Most of the works above-mentioned were carried out using the methods, based on electrons and electronic structure of silicene structures. At the same time, such powerful tool as vibrational spectroscopy, as well as other optical methods, has been little employed. On the contrary to the electron-based methods, the vibrational spectroscopy probes the phonons, the properties of which are highly robust, providing a highly reliable information about the atomic structure of the material, *i.e.* its spectral signature (fingerprint). This method can supplement our understanding of silicene with new aspects such as structural attributes of all present phases, their vibrational properties. Moreover, even *in situ* Raman spectroscopy is much easier to perform to identify the structure than, for instance, ARPES or STM. Therefore, spectroscopic measurements are strictly required in order to understand the $(\sqrt{3}\times\sqrt{3})R30°$ and other structures.

# Experimental methods

In the following chapter, the experimental methods used in this work and their theoretical background will be briefly discussed.

## 3.1   Raman spectroscopy

Raman scattering is a phenomenon, which occurs when light interacts with matter. According to the Maxwell equations, there are several types of such interaction listed as reflection, refraction, absorption and lastly scattering. During the scattering process, the moving object collides with another one, which leads to the trajectory deviation, while total momentum is conserved. In the case of light scattering, the moving object is a photon, while the scatterer (scattering center) can vary from the macroscopic objects to the quantum-mechanical entities such as phonons (the quanta of lattice vibrations) or other excitations. Depending on the energy of the photon scattered, one discriminates between elastic, *Rayleigh*, light scattering (the photon energy is preserved) and inelastic, *Brillouin* [82] and *Raman* [83] scattering, (the photon energy is not preserved). In any of the cases, the total energy of the system remains constant. Similarly to Rayleigh scattering, Raman scattering always occurs when light interacts with matter (gases, liquids, solids *etc*) but due to very low scattering cross-sections. The intensity of Raman scattering is lower than the one of Rayleigh scattering by 3-4 orders of magnitude [84]. Therefore it is impossible to be seen with the naked eye and thus requires the amplification by a number of technical solutions. In order to comprehend the necessity of such technological advances, the theoretical details of Raman scattering and spectroscopy itself as the method of scientific research need to be addressed first.

The theory of Raman scattering is profoundly described (both within classical and quantum-mechanical approaches) by Long [85], and Smith and Dent [86]. However, several general aspects of Raman scattering, which are important for further discussion in this work, shall be discussed here. According to the Maxwell equations, any piece of condensed matter can be polarized if it is placed inside an electric field. This means that electric charges will align accordingly to the direction of the electric field resulting in the formation of dipoles. In case of an oscillating electric field (as the one of an electromagnetic wave), the polarization of the physical body will oscillate as well, thus the dipoles will emit the light [87]. The polarization of a solid is defined by the polarizability, the characteristic property of the material, related to its average susceptibility. The polarizability originates from the fact the bound electrons inside a piece of condensed matter experience a restoring force due to the interaction with the nuclei, rigidly strained in the chemical bonds in the crystal lattice or molecular structure. Furthermore, the oscillating electric field can also change the polarizability of the condensed matter, inducing the actual movement of the ions themselves. Such motion, however, has some predefined characteristics: it is rather small (the fraction of Å); it has a fixed frequency (energy) and its pattern is determined by the specific interaction between the ions. The frequency of scattered light is modulated by the eigenfrequency of the lattice vibration (thus there is a finite change of polarizability). Due to the modulation, the frequency of scattered light is different to the one of incident light by the lattice eigenfrequency. This fulfils the energy conservation. The eigenfrequencies can be expressed in terms of the quanta of the lattice vibrations, *i.e.* phonons. As a quasiparticle, phonon also exhibits a momentum. According to the momentum conservation law, only phonons with the momenta close to 0 can interact with the photons because of the steeper dispersion relation of light, which crosses the phonon dispersions in the center of the Brillouin zone of the crystal. In the case of molecules, this corresponds to the symmetric vibrations, which give no change to the molecular dipole moment.

The scattering processes mentioned can be schematically portrayed within the energy scale as shown in Fig.3.1. As the light scattering does not require a real electron transition, the Rayleigh scattering considers that the electron transits back to the electronic ground state after the promotion to a virtual electronic state ($E_v$). In the case of Raman scattering, the electron relaxes back to an electronic ground state but to an excited vibrational state. The difference between two transitions $E_{0,0} \rightarrow E_v$ and $E_v \rightarrow E_{0,1}$ is equal to the magnitude of the vibrational energy itself and called the *Raman shift*. This holds for both Stokes (the negative
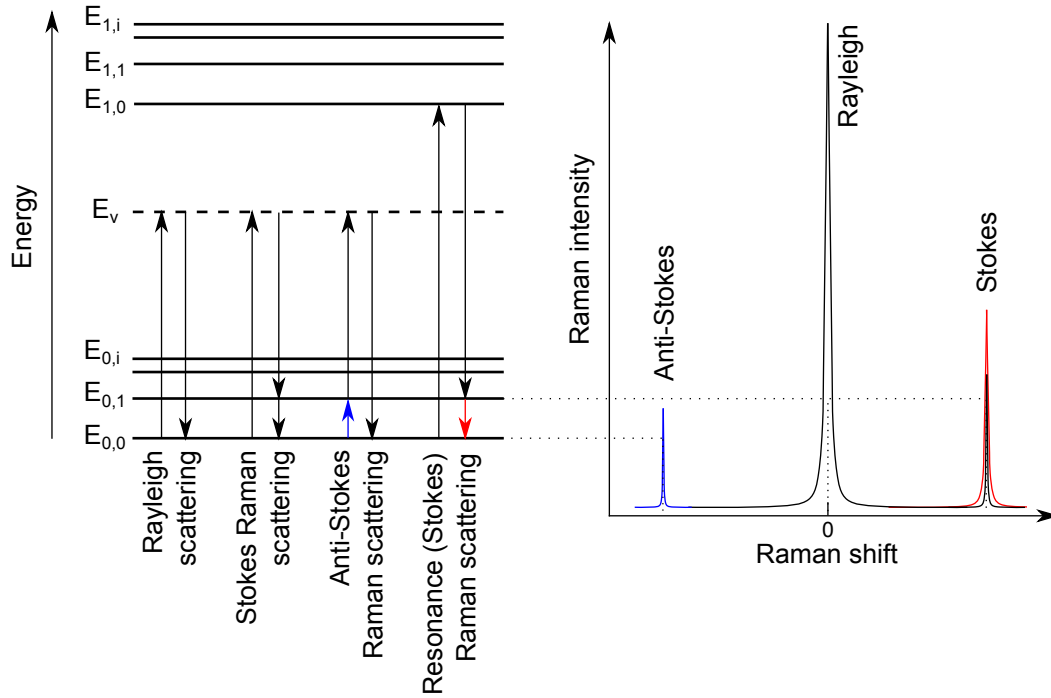
Figure 3.1: Schematic presentation of scattering processes on the energy scale. The notation $E_{j,i}$ represents the energy levels, where $j$ stands for the electronic energy states and $i$ - for vibrational energy states. $E_v$ - virtual energy state. The schematic Raman spectrum, shown on the right hand side, represents all the processes depicted on the scheme.

energy difference) and Anti-Stokes (the positive energy difference) Raman scattering, which differ, however, in the initial vibrational state. For the latter, it is necessary for the system to reside in the excited state which is always true at room temperature. Clearly, the number of phonons in the ground state is higher than the number of excited phonons, which is reflected in the higher Raman band intensity in case of Stokes in contrast to the Anti-Stokes shift. Rayleigh scattered light has a zero Raman shift and dominates the Raman spectrum in terms of its intensity. Eventually, Raman scattering can occur also within the real optical transition of an electron. This resonant process involves a change in electronic density in the crystal lattice, which is manifested by the enhanced intensity of the Raman bands due to the electron-phonon coupling. This effect is rather complex for a brief description and nicely described in Ref. [24], p. 121-137.

Raman scattering is an inherently weak physical process. In our experiments, only $10^{-14}$ of exciting photons are detected as the inelastically scattered photons for the solids with an average scattering efficiency, *e.g.* a bulk silicon crystal, which is governed by the scattering

cross section. Eventually not only the cross section is a reason to the usually low Raman signals but also the technical difficulties. Such issues, which are important for this work, will be in the focus of the following part. Namely, crystal volume, macro configuration and *in situ* experiments, and the power density of the laser line will be discussed. All listed issues were encountered and overcome during the experiments described here. The scattering efficiency of a material $\theta$ is a quantity, characteristic for a certain material as well as its eigenmodes, $\omega_0$. It is usually expressed by (according to Ref. [24]):

$$\theta = N_i(\omega_s/c)^4 V L \mid \mathbf{e}_i \cdot (\frac{\partial \chi}{\partial \mathbf{Q}})_0 \mathbf{Q}(\omega_0) \cdot \mathbf{e}_s \mid^2$$

where $N_i$ - the number of scatterers, $\omega_s$ - the frequency of the scattered light, $\mathbf{e}_i$, $\mathbf{e}_s$ - the polarization unit vectors of the incident and the scattered light, respectively, $V$ - the scattering volume, $L$ - the scattering length, $Q$ - the displacement vector, and $\chi$ - the electric susceptibility. The scattering efficiency is directly proportional to the intensity of the Raman bands in the spectrum. As it is clear from the expression, the Raman intensity also depends on the various factors such as the energy of the exciting light, the scattering volume, and $\mid \mathbf{e}_i \cdot \mathfrak{R} \cdot \mathbf{e}_s \mid^2$, where $\mathfrak{R} = \frac{\partial \kappa}{\partial \mathbf{Q}}_0 \mathbf{Q}(\omega_0)$. $\mathfrak{R}$ is called the *Raman tensor* and is used as a simplified expression of the first derivative of the susceptibility over the atomic displacement, which is usually difficult to obtain analytically. In the case of two-dimensional materials, which are in the focus of this work, the scattering volume is also a fixed parameter. The effect of the amount of probed volume on the Raman intensity is essential. For the instrument used in this work, the ratio between signals of 3D and 2D Si allotropes, considering the signal throughput of the instrument and the particular excitation wavelength of 514.5 nm, is 1000:1, respectively. For the 2D one-atom-thin materials the effective Raman signal is inherently low, hence it can be increased only through other enhancement channels. Using a resonant excitation wavelength allows the increase of the Raman signal by orders of magnitude. Eventually, it is possible to observe the phonon Raman spectra of monolayer silicene structures only because of the resonance.

Aforementioned factors, which influence the Raman intensity, are related to the material properties, while the power density of a laser line and the energy-dependent instrumental response function (the sensitivity of the instrument) are basically technical issues. The instrumental sensitivity is usually optimized for the highest throughput but still varies over the spectral range. The total sensitivity of the instrument is a function of the sensitivities of all optical elements involved. Thus a triple-monochromator spectrometer has a lower

signal throughput than a spectrometer with only one diffraction grating. Since the response function cannot be altered, this factor has to be included into the evaluation of the Raman intensity in the spectra measured with different excitation energies. The power density of a laser line, however, is a variable quantity and can be increased to obtain a better signal. The relation between the Raman intensity and the power is, in fact, linear. However, the laser power density cannot be infinitely increased due to the limitation of the laser itself (all laser have a finite output power) and the possible thermal damaging of the sample. Therefore, one should use the optimum power range to get the highest possible Raman intensity preventing the sample from heating by the laser excitation. The standard power density used in this work is below $10^3$ W/cm$^2$, which corresponds to the a power of 1 W (the maximal laser power of the Ar$^+$ laser (*INNOVA 70C*)) and a laser spot size of 300 $\mu$m$^2$. Despite the seemingly large laser power, its power density is by two orders of magnitude lower when compared to the usual micro-Raman measurements (the difference comes due to the use of the microscope objectives, which considerably reduce the laser spot size).

The last group of parameters which define the Raman intensity are related to the nature of the measurement itself. The acquisition time (exposure) and collection (objective, the slit width) are attributed to this group. The exposure is the most variable parameter in Raman measurements as it can be infinitely prolonged. It is accompanied by the number of exposure repetitions which comprise the measure of the signal-to-noise ratio. A high signal-to-noise ratio is achieved via increasing the number of accumulations, which averages out the effective signal, as well as the exposure time. This works properly for the samples with significant scattering efficiency. In the case of low Raman signals, the exposure time should be increased significantly, which, in principal, can compensate other deficiencies such as poor collection by the entrance lens or small probed volume. The standard acquisition time of one cycle used in this work is 144 seconds. Such value comes from the fact the spectral signal-to-noise ratio is proportional to the square roots of exposure as well as the repetitions ($S/N \approx \sqrt{\frac{time}{repetition}}$). Thus, the usual repetition number is 9 (for quick measurement) and 25 for high-quality spectra. The collection of the effective signal depends on the type of Raman spectroscopy. The Raman measurement can be performed in macro- and micro-Raman configurations; the latter implies the use of a microscope. In case of a micro-Raman regime, the collection of inelastically scattered light is carried out through a microscope objective. Such solution not only helps to substantially increase the spatial resolution of a measurement but also improves the collection since the solid angle of the objective is usually greater than of the standard

lens. In case of many *in situ* Raman measurements, the microscope is not easy to apply when samples are located inside the particular container, *e.g.* cryostat, electrochemical cell, ultra-high vacuum (UHV) chamber *etc*. The latter is the usual experimental component in surface science, since the surfaces are inherently very sensitive to the ambient conditions. The necessity of using a UHV chamber for the growth and characterization of the samples requires a list of technical issues, such as a high power density of the laser lines, a long exposure times, and an efficient rejection of the Rayleigh scattered light.

## 3.2 Group theory: Basics

Symmetry is a fundamental concept of nature manifested on each scale of its existence. Intrinsic symmetry of physical systems simplifies their understanding and rationalization. The use of symmetry is handled by the branch of mathematics, which is called "group theory". The fundamentals and application of group theory are vastly described in [88]. Here, only the basics of group theory with the main focus on its application in Raman spectroscopy are covered.

The matter in a solid state tend to arrange in a symmetric way forming crystals. By definition, crystals exhibit a translation symmetry of a single unique atomic arrangement (unit cell), in all possible directions. The unit cell can also have an internal symmetry in respect to rotations, reflections, inversions, and the combinations of those. The electronic as well as vibrational structures of the crystal are governed by the symmetry of the unit cell and its components (atoms, molecules etc). All existing crystals can be described using 230 space groups, which include the symmetry operations of the point groups (rotation, reflection, and inversion) and the translational operations. Unlike the electronic structure, the vibrational structure of the crystal is mainly dependent on the lattice symmetry. Therefore, the knowledge about the particular symmetry group of a crystal allow the determination of the symmetry of its vibrational eigenmodes. This can be performed via careful analysis of the character table of the symmetry group applying it to a particular crystal lattice. To illustrate the applicability of the character table, the one of the $C_{6v}$ point symmetry group will be explained (Table 3.1). This symmetry group is chosen on purpose since it describes the symmetry of epitaxial $(3 \times 3)/(4 \times 4)$ silicene.

The first row of the character table (except the group notation (after Schoenflies) in the first column) shows the symmetry operations, which belong to this group: E - identity operation,

Table 3.1: Character table for point group $C_{6v}$

| $C_{6v}$ | E | $2C_6$ | $2C_3$ | $C_2$ | $3\sigma_v$ | $3\sigma_d$ | | Basic | components |
|----|----|----|----|----|----|----|----|----|----|
| $A_1$ | 1 | 1 | 1 | 1 | 1 | 1 | z | | $x^2+y^2$, $z^2$ |
| $A_2$ | 1 | 1 | 1 | 1 | -1 | -1 | | $R_z$ | |
| $B_1$ | 1 | -1 | 1 | -1 | 1 | -1 | | | |
| $B_2$ | 1 | -1 | 1 | -1 | -1 | 1 | | | |
| $E_1$ | 2 | 1 | -1 | -2 | 0 | 0 | (x, y) | $(R_x, R_y)$ | (xz, yz) |
| $E_2$ | 2 | -1 | -1 | 2 | 0 | 0 | | x | $(x^2-y^2$, xy) |

C - rotation (subscripts denote the folding) , $\sigma$ - reflection (subscripts denote the plane of reflection: $v$ - vertical, $d$ - diagonal). The first column contains the irreducible representations of the physical properties of a system described as the transformation matrices: A and B are one-dimensional representations of matrices with symmetric and antisymmetric rotational operations in respect to the principal axis (an axis of the highest order symmetry), respectively. The E representation is two-dimensional and stands for the functions with a double-degeneracy. The subscripts indicate whether the particular representation has symmetric (1) or antisymmetric (2) two-fold rotation perpendicular to the principal axis or vertical symmetry plane [88]. The main part of the table contains the characters of the symmetry operations in respect to the irreducible representations (the intersections of the first row and the first column). The character is the trace of the transformation matrix which identifies the certain irreducible representation incorporated into the reducible one under the symmetry operation. Overall, it is important that the representations "represent" the physical properties of a system, which can be described by the basis functions. The particular physical properties (atomic orbitals, vibrations, magnetic moment etc) can be transformed as vectors (as the ones which designate the spatial coordinates *x, y, z* or rotational axis $R_x$, $R_y$, $R_z$) or pseudovectors $(x^2, y^2, z^2, 2yz, 2xz, 2xy)$. These are listed in the last three columns of the character table. In the case of vibrational spectroscopy, these basis functions describe the Raman- and IR-active vibrations in accordance to the physical quantity which is affected by the certain eigenmode. Shortly, the vibration is IR-active if the dipole moment of a system is being changed during the motion and the vibration is Raman-active if the polarizability is being changed. Due to the fact that the dipole moment is a vector and the polarizability is a $2^{nd}$-rank tensor, these eigenmodes have different representations. Thus, from table 3.1, we can see that IR-active modes can be described as $A_1$ and $E_1$ representations, while Raman-active modes (Raman modes) can be described as $A_1$, $E_1$, and $E_2$ representations. The particular basis functions define the components of the aforementioned Raman tensors.

Thus the Raman tensors of $C_{6v}$ are:

$$A_1 = \begin{pmatrix} a & 0 & 0 \\ 0 & a & 0 \\ 0 & 0 & b \end{pmatrix}; \; E_1 = \begin{pmatrix} 0 & 0 & c \\ 0 & 0 & c \\ c & c & 0 \end{pmatrix}; \; E_2 = \begin{pmatrix} d & -d & 0 \\ -d & -d & 0 \\ 0 & 0 & 0 \end{pmatrix}$$

Raman tensors contain the information about the intensity of the Raman modes and their selection rules. Selection rules allow the Raman modes to be observed in certain experimental geometry. In Raman spectroscopy, one distinguishes (forward)back-scattering and right-angle geometries in accordance with the incident and scattered light propagation vectors, depending whether they are parallel or perpendicular to each other. In addition to the geometries, the scattering configurations are also important. The main configurations are the *parallel* and *crossed* ones. From the names it implies that the polarization plane of the incident light is parallel to the one of the scattered light in the former case, while the polarization planes are orthogonal for the latter one. In a particular configuration, the coupling between the polarization planes of the incident and scattered light with the Raman tensor of a particular Raman mode defines its defining its presence in the spectrum. Mathematically, this can be expressed by $e_i \cdot \Re \cdot e_s$. As an example:

$$\begin{pmatrix} 1 \\ 0 \\ 0 \end{pmatrix} \times \begin{pmatrix} a & 0 & 0 \\ 0 & a & 0 \\ 0 & 0 & b \end{pmatrix} \times \begin{pmatrix} 1 \\ 0 \\ 0 \end{pmatrix} = a$$

Here, the Raman mode with A type of symmetry is probed by the light polarized along the x axis, while the polarization of the scattered light is parallel oriented. In this configuration, the intensity of the Raman mode is proportional to the $x_{1,1}(=a)$ matrix element. In the case of "crossed" configuration, the matrix product is equal to zero, hence, the Raman mode is not allowed, hence, must not be detected in the experiment. The intensity of the E modes would be equal in both geometries, which stems from the fact that such mode is degenerate. In the experiment, it is important to define the coordinate system, which is probed by changing the scattering configurations. In this work, the scattering geometries are named after Porto's notations, which designate the propagation directions by the symbols outside the parenthesis and the polarization planes by the symbols inside the parenthesis for the incident and scattered light in the coordinate system of a sample [89]. For instance, *-z(xx)z*

implies that incident light propagates along the *z* axis (normal to the sample's surface) with the polarization aligned along the *x* axis, while the scattered light is collected along the *z* axis as well (such configuration is called a "back-scattering geometry"), also polarized along the *x* axis (this is defined by the second polariser, analyzer, in front of an entrance slit). Hence, the *-z(yx)z* geometry implies the parallel propagation directions but orthogonal polarization planes. The right-angle scattering geometries allow more combinations of the propagation and polarization directions, however, such experimental set-up is mainly inapplicable for the one-atom-thin crystals. Overall, by changing the scattering configurations, the Raman tensor of a particular mode can be determined. This is an extremely powerful tool in the identification of the crystal structure.

## 3.3 Low-energy electron diffraction

Low energy electron diffraction (LEED) is a powerful technique, widely used in surface science to identify the structural symmetry of surfaces and 2D materials. The concept of LEED is based on the effect of electron diffraction by the crystal lattice. The de Broglie wavelength of electrons can be estimated as $\lambda_{el} = h/(m_{el}V_{el}) = \sqrt{150/E_{el}}$. Thus low-energy electron ($E_{el} < 100$ eV) have the wavelengths in the order of 1 Å, which corresponds to the atomic dimensions. Since the electron mean free path in a solid is small, the low-energy electrons appear highly surface sensitive. Typical LEED pattern of Ag(111) surface is shown in Fig.3.2(a).

The diffraction spots are formed due to the constructive interference of the electrons diffracted exposing the crystal lattice in the reciprocal space. The coherence length of the electrons lies in the range of 10 - 20 nm, which determines the minimal size of an ordered structure to be observed. The working principle of LEED is based on the concept of the Ewald sphere, hence the LEED optics is implemented in a hemispherical fashion, including the hemispherical fluorescent screen and the electron gun located in the center of a screen. Thus the diffraction spots observed are the intersections of electron momentum vectors and the Ewald sphere, located in accordance to the (h,k) order of the lattice. The central spot is always (0,0) and also overlays with the primary electron beam. Varying the electron energy, one varies the size of the Ewald sphere. In LEED measurements, low-energy electrons ($E_{el} <$50 eV) produce the image of several Brillouin zones of the structure on the surface, giving the information on the translation symmetry of the crystal. In the case of complex

(a)

(b)

(2,0)

$\mathbf{k'}$ $\mathbf{K = k - k'}$

(1,0)

(0,0)

$\mathbf{k}$

(-1,0)

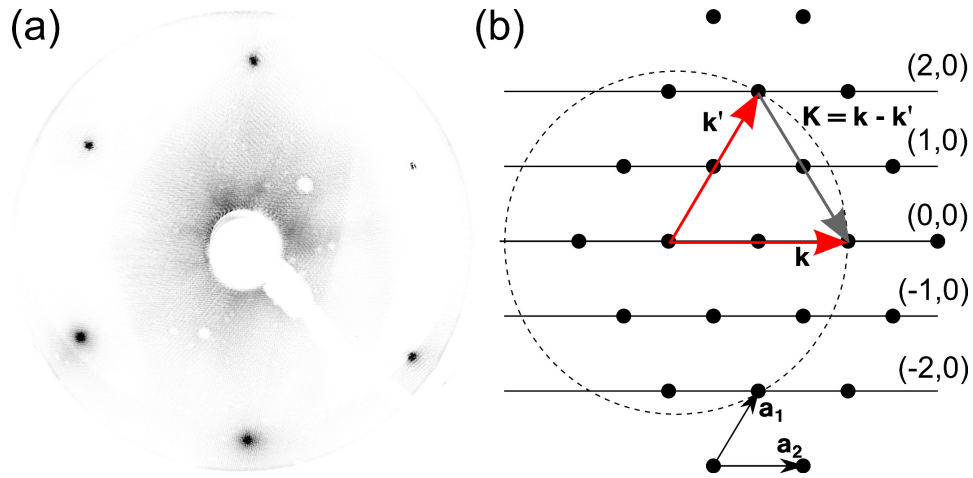(-2,0)

$\mathbf{a_1}$

$\mathbf{a_2}$

Figure 3.2: (a) Typical LEED pattern of Ag(111) 1×1 surface reconstruction. (b) Corresponding scheme of reciprocal space of a hexagonal lattice, including the Ewald sphere. Notation: $\mathbf{a_1}$ and $\mathbf{a_2}$ - reciprocal lattice vectors; $\mathbf{k}$ and $\mathbf{k'}$ are the momenta of electrons diffracted from (0,0) and (2,0) directions.

structures (more than one type of structure on the sample surface), the LEED pattern allows the domain structure on a qualitative level to be extracted. The pattern acquisition is carried out by making the photographs the fluorescent screen with a digital camera (*Canon 60D*) with the always same parameters of photographing (such as ISO, exposure, etc).

## 3.4 Atomic force microscopy

In this work, the surface morphology was probed by atomic force microscopy (AFM). This method is based on the effect of the interaction between the surface and a tip (curvature radius: ca. 10 nm, *μMasch, NGS series*) in a close proximity to the surface. According to the distance between the tip and the probed surface, which determines the forces acting on the tip, one distinguishes a contact and a non-contact modes. While the tip stays in touch (hard contact) with the surface, it is found in a repulsive regime due to the Coulomb-type interaction. Moving away from the surface, the tip starts to be affected by the attractive van der Waals forces deflecting it from the equilibrium position accordingly to the surface morphology. The alternating contact (tapping) mode used in this work lies in-between aforementioned regimes, implying that the tip stays in non-contact regime periodically touching the sample surface. Such modus operandi produces the images with high resolution and additional information about the surface such as phase images. In the latter, the contrast

is given by the lagging of the tip in the case of stronger interaction with the corresponding areas. This can hint towards the hardness/softness of a material. The deflection of the tip is monitored via detecting the change in a laser position from the back of the cantilever. As the laser impinges onto a the photo-detector, deflection is converted into the height profile over the linear scans. The precision of the AFM in height reaches the sub-nanometer range, while the lateral resolution is limited by the tip radius and usually lies in the range of tens of nanometres. The AFM images shown in this work were acquired *ex situ* using an *Agilent AFM 5420* and processed using WSXM software [90].

## 3.5   Experimental set-up for *in situ* **Raman spectroscopy**

The experimental set-up used in this work consists of a UHV chamber, a spectrometer and two lasers. The complete setup is displayed in Figure 3.3.
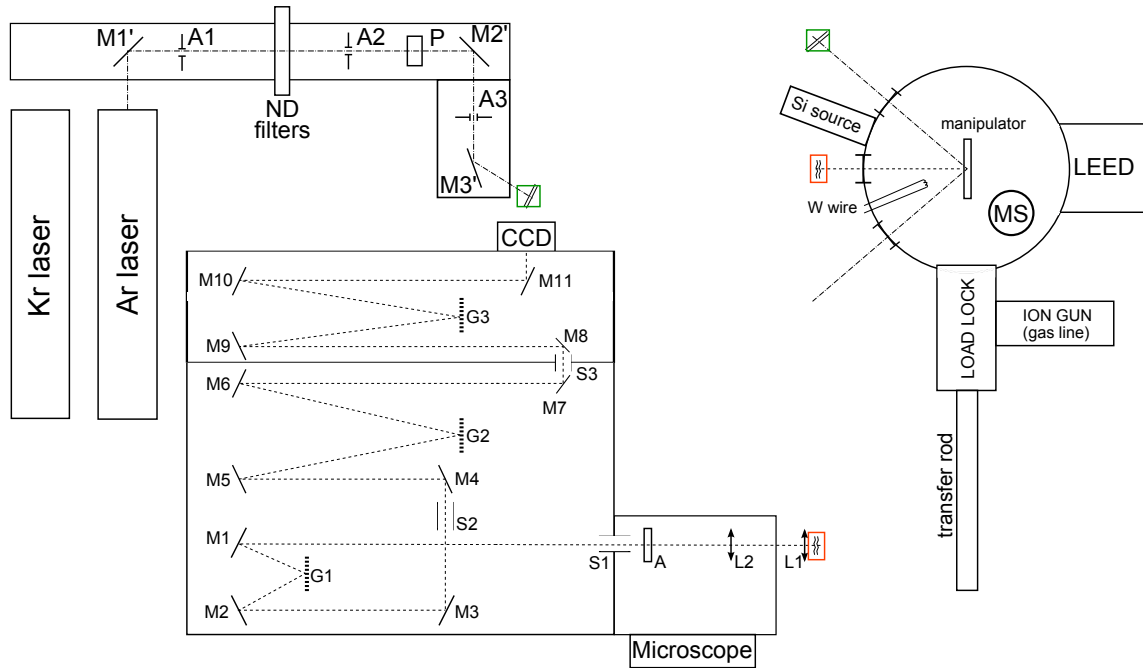


Figure 3.3: The scheme of the experimental set-up including the lasers and optical table, UHV chamber and the triple-monochromator spectrometer Dilor XY800. M: mirror. An: Aperture. P: quarter-wave plate. S: slit. G: reflection grating. L: lens. MS: mass spectrometer. ND: neutral density. The optical path after M3 is continued in the scheme of UHV chamber, which is depicted with curve breaking lines. The collection from the UHV chamber is carried out with L1 (curve break).

The light sources used are $Ar^+$ and $Kr^+$ lasers (*Coherent INNOVA 70C* and *300*, respectively). Gas lasers are especially suitable for Raman spectroscopy because of high output powers (up to several Watts) and the narrow linewidth of the excitation wavelengths (usually below the $1 \, cm^{-1}$). Laser light is guided through three apertures (denoted as A1, A2, and A3 in Fig.3.3) to ensure the straight incidence along the optical axis. The laser light is linearly polarized, therefore, a waveplate *P* is used to rotate the polarization plane. Eventually, the light falls onto the sample inside the UHV chamber through the sapphire window to ensure the transmittance of a broad range of the laser lines. The scattered light is collected through the lens *L1* hitting the entrance slit *S1* of the triple-monochromator spectrometer (*Jobin Yvon Dilor XY800*). The collected light is guided through a set of mirrors and slits to the three reflection gratings (1800 l/mm), which disperse the light to deliver the highest possible energy separation in the Raman spectrum. The light dispersion is wavelength-dependent, hence it is higher for longer excitation wavelengths. The first monochromator (two gratings) is used to reject the elastically scattered light via intentional shift in respect to a third grating. It basically acts as a bandpass filter. Therefore, neither notch nor edge filters are required to suppress the Rayleigh light in the triple-monochromator spectrometer. This also enables the measurements of the phonon modes in a low-frequency range (down to $10 \, cm^{-1}$). The polariser *A* allows the control of the polarization plane of the light collected, which is a prerequisite for the determination of the Raman selection rules. The spectrometer is equipped with an electrically cooled charge-couple device (*Synapse CCD, Horiba*) which significantly increases the detection sensitivity and allows a multichannel detection. Due to this feature of CCD camera and the availability of gratings with smaller number of grooves per unit length (150 and 600 l/mm) the spectrometer can also be used to measure luminescence. Although the spectrometer is equipped with the microscope, this option has not been used in this work. All Raman measurements shown later were performed *in situ*, *i.e.* measuring the Raman scattering of the samples inside the UHV chamber. The base pressure in the UHV chamber is kept at $2 \times 10^{-10}$ mbar using two turbomolecular pumps (*Leybold*) and the ionic pump (*IONVAC, Leybold*). The chamber is also equipped with a quadrupole mass spectrometer, which is used to identify the composition of the residual gases. The sample transfer is carried out using the load lock system, which base pressure is in the high vacuum range ($5 \times 10^{-9}$). The ion source is mounted to the load lock and used for the sample cleaning. UHV chamber is equipped with the low-energy electron diffraction (LEED) optics (*SpectaLEED, Omicron*).

## 3.6 Growth of monolayer silicene on Ag(111)

In order to grow silicene sheets on Ag(111) epitaxially, several requirements, such as proper substrate condition, a source for Si atoms, a controlled growth rate, and a substrate temperature, should be matched. The substrate, which was used in this work, is a silver single crystal with a cut along the (111) crystallographic plane ("Ag(111)"). Due to the fact that silver, as many other metals, has a face-centered cubic crystal structure, its (111) plane has a hexagonal atomic arrangement, which turns out to be suitable for a growth of a honeycomb Si crystals. The Ag(111) crystals used were manufactured by *Surface Preparation Laboratory (SPL), Zaandam, The Netherlands* and *Mateck GmbH, Julich, Germany*. The surface of such crystals is polished up to 0.1 degree of the off-cut in order to achieve its best possible smoothness. The shape of the substrate surface is circular with 1 cm in diameter, which was chosen according to the design of the sample holder. The crystal surface, despite the absence of macroscopic defects, is usually contaminated with residuals of the polishing process (mostly, of the hydrocarbonic nature) and the Ag-based molecules (silver sulphides, oxides, *etc*), appearing in ambient atmosphere. While the former species are almost impossible to remove, the latter can be cleaned using a standard method in surface science: alternating cycles of ion bombardment (sputtering) and annealing. A typical sputtering run implies surface bombardment with $Ar^+$ ions, ionized and accelerated by the ion gun (*ISE 5, Scienta-Omicron*). Such cleaning procedure involves a handful of physical processes, vastly described in Ref. [91]. Briefly, the accelerated $Ar^+$ ions provide energy to the molecules, bonded to the surface, to break their bonds to the surface and let them desorb. The important parameters of sputtering are the duration, the ion energy, and the amount of Ar gas used (determined by the gas pressure). All factors directly scale with the sputtering efficiency. The usual parameter set includes 15 minutes of sputtering with the ions accelerated by an energy of 1.5 keV at $1 \cdot 10^{-5}$ mbar. These are the optimal parameters to obtain macroscopically smooth Ag(111) surface. Longer duration as well as higher acceleration energy may result in a non-reversible surface roughness. The latter appears due to the fact that $Ar^+$ ions also collide with the Ag atoms eliminating them from the surface. In order to overcome such intrinsic drawback of the sputtering procedure, the silver crystal can be annealed at the temperature around 520°C. During the annealing, the surface atoms acquire the thermal energy allowing them to drift towards the positions with a lower potential energy, which are usually a vacancy or a terrace edge. Hence, the Ag terraces grow larger and become smoother. The experiments showed that the annealing temperature

may exceed a value of 520°C but not by more than 30°C, which, otherwise, end up in the melting of the crystal since the melting point of a material is significantly decreased in UHV (for Ag in ambient pressure, it is 961.8°C). The surface quality during the annealing is also directly proportional to its duration. During the parameter optimization, it was determined that the satisfactory surface quality can be obtained within 20 minutes of annealing at 520°C. After the annealing is over, the sample slowly cools to room temperature. Initial substrate cleaning involves 10 cleaning cycles, while the initially cleaned Ag substrate requires only one cleaning cycle for a new deposition run. In order to test the surface quality, necessary for the Si deposition, LEED and Raman measurements are utilized. The typical Raman spectrum of a clean silver surface is shown in Fig. 3.4. The spectrum exhibits no Raman bands since elemental metals with 1 atom per cubic unit cell (of a face or body-centred cubic system) do not host optical phonons, but acoustical ones, which have a zero energy at the center of FBZ [92]. The characteristic spectral feature in the Raman spectra of metals is a so-called "Rayleigh tail", due to very strong reflectivity of the metal surface. The elastic scattering, in principle, can be also considered as the measure of the surface roughness since rough surfaces diffuse the light more efficiently due to the larger number of the reflection planes. In our case, these two factors always play a role in the measurements, hence, they need to be considered. Namely, the Rayleigh tail can be fitted and extracted from the spectrum without any loss of information.

The corresponding LEED pattern is shown in the inset of Fig. 3.4. Such LEED patterns are characteristic for a hexagonal lattice of the fcc metals. A sign of the surface cleanness are the sharp diffraction spots and the low-intense background light (around the central spot). Such a background is mainly coming from the direct reflection of the electron gun itself but also from the surface defects (amorphous areas, roughness, contaminants etc), which increase the number of randomly diffracted electrons. An ideal LEED pattern shows only intense sharp spots of the electrons diffracted. It is important to remember that the hydrocarbonic residuals of the polishing process are impossible to be entirely removed. However, their amount can be reduced to the level, at which their presence is not detected any more in Raman measurements. As a source for Si atoms, a directly heated piece of a Si wafer was used. The rate of the thermal evaporation linearly scales with the current. This also determines the growth rate. Depending on the current, a monolayer sheet can be grown in a time period starting from a few minutes to several hours. An important factor for the growth rate is also the distance between the Si source and the substrate, which is 11 cm in our case.
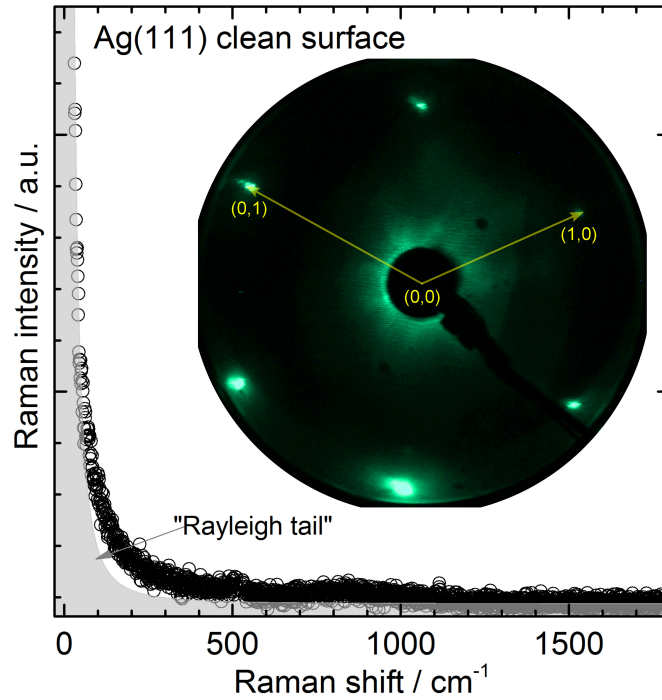
Figure 3.4: Raman spectrum of clean Ag(111) surface. Rayleigh contribution ("tail") is fitted with Lorentzian curve, centered at 0 cm$^{-1}$. Inset: LEED pattern of a clean Ag(111) surface with a diffraction spots of a 1×1 reconstruction. The arrows indicate the unit cell of the reciprocal lattice. The central point is (0,0). $E_{el}$ = 50 eV.

Prior to the deposition, the Si source should be degassed to the base pressure of the UHV chamber. The last important requirement for the Si deposition onto the Ag(111) surface is the possibility to heat the substrate. As it was discussed in the Chapter 2, the deposition temperature plays a crucial role for the silicene formation. Moreover, a precise temperature control is required since the deposition range which corresponds to the 2D Si structures formation is rather narrow (ca. 50°C). The precision of 5°C can be achieved by directly contacting the substrate and a thermocouple (compatible with the UHV environment). This, however, is not possible in our case. According to the initial design of the manipulator, the thermocouple is attached to the sample holder. The loss of precision is not crucial since the sample composition can be determined by LEED and Raman spectroscopy, which eventually became a good test for the structures grown. Alternative way of the temperature calibration could be a temperature-dependent Raman measurement of bulk Si, which is, however, of no use in this case since the sample positioning in respect to the sample holder is different for Si piece and Ag sample. This changes the conditions of the heat transfer

for each sample. Silicon is deposited under UHV conditions by exposure of the Ag(111) surface at a given substrate temperature to a Si beam with a fixed evaporating temperature. The latter defines the growth rate, which is determined by monolayers per time period. The determination of the growth rate is the first task to be completed. It is troublesome when the usual surface science techniques, such as Auger electron spectroscopy (AES), X-ray photoemission spectroscopy (XPS) not available. Moreover, despite that LEED is a surface-sensitive method, its applicability for coverage studies is reduced due to the impossible quantitative analysis of the image (which is feasible, though, for LEED with a spot-profile-analysis option (SPA-LEED), for example). In our case, the growth rate as well as the surface coverage were determined by the combination of LEED and Raman data. To approach the 1 ML coverage of the epitaxial silicene, the submonolayer and supramonolayer regimes need to be understood in order to define the limits of a monolayer coverage. In order to exemplify the coverage challenge, the set of LEED patterns are shown in Fig. 3.5.
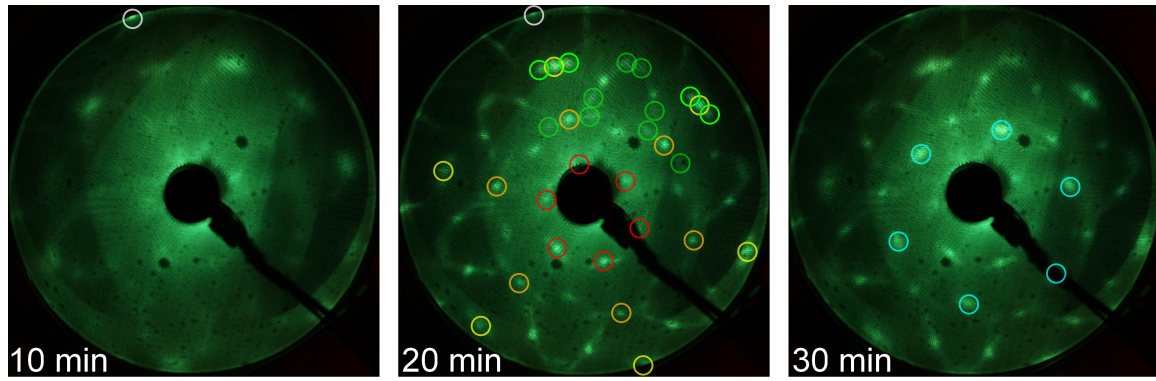


Figure 3.5: LEED patterns of the 2D Si structures on the Ag(111) depending on a surface coverage as a function of exposure. Deposition temperature: > 220°C. The electron energy ($E_{el}$ = 25 eV) is chosen to show main diffraction spots of the silicene sheets and to hide the high-intense spots of the 1×1 reconstruction of the silver surface. Colour code of circles designates the Si structure: red-orange-yellow-white circle show the 4×4 periodicity of epitaxial silicene, green circles correspond to the $(\sqrt{7}\times\sqrt{7})R \pm 19.1°/(\sqrt{13}\times\sqrt{13})R \pm 13.9°$, and blue circles show the LEED pattern of the $(\sqrt{3}\times\sqrt{3})R30°$ structure.

Although the changes in the LEED patterns of the structures deposited are obvious, it is, in fact, difficult to determine the coverage regime exactly due to the co-existence and similarity in the structural symmetry of different phases. The LEED pattern, obtained after 20 minutes of Si deposition, belongs to the so-called "dominant (3×3)/(4×4)" phase. As it was mentioned in the previous chapter, the (3×3)/(4×4) layer is a single-phase structure,

while $(\sqrt{7}\times\sqrt{7})R\pm19.1°/(\sqrt{13}\times\sqrt{13})R\pm13.9°$ phases are only subsidiary structures, which always accompany a single-phase structure. The diffraction spots of the former are located along the directions of the 1×1 silver unit cell (white circles), but, due to the smaller unit cell, they fit 4 times between (0,0) and the first-order Ag spots. They are highlighted by red, orange, yellow circles. The last, 4th, spot on the line overlays the diffraction spot of the substrate. The diffraction spots of $(\sqrt{7}\times\sqrt{7})R\pm19.1°/(\sqrt{13}\times\sqrt{13})R\pm13.9°$ phases (marked with green circles) deviate from the main spots of the (3×3)/(4×4) structure due to the different rotation angles, contributing to the areas of smeared spots (shown only for one direction). The LEED pattern obtained after 10 minutes of Si deposition partly resembles the one discussed, however, the intensity and the sharpness of the diffraction spots is poorer when compared to a higher coverage, which suggests a low amount of silicene formed. The LEED pattern of 30 minutes of Si deposition shows sharp and intense spots of (3×3)/(4×4) structure as well as the ones marked with blue circles. These are the indication of an adlayer with another symmetry, namely, $(\sqrt{3}\times\sqrt{3})R30°$, which is attributed to the structure of the so-called "multilayer silicene" [28]. The presence of these spots obviously indicates the supramonolayer coverage regime. Despite that a careful analysis of the LEED patterns would still allow the identification of the coverage regimes, its sensitivity is greatly reduced by the disability of the quantitative interpretation. Such deficiency can be overcome using Raman spectroscopy as the subsequent test technique for the coverage regime. The Raman spectra, corresponding to the LEED patterns in Fig. 3.5, are shown in Fig. 3.6.

These spectra exhibit diverse sets of the Raman bands which correspond to the significant structural differences of the Si phases of different coverage regimes. It will be shown below that coverage regime is possible to determine by careful examination of the following Raman spectra, recorded at presumably different coverages. The Raman spectrum of the Si structure deposited within 10 minutes of exposure has only one broad Raman band around 514 cm$^{-1}$. This band is clearly observed in the Raman spectrum of the 20 minutes of Si deposition. It is expected assuming that its intensity should increase with a prolongation of the deposition time (since the Raman intensity is a function of the probed volume). However, it also exhibits a band at 216 cm$^{-1}$, which should be also visible after 10 minutes of Si deposition due to the comparable intensity to the one at 514 cm$^{-1}$. This is, however, not the case, which brings to an idea that the Raman bands 216 cm$^{-1}$ and 514 cm$^{-1}$ are not attributed to the same structure. Otherwise, the discrepancy between the top and the middle spectra would have a more complex nature. To support this statement, one should examine the Raman spectrum
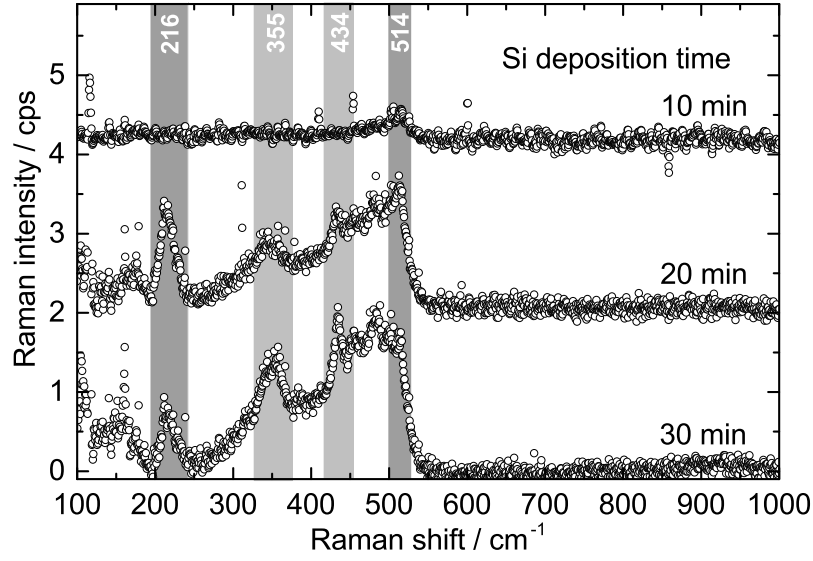
Figure 3.6: Raman spectra of the samples prepared by the Si deposition onto Ag(111) varying the duration of Si deposition. The spectra are stacked for clarity.

of the sample deposited within 30 minutes. It shows the following trends (when compared to the Raman spectrum in the middle): the intensities of both bands mentioned simultaneously decrease, while the magnitude of the other Raman modes at 355 and 434 cm$^{-1}$ is directly scaling with the amount of Si atoms deposited. Such progressions suggest that these pairs of Raman bands belong to the same structures (note their notation in the figure). This already allows some conclusions. Firstly, the "multi-layer structure" formed after 30 minutes of Si deposition, which was observed in the LEED pattern (Fig. 3.5, 30 min) is also present in the sample obtained with 20 minutes of Si deposition. The relevant diffraction spots can be also seen in the LEED pattern (not marked), which was, however, not obvious from the first glance. Hereby, 20 minutes of Si deposition skips over to the supramonolayer regime and thus the monolayer coverage must lie between 10 and 20 minutes of the exposure to a Si vapour with a constant flux. Secondly, the Si structure, to which bands at 216 and 514 cm$^{-1}$ belong, is not completely formed within 10 minutes of the Si deposition. This is in the agreement with the corresponding LEED pattern, which weakly resembles the one of the (3×3)/(4×4) symmetry. In other words, the Raman spectrum of submonolayer coverages is not just a scale-down version of the one of the monolayer coverage, but rather shows the sign of an incomplete structure. This agrees well with the STM studies of epitaxial silicene-related phases [15, 26, 61, 93], which demonstrated the layer-by-layer, Frank-van der Merwe, growth mode for the first monolayer.

Evidently, Raman spectroscopy proves its applicability for the structural studies, showing that the insightful conclusions can be drawn immediately even without the full knowledge of the spectral features. However, the growth rate calibration would be not possible without LEED patterns, which coarsely show the approximate surface composition. Thus the combination of both techniques and the self-consistent interpretation of the results allowed us to understand the Si growth on Ag(111) and to assign the proper Raman spectrum to a particular Si structure grown intentionally. It is noteworthy that all possible 2D Si layers were numerously grown in the course of the investigation showing the results demonstrated are highly reproducible.

### *In situ* hydrogenation of 2D Si layers

The hydrogenation process can be performed under UHV conditions by cracking the hydrogen molecules by a hot filament. For this purpose, a tungsten (W) wire was introduced into the chamber and connected to the current supply via the electrical feed-through (Fig. 3.3). The hydrogenation occurs when the chamber is filled with $H_2$ up to the pressure of $10^{-6}$ mbar ($7.5 \cdot 10^{-7}$ Torr) and the current of about 3 A passes through the W wire in a close proximity to the sample (ca. 2 cm). The exposure of the surface to atomic hydrogen is measured in Langmuirs (1 L = $10^{-6}$ Torr/s). For example, the dose of 100 L implies the exposure of H for 100 seconds at a pressure of $10^{-6}$ Torr ($1.3 \cdot 10^{-6}$ mbar). The exposure to atomic hydrogen stops when no voltage is applied to the W filament, thus no hydrogen ions are being produced. As in the case of *in situ* monitoring of the silicene growth, the time required for the acquisition of the Raman spectrum greatly exceeds the time of the structural modifications due to hydrogenation. Therefore, only step-wise hydrogenation can be carried out. Nevertheless, a control of the H dose via varying the exposure time allows the precise control over the whole hydrogenation process.

# *In situ* Raman spectroscopy of Si structures grown on Ag(111)

In this chapter, the silicene growth and characterization using *in situ* Raman spectroscopy is discussed. The deposition of Si atoms onto the Ag(111) surface can result in the formation of 2D as well as 3D structures. While the 3D structures may have arbitrary sizes in all three dimensions, the formation of 2D layers is limited to the thickness of just one atom. Their formation is being referred to as a monolayer coverage. Consequently, if the deposition of the Si atoms, sufficient for a complete 2D monolayer coverage, ends up in the 3D structure formation, such film cannot be continuous. Fig. 4.1 shows the Raman spectra of 1 ML deposition at various deposition temperatures of the Ag substrate. The Raman spectra of the structures grown at low temperatures ($< 200°$C) show only weak and broad Raman bands. First sharp spectral features in the spectral range from 175 to 514 cm$^{-1}$ appear when the substrate temperature during the deposition reaches 220°C. Further increase of the deposition temperature results in the rise of the band at 520 cm$^{-1}$. The variation of the Raman spectral lineshapes with the substrate temperature during the deposition demonstrates that the temperature is a key growth parameter in the Si/Ag(111) system. Such tremendous changes of the spectral signature imply the significant structural differences of the structures formed in each specific temperature range. The details of each spectrum shown will be thoroughly discussed in this chapter. In the case of 2D layers, the theoretical background for the deposition temperature as a measure of the formation energy of the Si structures is described in Ref. [44]. Briefly, the substrate temperature during Si deposition defines the additional kinetic energy of the Si atoms at the silver surface. Thus the Si atoms with higher

Figure 4.1: Raman spectra of the various structures obtained upon Si deposition at room temperature (RT), 220, 250, 280, and 300°C. In the spectral range between 550 and 830 cm$^{-1}$, no features were observed. The spectra are stacked for clarity. The topmost Raman spectrum was divided by 10 times for a better comparison with the rest of spectra in the plot.
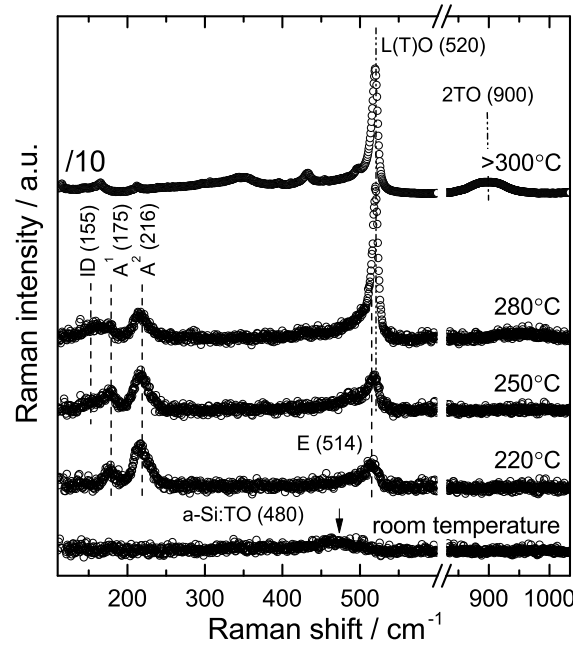
kinetic energy can assemble into the structure, which total energy is higher. Beside the 2D structures, the Si atoms can also form crystalline 3D structures, if energetic requirements are fulfilled or amorphous 3D structures, if not. Appearance of these phases and transitions from one phase to another can be monitored by Raman spectroscopy. The identification of the particular Si species is then provided via the characteristic spectral features in the Raman spectrum. While the signatures of 3D Si phases are well-studied and, therefore, easily recognizable, the ones of 2D Si structures need to be determined first.

## 4.1 Bulk silicon structure formation

### Si deposition at room temperature

In order to explain the formation of the 2D Si structures, first the formation of 3D phases and their manifestations in the spectra have to be explained in order to exclude them from the considerations whenever possible. The Raman spectra recorded after Si deposition at room temperature exhibit a broad Raman band at 480 cm$^{-1}$ with a shoulder around 350 cm$^{-1}$ (Fig. 4.1, bottom). Narrow phonon modes indicative of a crystalline order are not observed in this case. Therefore it can be assumed that amorphous phase is formed. In order to test this assumption, the Raman spectrum of a sample after the deposition of nominal 1 ML of Si at room temperature is plotted together with the spectrum of the sample prepared under
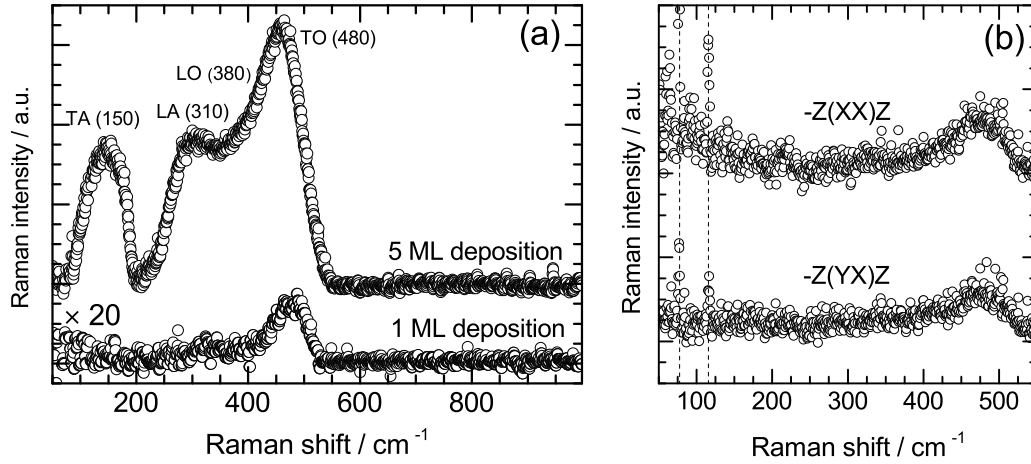
Figure 4.2: (a) Raman spectra recorded of samples after Si deposition at room temperature the coverage of 1 ML and 5 MLs. (b) Polarization-dependent Raman spectra of the room temperature Si deposition in parallel *-z(xx)z* and crossed (*-z(yx)z*) geometries. Dashed lines mark the plasma lines of Ar laser.

identical conditions but with 5 nominal MLs of Si deposited in Fig. 4.2(a). In contrast to the spectrum of 1 ML, the Raman spectrum of a sample with 5 MLs of Si clearly shows broad Raman bands at $150\,\mathrm{cm^{-1}}$ and at $310\,\mathrm{cm^{-1}}$. The shoulder, which is seemingly centred around $350\,\mathrm{cm^{-1}}$ in the case of 1 ML of Si, turns out to be a superimposed by the two real Raman bands, which are assigned to the longitudinal acoustic (LA) ($310\,\mathrm{cm^{-1}}$) and optical (LO) ($380\,\mathrm{cm^{-1}}$) phonon modes of silicon in an amorphous phase (a-Si) [94]. Overall, the spectrum shows a strong similarity to the one of amorphous Si [95, 96]. In the case of the 1 nominal ML, the Raman intensity of all Raman bands is very weak. Practically, only the most intense band at $480\,\mathrm{cm^{-1}}$ can be detected. In order to validate this finding, polarization-dependent Raman measurements were carried out. As it was described in the Chapter 3, the Raman intensity of the vibrational modes is sensitive to the incident light polarization, which can be used to deduce the Raman selection rules for each mode, based on its Raman tensor. In this case, the parallel (*-z(xx)z*) and crossed (*-z(yx)z*) scattering geometries can be used to reveal such polarization dependence. Fig. 4.2(b) displays the Raman spectra of the sample at the deposition of 1 ML Si at room temperature in the opposite scattering geometries. The only Raman band at $480\,\mathrm{cm^{-1}}$, characteristic for amorphous silicon, is visible in both Raman spectra. Such an insensitivity to the light polarization implies that this mode is not polarized. Such behaviour is obviously related to the intrinsic disorder in a-Si. The slight increase of the background towards the low-energy side of a
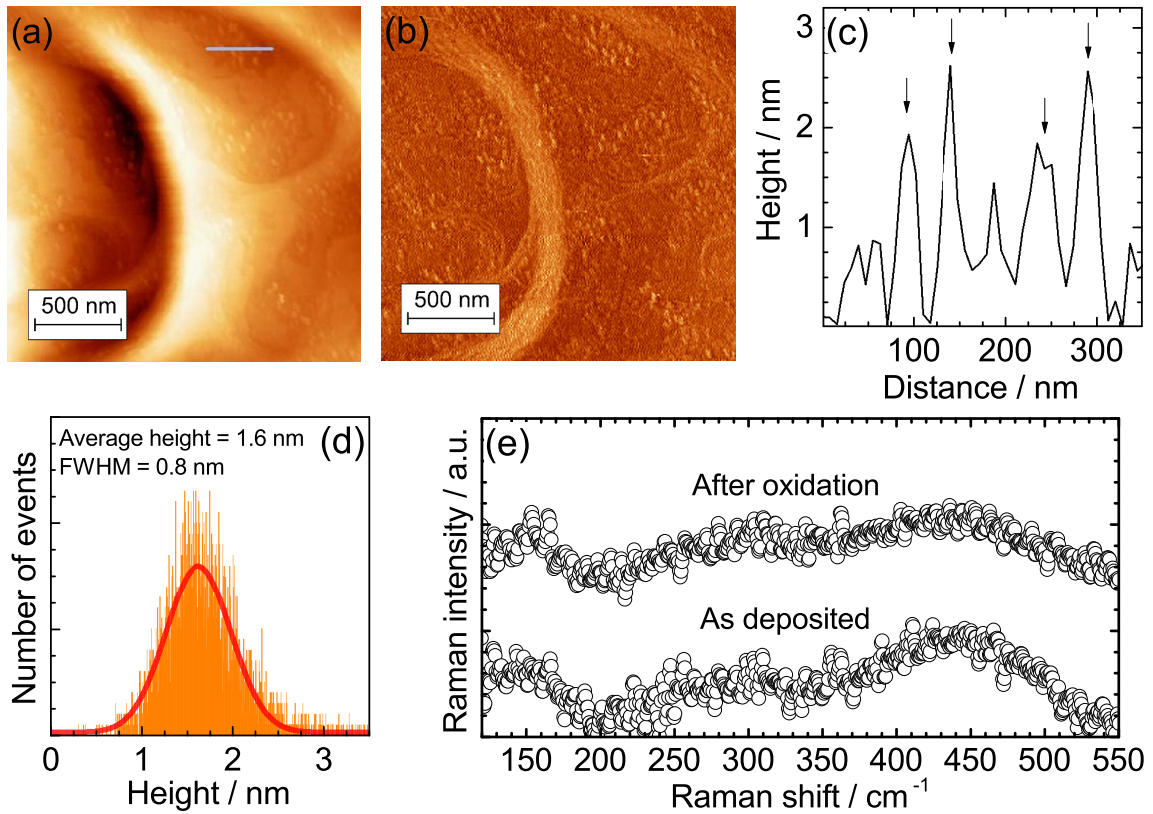
Figure 4.3: *Ex situ* AFM topography measurement of the Ag(111) surface after the 1 ML deposition at room temperature: (a) topography and (b) phase images. (c) Height profile, along the line at the topography image. (d) Height distribution of features at the AFM topography image. (e) Raman spectra of the Si deposition (above 1 ML) at room temperature, recorded before and after the oxidation.

spectrum is due to the Rayleigh scattering peak at 0 cm$^{-1}$, which is, however, cancelled by the perpendicular positioned polarizers in the crossed-geometry spectrum.

*Ex situ* AFM topography images of this sample obtained under ambient conditions, *i.e.* after oxidation in air, are displayed in Fig. 4.3(a). One can find numerous bright features having an average height of 1.6 nm (Fig.4.3(d)), which can be found within the scanning range. Despite the low height, the lateral size of the features reaches tens of micrometers, thus they are referred to as the islands. The contrast in the AFM phase image (Fig. 4.3(b)) demonstrates a different chemical composition of the islands in contrast to the Ag(111) surface. It is therefore possible to assign the clusters observed to amorphous silicon. The exposure of the sample to ambient atmosphere can also lead to the partial oxidation of the sample (including the substrate) [97]. It was shown that, although, amorphous silicon is

oxidized in the same self-limiting manner as a crystalline phase [98], such process is unlikely at room temperature. Moreover, the formation of $SiO_x$ cannot directly be observed by Raman spectroscopy due to the non-resonant scattering conditions and low probed volume of $SiO_x$ present on the substrate. The Raman measurements of the RT sample performed after the oxidation exhibit the spectrum which is identical to the one, recorded before the oxidation (Fig. 4.3(e)). In combination with the Raman results, it is concluded that the small islands, observed in Fig. 4.3, are related to a-Si. This demonstrates that Si deposition at low temperatures ($\leqslant 150°C$) results in neither 2D, nor 3D ordered Si structures formation. It can be safely assumed that the Si deposition at even lower temperatures ($\leqslant 0°C$) leads to a similar outcome. As for the RT Si deposition, it was recently suggested that impinging Si atoms penetrate the Ag(111) surface, replacing the Ag atoms and thus act as the seeds for the growth of recessed islands [50]. At the same time, released Ag atoms released should form the new Ag(111) terraces by a process described to occur more rapidly as the size of the embedded islands increases. These assumptions are not supported by the Raman results, which demonstrate that RT deposition leads to the formation of amorphous Si clusters only. Moreover, the Raman spectra recorded after the Si deposition at higher temperatures up to 150°C, retain the same spectral profile, suggesting the formation of amorphous silicon on silver surface in the broad temperature range.

## Si deposition at temperatures above 300°C

Another type of 3D Si structures is formed when Si is deposited onto Ag(111) at the deposition temperatures exceeding 300°C. In this case, only the characteristic (1×1) pattern of the initial Ag 1×1 surface is found without any other distinctive diffraction spots (Fig. 4.4(b)). Intense background suggests a poor quality of the silver surface after Si deposition. Fig. 4.4(a) shows the Raman spectra after deposition of 1 ML of Si at 290 and 350°C. Both spectra are dominated by an intense Raman band at 520 $cm^{-1}$ with a full width at half maximum (FWHM) of 8 $cm^{-1}$. This mode is similar to the L(T)O phonon mode of the diamond-like silicon clearly indicating the formation of Si crystallites. The fact that the intensity of L(T)O phonon mode gets higher for the deposition at 350°C (note the 0.1 multiplication factor) demonstrates that the average size of the crystallites enlarges at higher temperatures. However, this temperature is still low if compared to the growth temperature of crystalline Si which usually exceeds 1000°C [99]. Such low crystallization temperature could be surprising, but it can be easily understood if a surface mediation by the metal atoms
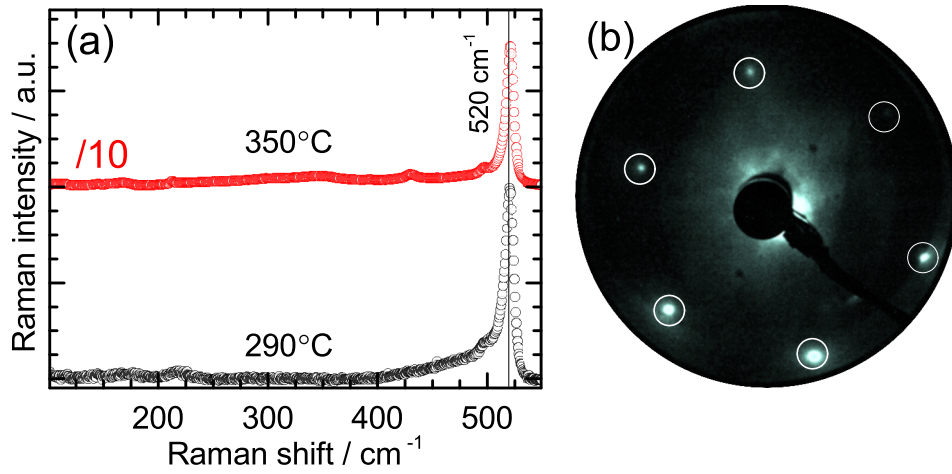
Figure 4.4: (a) Raman spectra of samples deposited at 290°C and 350°C. (b) LEED pattern obtained after the Si deposition at 350°C. $E_{el}$ = 55 eV. White circles mark the integer order spots of Ag(111)-1×1.

is considered. The metal mediation implies the inter-diffusion of the metal and non-metal atoms. In the case of the infusible components such as silver and silicon, the diffusion eventually leads to a separation rather than alloying of the crystalline phases. For a Si-Ag layered system a crystallization temperature as low as 400°C has been reported [100, 101]. These results are in agreement with the low-energy electron microscopy observations [102] and Auger electron spectroscopy measurements [39], which demonstrated a dewetting process of the Si layer from the Ag(111) surface above ∼ 300°C. Hence, a temperature of ∼ 300°C marks the high temperature limit for 2D Si layer formation on Ag(111), where a 2D-to-3D phase transition takes place. This leads to a conclusion that the reports of an almost perfectly ordered 2D Si layer on Ag(111) at almost 400°C must be declared as wrong [103]. According to the Raman results, 3D phase starts to develop for temperatures below 300°C, while the complete transition occurs around this temperature. Surface impurities of the substrate can produce local temperature variations, which can cause a localized dewetting of the Si atoms. Obviously, the rate of this phase transition is solely determined by the temperature. Therefore, one may expect to detect the presence of the bulk-like Si for the samples at temperatures below 300°C. Such blurred borders of the phase modifications add to the complexity of the phase diagram of the Si deposition onto Ag(111).

## 4.2 Two-dimensional Si structure formation

As mentioned in the section 4.1, the temperature value for the formation of 2D Si structures is 220°C. This temperature is not sharp, however, a purely single-phase 2D structure (with a (3×3)/(4×4) symmetry) at the full ML coverage can be obtained specifically at this temperature [15]. Another, high-temperature, limit of 2D Si structure formation is found at 280°C, where another single-phase 2D structure with partial symmetry of "$(2\sqrt{3}\times2\sqrt{3})$R30°" forms [39]. It can be seen in Fig. 4.1 that the Raman spectra of the samples prepared at these two temperatures substantially differ, which suggests the apparent structural differences of these 2D structures, but could also be related to a co-existence of the several phases on Ag(111), which will be discussed later. Despite that this dissimilarity can be immediately recognized, its understanding is only possible if the Raman spectrum of each phase is fully disclosed.

**Epitaxial $(3 \times 3)/(4 \times 4)$ silicene**

As discussed in Chapter 2, the archetypical epitaxial (3×3)/(4×4) silicene layer is formed on the Ag(111) surface at a deposition temperature of 220°C. The overview Raman spectrum of the sample prepared under these conditions is shown in Fig. 4.5(a). It exhibits distinct Raman bands at 175, 216, and 514 cm$^{-1}$ as well as a very broad shoulder at the low-energy side of the peak at 514 cm$^{-1}$. While narrow peaks listed underline the crystalline nature of epitaxial silicene, the presence of the broad bands at 350 cm$^{-1}$ and 480 cm$^{-1}$ is associated with the co-existence of smaller amounts of amorphous Si (a-Si). Indeed, one can show that only Raman bands of amorphous silicon remain in the Raman spectrum after the oxidation of the epitaxial silicene sample. The Raman spectra of the sample before and after the oxidation are shown in Fig. 4.5(b). The sharp Raman bands at 175 and 216 cm$^{-1}$, as well as the one 514 cm$^{-1}$ are not visible in the spectrum of the oxidized structure, whereas the broad band remains. This implies that epitaxial silicene is not stable against the ambient atmosphere, while amorphous silicon is, as it has already been demonstrated previously. The chemical instability of epitaxial silicene in ambient atmosphere has been reported by X-ray photoemission spectroscopy measurements, which also find a Si-O component in the Si 2p core-level emission line after the oxidation [97] and X-ray absorption spectroscopy experiments [104]. Consequently, the broad Raman band at 480 cm$^{-1}$ is not related to the relaxation of the momentum conservation law in an epitaxial silicene layer [105, 106].

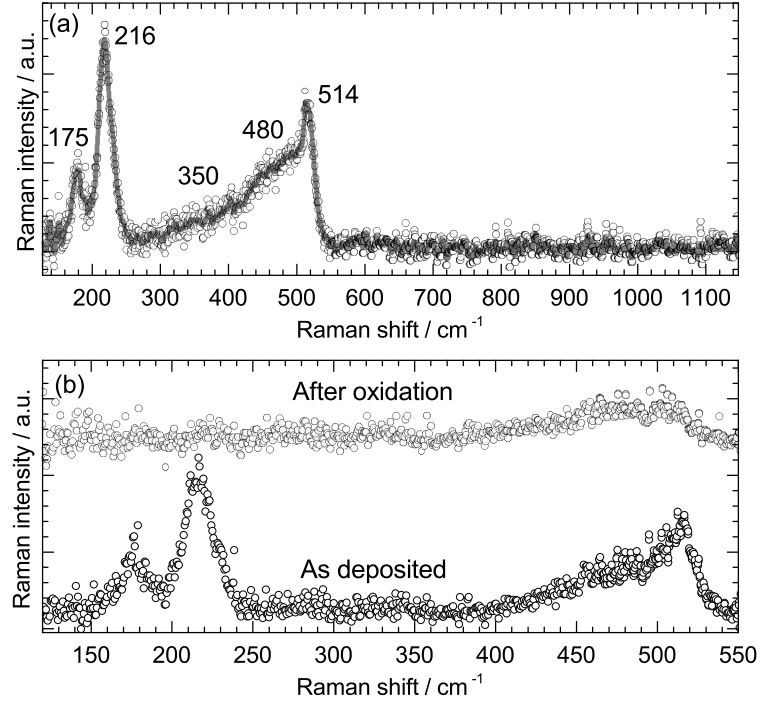Figure 4.5: (a) Raman spectrum of $(3 \times 3)/(4 \times 4)$ silicene up to 1200 cm$^{-1}$. The broad shoulders around 350 and 480 cm$^{-1}$ are associated with small amounts of co-existing a-Si. (b) Raman spectra of $(3 \times 3)/(4 \times 4)$ silicene layer on Ag(111) before and after oxidation.

The small intensity of the a-Si signature indicates that only a minor amount of a-Si is formed at defective substrate areas. To obtain the pure signature of epitaxial $(3 \times 3)/(4 \times 4)$ silicene in Fig. 4.6(a), the spectrum of a-Si was subtracted from the spectrum, which is shown in Fig. 4.5(a). This spectrum was subtracted after matching the intensity of the broad band at 480 cm$^{-1}$ in the Raman spectra of epitaxial silicene. After the subtraction, a low-intense broad band around 410 cm$^{-1}$ is seen in the spectrum. According to its energy, it can be a second-order phonon band of the intense mode at 216 cm$^{-1}$. Polarization-dependent Raman measurements were performed in order to determine the selection rules of the observed modes at 175 cm$^{-1}$, 216 cm$^{-1}$, and 514 cm$^{-1}$. For this, two scattering geometries: $\bar{z}(xx)z$ and $\bar{z}(yx)z$ (Porto notation), *i.e.* parallel and crossed polarisations, respectively, were utilized. As for the sample with amorphous silicon, the axes represent the sample coordinate system, where the z axis is normal to the substrate surface, while x (aligned with the Ag [-110] direction) and y represent the in-plane axes. In figure 4.6(b) the Raman spectra for both scattering configurations are plotted together with their fits. The two Raman modes at 175 cm$^{-1}$ and 216 cm$^{-1}$ are clearly visible in parallel geometry but they entirely vanish in
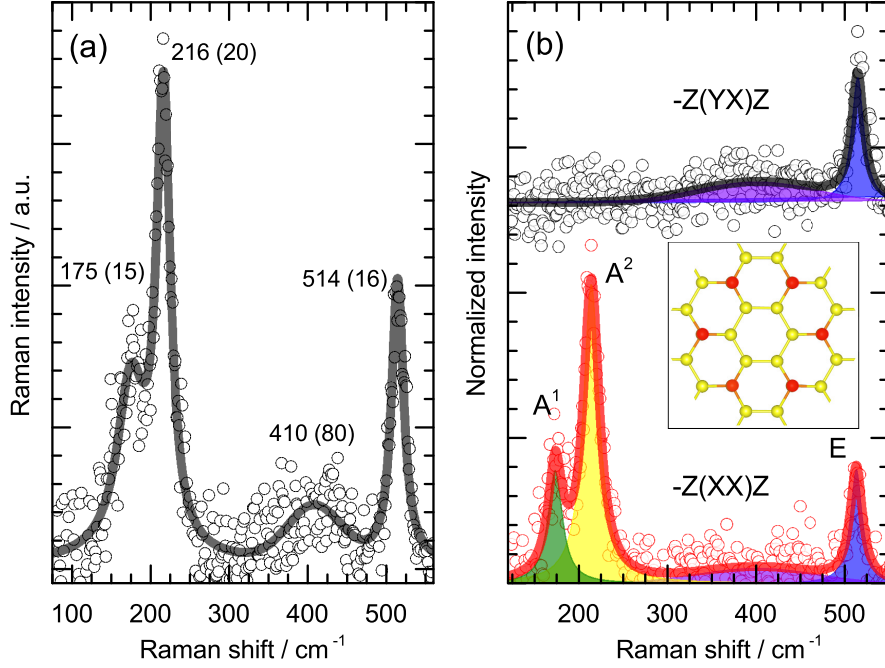
Figure 4.6: (a) Raman spectrum of $(3 \times 3)/(4 \times 4)$ silicene after the subtraction of a-Si signature. Raman bands are noted by the spectral positions (frequencies); their linewidths are shown in brackets. (b) Related Raman selection rules for parallel $-z(xx)z$ and crossed $-z(yx)z$ scattering configurations. Inset: the Wigner-Seitz cell of the $(3 \times 3)/(4 \times 4)$ structure. The figure is adapted from Ref. [54].

crossed scattering configuration. At the same time, the Raman mode at 514 cm$^{-1}$, as well as the broad band at 410 cm$^{-1}$ are present in both polarization configurations. Such a behaviour is obviously governed by the selection rules of these modes. Moreover, it suggests that the lattice vibrations, which are associated with these modes, possess different symmetries. The $(3 \times 3)/(4 \times 4)$ structure of the epitaxial silicene layer belongs to the $C_{6v}$ symmetry point group [44], which has the following possible Raman-active mode symmetries: $A(z)$, $E_1$, and $E_2$. The Wigner-Seitz cell of epitaxial silicene, shown in the inset of Fig.4.6(b), nicely demonstrates the symmetry group assignment. The Raman tensors of the $C_{6v}$ group (see section3.2) dictate that the Raman modes with A symmetry can be seen only in the spectrum of parallel scattering configuration, whereas the Raman modes with E symmetry are visible in the spectra of both configurations. The polarization-dependent Raman results conclusively show that the modes at 175 cm$^{-1}$ and 216 cm$^{-1}$ are fully symmetric vibrations and are assigned to an $A$ symmetry, denoted as $A^1$ and $A^2$, respectively. A mode similar to $A^2$ was also observed by *in situ* Raman measurements at 77 K and assigned to light

scattering from domain boundaries [106]. Hence it was attributed as a '*D* band', by analogy to graphene. This, however, is fully contradictory to the results demonstrated here. The clear selection rules of $A^1$ and $A^2$ modes rule out such interpretation, since the polarization dependence should not be observed for the light scattering from the domain boundaries since the boundaries would break the long-range translational symmetry in the 2D crystal. The Raman band at 410 $cm^{-1}$ shows rather weak sensitivity to a polarization, which supports its assignment as a second-order phonon band. The mode at 514 $cm^{-1}$ has a clear *E* type of symmetry due to its polarization dependence. This phonon mode was also reported in previous *ex situ* [105] and *in situ* [106] Raman measurements at 516 $cm^{-1}$ and 530 $cm^{-1}$, respectively. The blueshift in the latter case can be partly related to the lower temperature of 77 K during the measurements but the total shift is too large to relate it solely to thermal effects. In any case, selection rules finally provide the experimental evidence for the *E* symmetry of this mode.

It is noteworthy that the spectrum of epitaxial $(3 \times 3)/(4 \times 4)$ silicene is dominated by phonons with an *A* symmetry. *A* modes do not exist in diamond-like Si [107, 108] or other bulk Si forms. For silicene, as a 2D material, the translational symmetry is broken perpendicular to the lattice plane. Therefore, the phonon triple degeneracy at the $\Gamma$ point is lifted, as it was shown by theoretical calculations for the phonon dispersion of free-standing silicene [53, 109, 110]. According to the simulations, the former TO phonon mode of bulk Si shifts towards a lower energy. Moreover, group theory analysis shows that free-standing silicene has Raman-active modes of *A* and *E* symmetries, unlike bulk Si, which has only one zone-centre Raman mode of *F* symmetry [111]. The existence of *A* modes in $(3 \times 3)/(4 \times 4)$ silicene on Ag(111) is a conclusive indication of the 2D character of epitaxial silicene. Also from the group theory analysis [111], the out-of-plane displacement of Si-atoms, a vibrational mode that is supported by the buckling and the out-of-plane oriented hexagons of the $(3 \times 3)/(4 \times 4)$ atomic structure, should be manifested by the *A* modes. Such modes were not observed for the absolutely planar graphene sheets.

The symmetries of the observed Raman modes of epitaxial silicene are in good agreement with theoretical expectations for free-standing silicene. Their frequencies show less agreement with phonon dispersion calculations for the free-standing material [53, 109, 110]. According to DFT calculations, there are three optical phonon branches at $\Gamma$: a ZO, flexural, mode, related to out-of-plane optical phonons, and energetically degenerate TO and LO phonons. It is noteworthy that the position of the ZO branch at $\Gamma$, is actually close to the experimentally
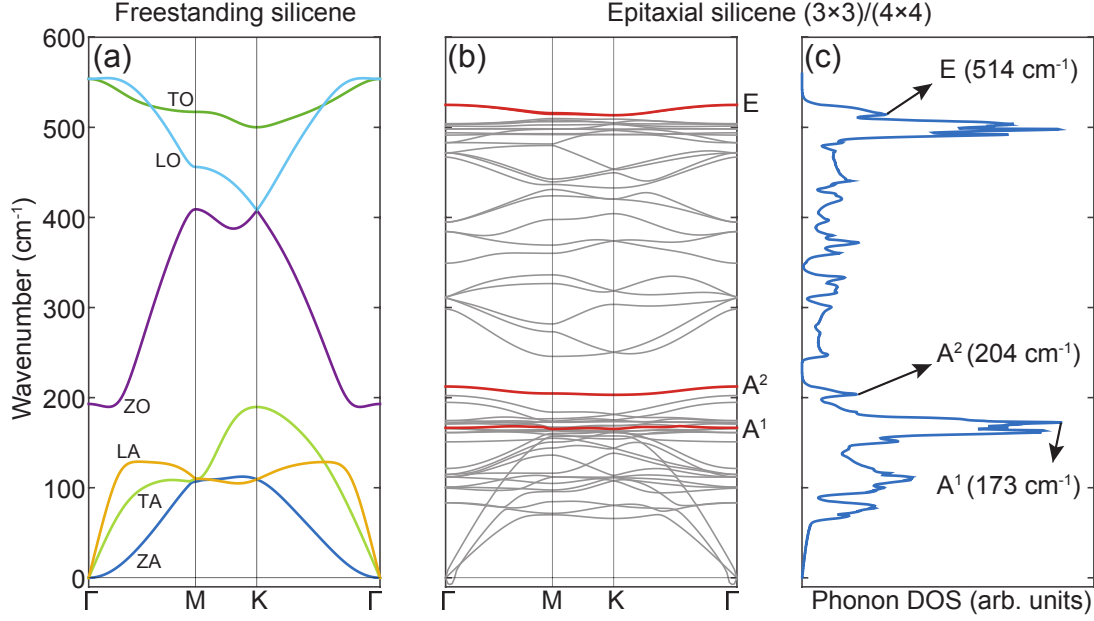
Figure 4.7: (a) Phonon dispersion of free-standing buckled silicene. Longitudinal, transverse and out-of-plane acoustic (and optic) modes are denoted as LA, TA and ZA (LO, TO and ZO), respectively. (b) Phonon dispersion of (3×3) silicene calculated by including the effect of the Ag(111) substrate. The Raman active modes are shown by red lines. The small imaginary frequencies near the Γ point are numerical artefacts. (c) Calculated phonon density of states of (3×3) silicene on Ag(111). The DFT simulations are performed by Dr. S. Cahangirov and Dr. H. Sahin. The figure is adapted from Ref.[54].

observed *A* modes. At the same time, the degenerate TO/LO branches (562 cm$^{-1}$ [109], $\sim$ 550 cm$^{-1}$ [110], $\sim$ 556 cm$^{-1}$ [53]) show no match to the *E* mode of epitaxial silicene (514 cm$^{-1}$). Such a disagreement is explained by the fact that epitaxial silicene shows a superstructure, which differ to a conceptual lattice of free-standing silicene. As explained, this is due to the significant interaction between the Si adlayer and the substrate. Moreover, the electronic structure of epitaxial silicene is also different [49]. Thus the match of energy position of Raman-active modes is actually not expected at all. In this respect, the close energies of the ZO modes of epitaxial silicene and ZO mode of free-standing silicene are even more remarkable, which apparently implies their less intense coupling to the supporting substrate. This, however, does not shed the light on the presence of two A modes, which is connected to the influence of the substrate for certain.

To resolve these discrepancies, *ab initio* phonon calculations of the epitaxial $(3 \times 3)/(4 \times 4)$ silicene (including the presence of the Ag substrate) were performed. In Fig. 4.7, the phonon dispersions of free-standing silicene and epitaxial silicene on Ag(111) are presented. The

55

dispersions were obtained by DFT simulations (the details are described in Ref. [54]). It is clearly seen that the interaction with the substrate alters the phonon dispersions significantly when compared the phonon dispersion of these two crystals. The phonon dispersions of epitaxial silicene become flat compared to the free-standing case (Fig. 4.7(a)). Such flattening is a result of the 3×3 reconstruction that breaks the symmetry and forms protruding triplets of Si atoms that are rather isolated from each other. The triplets are involved in all vibrational modes but due to the isolation the modes become flat. The calculated phonon density of states (DOS) is presented in Fig. 4.7(c). The DOS is not directly correlated to the experimentally observed Raman spectra since it also includes the contributions from the non-Raman-active phonons. The analysis of the symmetries of the optical phonon modes below 220 cm$^{-1}$ showed that only two normal modes can belong to the irreducible representation of A symmetry. These modes are highlighted by red lines and denoted as A$^1$ and A$^2$ in Fig. 4.7(b). Their relation to an A type of symmetry will be described later on the basis of the atomic motion pattern. The DOS features, which are attributed to the modes A$^1$ and A$^2$, are centred at 173 cm$^{-1}$ and 204 cm$^{-1}$, respectively. The frequency of the normal mode, which can be assigned to a degenerate LO/TO mode at the Γ-point, is significantly lowered upon the superstructure formation, which is in excellent agreement with the experimental data. Symmetry analysis of the corresponding motion pattern provides its relation to the irreducible representation E$_2$. This degenerate LO/TO mode is also highlighted by the red line and denoted as E in Fig. 4.7(b). The DOS peak, corresponding to this mode, is at 514 cm$^{-1}$ (Fig. 4.7(c)). It is noteworthy that E mode phonon dispersion is rather separate from others giving a stand-alone contribution in the phonon DOS and thus cannot be mistaken or missed. The calculated DOS features which correspond to the Raman-active A$^1$ and the E modes are in excellent agreement with the experimental data. On the contrary, the normal mode which is assigned to the A$^2$ mode is redshifted by 12 cm$^{-1}$ with respect to the experimental A$^2$ mode. This shift may be due to some involvement of Ag atoms that approximate DFT calculation (that separates Si and Ag vibrational modes) could not capture.

The atomic motion patterns corresponding to A$^1$, A$^2$ and one of the doubly degenerate E Raman modes are demonstrated in Fig. 4.8. For the A$^1$ mode, the protruding six atoms (forming the "flower pattern") and the six atoms connected to them to form two hexagons are moving down while the remaining six atoms move up. One can imagine using the Wigner-Seitz cell inset of Fig. 4.6(b), where the six atoms forming the hexagon in the
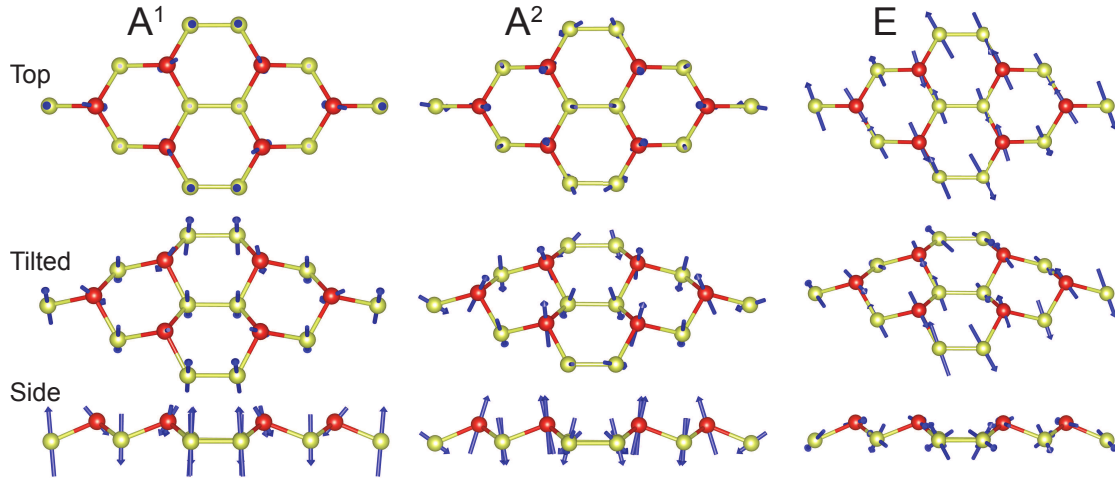
Figure 4.8: Top, tilted and side views of eigenvectors of calculated phonon modes identified as the experimentally observed Raman active modes. The DFT simulations are performed by Dr. S. Cahangirov and Dr. H. Sahin. The plot is adapted from Ref.[54].

middle moving up while the rest are moving down. For the $A^2$ mode, the protruding six atoms move up while the remaining twelve atoms move down. The $A^1$ and $A^2$ modes clearly show the character of the ZO, flexural, mode, similarly of free-standing silicene. For the E mode, the three protruding atoms in the left half of the unit cell move in a certain in-plane direction while the atoms surrounding them move in the opposite direction. Consequently, the atoms in the right half move opposite to the corresponding atoms in the left half of the $(3 \times 3)/(4 \times 4)$ cell. Hence, both A phonon modes are dominated by out of plane and the E mode by in plane atomic displacements supporting the interpretation of experimentally observed Raman selection rules. The agreement allows the Raman modes observed experimentally to be associated with the vibrations described in Fig. 4.8. This subsequently rules out several claims for the nature of epitaxial silicene, such as Si-Ag alloying [93]. Raman spectroscopy results give no indication for Si-Ag vibrational modes, resulting from the inter-atomic bonding between these two species. Theoretical calculations show that the Si-Ag stretching vibration should evolve at about 90 cm$^{-1}$ [112]. Besides the interaction with the Ag substrate, which has, indeed, a significant effect on the structure and vibrational modes of silicene, the presence of Si-Ag bond is not observed neither inside the $(3 \times 3)/(4 \times 4)$ silicene layer, nor between the Si adlayer and the Ag(111) substrate.
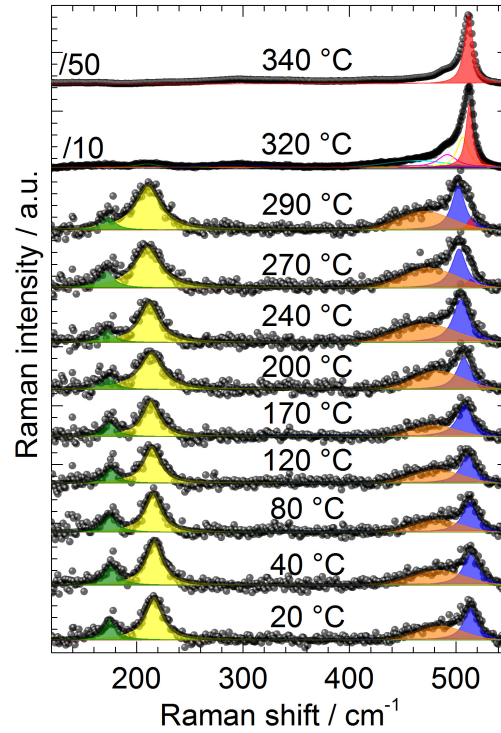
Figure 4.9: Series of Raman spectra of $(3 \times 3)/(4 \times 4)$ silicene measured at increasing temperatures. The figure is adapted from Ref. [54].

## Temperature properties of epitaxial $(3 \times 3)/(4 \times 4)$ silicene

Figure 4.9(a) shows a series of Raman spectra measured during the annealing of the epitaxial $(3 \times 3)/(4 \times 4)$ silicene layer on Ag(111). The Raman spectra were recorded in incremental temperature steps from room temperature to 500°C. This experiment was reproduced 4 times giving the similar results within the experimental errors. For temperatures up to ~300°C the overall spectral line shape remains unchanged and all modes shift almost equally towards lower wavenumbers with increasing temperature. Such temperature dependence is qualitatively very similar to the ones of graphene [113], $MoS_2$ [114], or bulk Si [108, 115] where the Raman modes, related to optical phonons, shift towards lower energies. At a temperature slightly above 300°C the spectrum undergoes a peculiar change: the E mode, which is found at 514 cm$^{-1}$ at room temperature, broadens considerably as a result of a new component appearing at around 520 cm$^{-1}$ (measured at room temperature). For higher temperatures this new mode increases and finally dominates the spectra. The disappearance of Raman modes of epitaxial silicene and the domination of the mode at 520 cm$^{-1}$ clearly demonstrate that a structural phase transition takes place at temperatures around 300°C in agreement with earlier results [39, 102]. According to the Raman spectra, the silicene layer transforms into a phase which exhibits a bulk Si-like Raman spectrum characterized
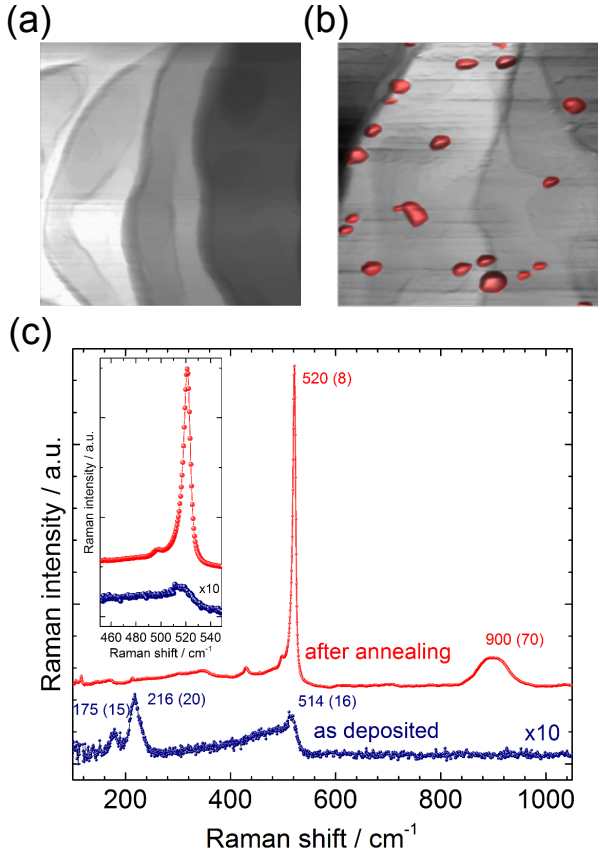
(a)

(b)

(c)



Figure 4.10: (a) AFM image (2 $\mu$m $\times$ 2 $\mu$m) of the initial Ag(111) surface. (b) AFM image (2 $\mu$m $\times$ 2 $\mu$m) after annealing the (3$\times$3)/(4$\times$4) silicene layer to 500°C with small islands (in red). (c) Overview Raman spectra of the epitaxial silicene before and after annealing to 500°C both measured at room temperature (FWHM in brackets). Inset: detailed Raman spectra (450 - 550 cm$^{-1}$). The figure is adapted from Ref. [54].

by the L(T)O mode at 520 cm$^{-1}$ with an asymmetric shoulder on the lower energy side. In the respect of thermal instability of epitaxial silicene, it is important to mention that free-standing silicene was, on the contrary, predicted to survive the temperatures up to 1500 K [116].

AFM images acquired at room temperature after the annealing procedure to 500°C (Fig. 4.10(a,b)) show the formation of small islands with an average size of (10 ± 8) nm, distributed over the Ag surface. These islands are not observed on the initial Ag(111) surface (Fig. 4.10(a)) or after formation of the epitaxial silicene layer and are, thus, assigned to Si crystallites. This assignment is justified since Si nanoparticles show a L(T)O mode around 520 cm$^{-1}$ with an asymmetric shoulder, which is caused by spatial phonon confinement in particles smaller than 7 nm [117], while their size distribution explains the broad linewidth of this mode. In Fig. 4.10(c) the room temperature Raman spectrum of the same sample is shown in a spectral range between 100 cm$^{-1}$ and 1000 cm$^{-1}$. Note that in this instance, *i.e.* after formation of Si crystallites, a broad band (2nd-order of TO mode) centred around 950 cm$^{-1}$ can be seen, which is not the case for the epitaxial silicene layer. This means

that the occurrence of this band is indicative for the formation of Si crystallites. This result elucidates the early Raman spectroscopy results on epitaxial silicene capped under the $Al_2O_3$ layer [105, 118]. Such *ex situ* Raman measurements of epitaxial $(3 \times 3)/(4 \times 4)$ silicene showed the spectra, where the dominating Raman band was found at $516$ cm$^{-1}$. Another prominent Raman band is positioned in the range of $900$ to $1000$ cm$^{-1}$ and assigned to a graphene-like 2D mode. Judged by comparison with *in situ* Raman measurements, such spectra must be related to Si nanocrystallites rather than epitaxial silicene. It is clear that considerable 2TO mode in the Raman spectra recorded *ex situ* suggests the presence of bulk Si on the surface. Consequently, 2TO mode can only be seen, when the first order phonon mode is intense. Such intense Raman band is apparently the one at $516$ cm$^{-1}$. The difference in Raman shifts of this mode to the one of bulk Si ($520$ cm$^{-1}$) is then unclear and cannot be rationally explained. Moreover, it can be assumed that the Si crystallites were formed during Si deposition since the oxidation, which still takes place despite the capping during the *ex situ* measurements should not lead to the crystallization process, but the destruction of the silicene layer. The oxidation of silicene can be concluded from the absence of the dominant $A^2$ mode at $216$ cm$^{-1}$ in the *ex situ* Raman spectra. Such results bring doubts about the Raman results presented in Ref. [119]. In the paper, where the production and characterization of silicene transistor was presented, the survival of epitaxial silicene was tested using the Raman band at $517$ cm$^{-1}$. As shown, this Raman mode has no relation to silicene, but Si crystallites, therefore it cannot be utilized for such purpose. Moreover, the oxidation of epitaxial silicene is very fast process. According to own experiment with *ex situ* Raman measurement, its duration is less than 1 minute. In this respect, it is surprising to observe the IV characteristics of the transistor, which confirm the predicted transport properties of silicene.

Additional evidence for a phase transition can be found by following the evolution of the Raman modes upon heating. The temperature-dependent position of the $E$ mode is depicted in figure 4.11(a). The shift with increasing temperature allows the determination of its thermal coefficient, having a value of $\chi_{silicene} = (-0.030 \pm 0.003)$ K$^{-1}$ cm$^{-1}$. Instead, the thermal coefficient of the L(T)O phonon of the Si nanocrystallites after the phase transition is found to be $\chi_{Si} = (-0.019 \pm 0.003)$ K$^{-1}$ cm$^{-1}$, in good agreement with values reported for diamond-like bulk Si [108, 115, 120]. Note, the determination of the thermal coefficient of silicene is not dependent on absolute temperature and hardly influenced by the external factors such as the underlying Ag substrate. The shift of the other Raman modes of epitaxial
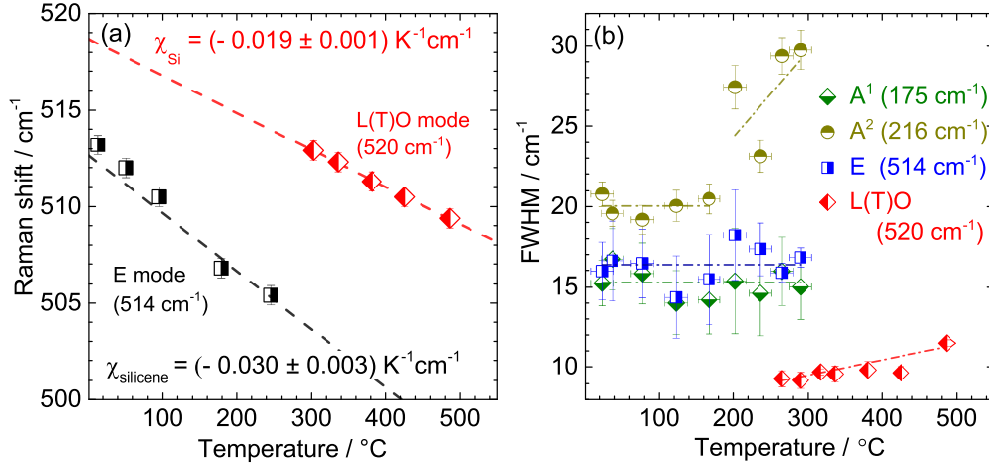
Figure 4.11: (a) Raman shift of the E mode of $(3 \times 3)/(4 \times 4)$ silicene as a function of annealing temperature. (b) Full width at half maximum (FWHM) of the silicene $A^1$, $A^2$, and $E$ and the Si L(T)O Raman modes as a function of temperature (with error bars). The experimental points are linearly fitted (dash-dot lines) and weighted by the error bars. The figure is adapted from Ref. [54].

silicene is similar to the one of the E mode. This reveals that the thermal coefficient of the Raman modes of epitaxial silicene on Ag(111) markedly differs from the one of bulk-like Si. A similar difference is found between graphene (2D) and diamond (3D), where the zone-centre *G mode* of graphene has a higher thermal coefficient compared to the diamond phonon mode [113].

Further information is gained upon studying the evolution of the FWHM of the silicene Raman modes (figure 4.11(b)). While the widths of the $A^1$ ($\sim 15 \, \text{cm}^{-1}$) and the $E$ ($\sim 16 \, \text{cm}^{-1}$) modes remain unchanged up to 300°C, the $A^2$ mode shows a constant width ($\sim 20 \, \text{cm}^{-1}$) for temperatures up to 220°C. For temperatures exceeding 240°C the $A^2$ mode starts to broaden when the L(T)O mode appear in the spectra. Moderate dewetting of Si atoms from the Ag surface creates a local disorder [102], which could be related to the $A^2$ mode broadening. Remarkably, only the $A^2$ mode responds to this structural change, showing similarities to the broadening of the *D* band of graphene upon temperature increase [25]. At temperatures above 300°C, we can only follow the FWHM of the Raman mode at 520 $\text{cm}^{-1}$, as the Raman modes of silicene have disappeared. Its linewidth (FWHM at room temperature: $\sim 6 \, \text{cm}^{-1}$) evolves in a manner, expected for nanocrystalline Si [121]. In contrast to this behaviour expected for a semiconductor crystal, the constant linewidth of the $A^1$, $A^2$, and E Raman modes of epitaxial silicene upon heating inevitably points to a considerable

electron-phonon coupling (EPC). This is due to the fact that the temperature-independent part of the phonon mode linewidth, consistent with the electron-phonon interaction, is bigger than the temperature-dependent contribution from the phonon-phonon interaction [25]. Overall, all observed Raman modes for epitaxial $(3 \times 3)/(4 \times 4)$ silicene show a markedly larger broadening at room temperature than, for example, the L(T)O mode of bulk Si ($\sim 2.4$ cm$^{-1}$). Beside the already mentioned EPC this broadening could also be caused by a loss of crystallinity and lattice disorder or confinement effects due to small domain sizes. However, the very clear polarization dependence of the phonon modes (described above) and the well defined layer periodicity (according to LEED and STM) demonstrate that disorder as an explanation of the phonon peak broadening can be neglected. Phonon confinement could occur if the average domain size of the epitaxial silicene is in the range of a few nm ($\sim 7$ nm for Si allotropes [122]). This would lead to a lifting of momentum conservation which disagrees again with the clear fulfilment of the Raman selection rules. Additionally, the lifting of momentum conservation implies an averaging over the phonon dispersion curves from the $\Gamma$ point towards the Brillouin zone edge. The branches of optical phonons usually have a negative slope around the $\Gamma$ point and such averaging would cause an asymmetry of the phonon modes in the case of a significant slope. Since a peak asymmetry is not observed (as it would be expected for Si allotropes [110]), phonon confinement cannot explain the phonon broadening of epitaxial silicene either. Ultimately, the large linewidth of the silicene phonon modes and their temperature-independent linewidth character indicate a strong electron-phonon coupling in epitaxial silicene. A very similar effect was shown to introduce a significant broadening of $G$ and $G'$ phonon bands of graphene and carbon nanotubes up to $11 - 13$ cm$^{-1}$ [25, 123]. By analogy with the constant width of the $G$ mode of graphene versus temperature, we also observe a constant linewidth with temperature of the $A$ and $E$ modes, which supports the existence of strong coupling. Significant electron-phonon coupling at the $\Gamma$ point was also predicted theoretically for free-standing silicene [109].

The strong EPC is in fact expected for the materials of a semi-metallic nature such as graphene, silicene etc. As it was explained in the chapter 2, their phonon dispersions exhibit cusps (Kohn anomalies), for instance, the LO and ZO phonon branches of free-standing silicene (Fig. 4.7(a)). On the contrary, epitaxial $(3\times3)/(4\times4)$ silicene does not exhibit Kohn anomalies for the Raman-active modes (Fig. 4.7(b)), thus it should not inherently exhibit the strong EPC. Therefore, a considerable EPC, discovered by the temperature-dependent Raman measurements, is an acquired feature. Such claim goes well along with the observations of

its metallic character [48], which originates from the silicene-silver interaction. An attempt to evaluate the EPC values for the phonon modes of epitaxial silicene from the experimental data according to the method, suggested for graphene in Ref. [25], has failed since such parameter as the Fermi velocity is not defined for the epitaxial silicene. Meanwhile, using the parameters of the free-standing silicene obviously leads to the non-reasonable values. Therefore, the question of the exact coupling remains open, while the hints of its significance have been presented. Generally, a strong electron-phonon interaction, especially coupling to the flexural phonons [53] can hinder the application of epitaxial silicene due to the poor ballistic transport properties, but it could be a solid basis for the exotic physical effects such as the tunable superconductivity transition temperature ($T_c$) [124] or valleytronics [20].

In short summary, epitaxial $(3 \times 3)/(4 \times 4)$ silicene is a 2D Si structure of many interesting and important properties and, according to our Raman results, the closest structure to a free-standing silicene.

## 2D Si "$(2\sqrt{3} \times 2\sqrt{3})$" structure

As for the other silicene-related structures, their nature and properties are less studied due to the number of reasons, mentioned in the Chapter 2. Since their structural differences are obvious, when observed in the STM topography images [26], their vibrational structures can also be expected to differ. In this case, Raman spectroscopy can be employed to identify these structures and explain them in terms of the vibrational properties they exhibit. Such assumption was already validated by the Raman spectra, recorded for the samples deposited in the temperature range between 220°C and 280°C (Fig. 4.1). Before the explanation of the processes, which occur during Si deposition at temperatures in the range mentioned, the vibrational properties of "$(2\sqrt{3} \times 2\sqrt{3})$" structure need to be addressed first.

At preparation temperature of approximately 280°C the 2D Si layer with a "$(2\sqrt{3} \times 2\sqrt{3})$" symmetry (Fig. 2.5(c)) can be observed in the corresponding LEED pattern in Fig. 4.12(a). On the contrary to epitaxial silicene, this structure can be grown in a single phase regime. No spots, related to other structures, are detected. Hence, the visible spots are solely related to the "$(2\sqrt{3} \times 2\sqrt{3})$" structure. As for the pattern itself, one can see that the diffraction spots of the "$(2\sqrt{3} \times 2\sqrt{3})$" structure are not aligned along the crystal axes of silver crystal. This is a sign of the layer rotation by 30° in respect to the 1×1 surface reconstruction of the substrate. Moreover, some spots are actually doubled and tripled. It is attributed to the Moiré-like structure, observed in STM images [39, 125]. Nevertheless, the
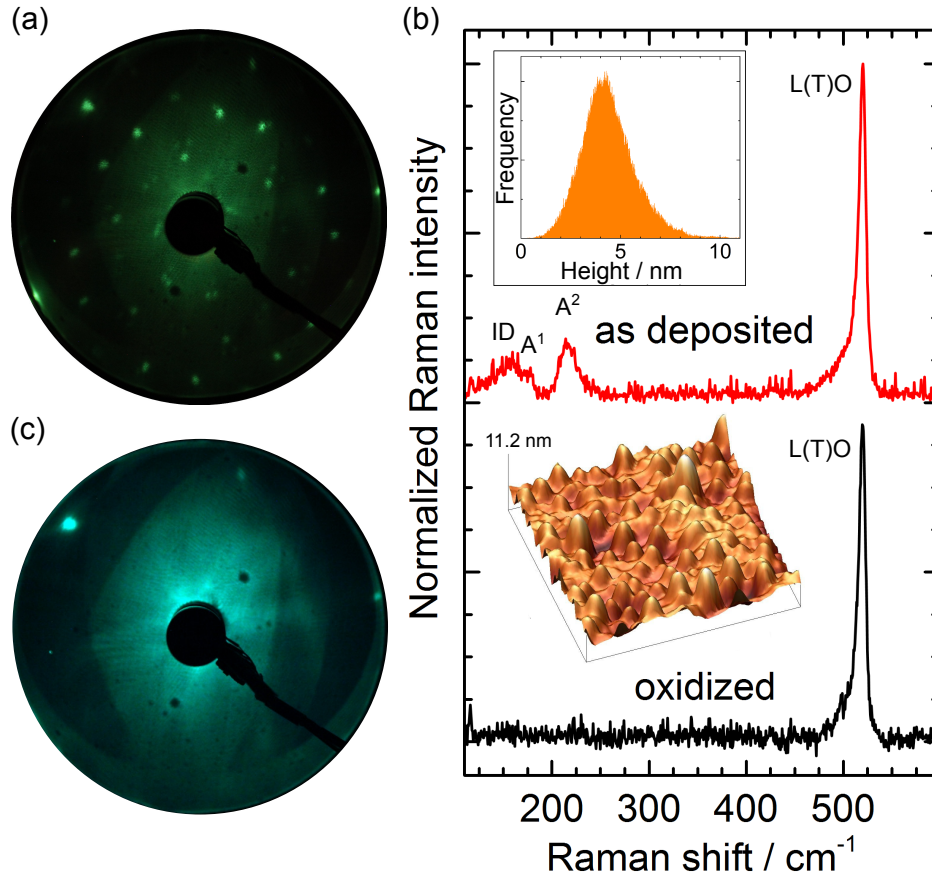
Figure 4.12: (a) The LEED pattern, obtained after Si deposition at 280°C. $E_{el}$ = 32 eV. (b) Raman spectra of the sample with the "(2√3×2√3)" structure after deposition and after *ex situ* oxidation. Insets: height distribution of the small features observed in the AFM topograph (top); *ex situ* AFM image (1 $\mu$m × 1 $\mu$m) of the Ag(111) surface, measured after the oxidation (bottom). (c) The LEED pattern, obtained after the oxidation of the sample prepared at 280°C. $E_{el}$ = 32 eV.

diffraction pattern of this structure indicates its 6-fold symmetry, which is characteristic to honeycomb lattices.

The impression of the Moiré structure in STM images originates from the locally ordered areas surrounded by the distorted or disordered zones [39]. The ordered areas appear brighter in filled states STM images, thus mimicking a Moiré pattern. Because of the inherent intrinsic disorder (ID) it is not reasonable to assign any symmetry to this structure except the one, which describes the ordered zones. Therefore, this phase is referred to as "(2√3×2√3)". The Raman spectrum of the sample prepared at 280°C is shown in Fig. 4.12(b). It exhibits similar Raman bands such as $A^1$ and $A^2$ modes as the ones observed

for the $(3 \times 3)/(4 \times 4)$ structure, a dominating spectral feature at 520 cm$^{-1}$ with a broad shoulder at 495 cm$^{-1}$ as well as a new Raman mode around 155 cm$^{-1}$. The visibility of A modes in the spectrum testifies the presence of E mode at 514 cm$^{-1}$, which can only be surmised due to an intense shoulder of the peak at 520 cm$^{-1}$. In order to verify the evident similarities with $(3 \times 3)/(4 \times 4)$ 2D structures, a similar set of experiments was carried out. The origin of the spectral signatures of the "$(2\sqrt{3} \times 2\sqrt{3})$" structure can be elucidated after the oxidation of the sample. After oxidation no LEED diffraction spots, except the integer Ag(111) ones can be seen (Fig. 4.12(c)). In Fig. 4.12(b) the Raman spectra of the "$(2\sqrt{3} \times 2\sqrt{3})$" structure before and after oxidation are shown. The oxidized structure clearly exhibit no Raman bands, related to the 2D layer, but the intense band at 520 cm$^{-1}$ and the low-energy shoulder centred around 495 cm$^{-1}$. *Ex situ* AFM measurements of the same sample, show protrusions with an average height of 4.4 nm ((Fig. 4.12(a), top inset)) and a lateral size of up to 100 nm (Fig. 4.12(a), bottom inset). In combination with the Raman results of the oxidation of the "$(2\sqrt{3} \times 2\sqrt{3})$" structure, it can be stated that these protrusions are diamond-like Si crystallites. Their broad size distribution explains the linewidth of the Raman band at 520 cm$^{-1}$: the biggest crystallites ($> 7$ nm) exhibit the intense L(T)O phonon mode, whereas the small ones ($< 7$ nm) are responsible for its large linewidth. The formation of such crystallites is clearly temperature-dependent; it is the only growth process when the temperature reaches 300°C, *i.e.* the limit of the 2D Si layer growth mode on Ag(111). The Raman and AFM results confirm the co-existence of Si crystallites and of the "$(2\sqrt{3} \times 2\sqrt{3})$" structure at temperatures between 250°C and 300°C.

To substantiate the understanding of the "$(2\sqrt{3} \times 2\sqrt{3})$" structure polarization dependent Raman measurements have been performed. Fig. 4.13 shows Raman spectra of a sample with the "$(2\sqrt{3} \times 2\sqrt{3})$" structure in parallel (Porto notation: *-z(xx)z*) and crossed (*-z(yx)z*) geometries. According to the selection rules for the six-fold symmetry, the unpolarized (degenerate) modes are measured in both parallel and crossed geometries, while the polarized vibrational modes are visible only in the parallel configuration. One notices that only A modes at 175 and 216 cm$^{-1}$ are missing in the crossed configuration, while the Raman modes at 155, 514 (E mode), and 520 cm$^{-1}$ are present in both cases. The polarization dependence of A and E modes fully reproduces previous results for epitaxial $(3 \times 3)/(4 \times 4)$ silicene. The triple-degenerate Raman mode at 520 cm$^{-1}$ is not sensitive to the polarization because of the degeneracy. The presence of polarized modes in the Raman spectrum of the "$(2\sqrt{3} \times 2\sqrt{3})$" structure at the same positions as the ones of epitaxial $(3 \times 3)/(4 \times 4)$ silicene suggests
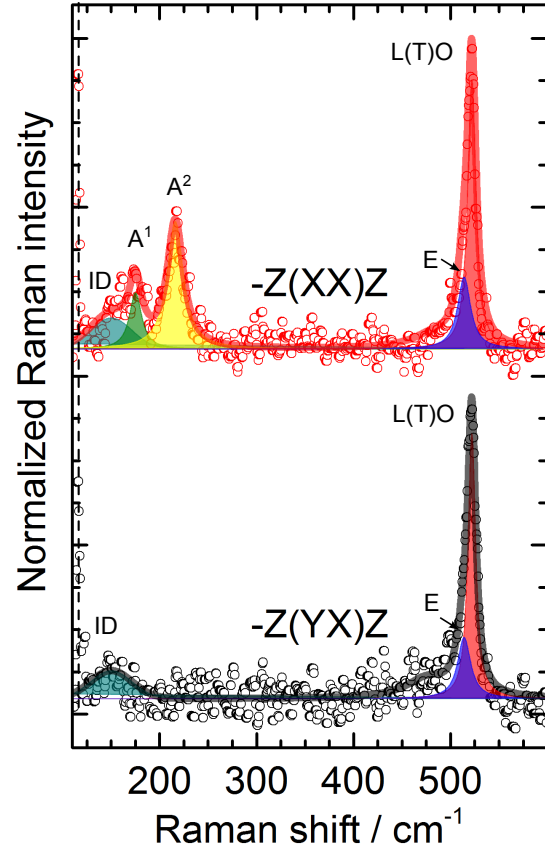
Figure 4.13: Polarization-dependent Raman spectra measured from the 280°C sample, recorded in parallel $-z(xx)z$ and crossed $-z(yx)z$ scattering configurations. The dashed vertical line marks the Ar$^+$ plasma line.

structural similarities of these materials. Indeed, the bright hexagons (Fig.2.5(c)) are nicely ordered and, therefore, can provide the similar spectral response. The E mode under the low-energy shoulder of the L(T)O phonon mode can be surmised. The Raman band at 155 cm$^{-1}$ is present in both geometries, which hints for its disorder-related origin, since only the vibrations of ordered crystalline structures follow the Raman selection rules. Its broad linewidth of 30 cm$^{-1}$ further corroborates this assignment. According to its frequency, this mode can be related to the softening of the A$^1$ mode, in connection with the intrinsic disorder (ID) of the "$(2\sqrt{3}\times2\sqrt{3})$" structure. As this Raman mode is the one which distinguishes the "$(2\sqrt{3}\times2\sqrt{3})$" structure from epitaxial silicene, it can be considered as its marker. Due to its evident relation to the intrinsic disorder of the "$(2\sqrt{3}\times2\sqrt{3})$" superstructure, it is referred to as the "ID" mode. The Raman spectrum of the sample prepared at 280°C and recorded via *in situ* Raman measurement can be compared to the ones, measured in *ex situ* experiments [105, 126]. The only spectral feature, which is present in both measurements, is the Raman band at 520 cm$^{-1}$. As shown, this is a manifestation of Si crystallites co-formed with the "$(2\sqrt{3}\times2\sqrt{3})$" structure. Therefore, it cannot be used for the interpretation of the
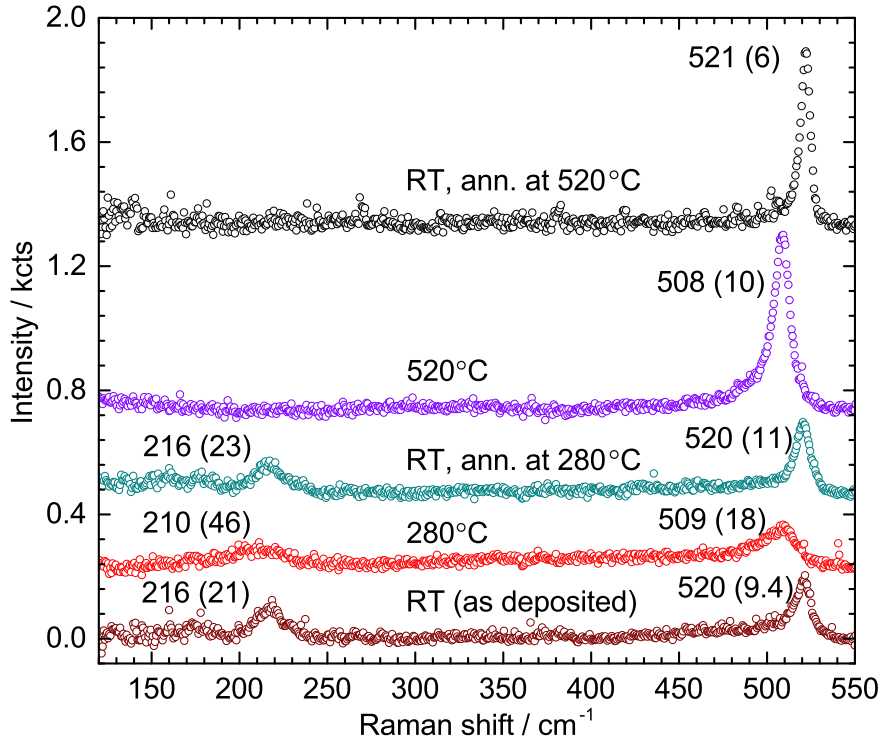
Figure 4.14: Raman spectra of the sample deposited at 280°C recorded during and after the post-annealing at different temperatures. The main Raman bands are marked by their spectral position. FWHMs are shown in parenthesis.

Si honeycomb lattice. As in the case of epitaxial $(3 \times 3)/(4 \times 4)$ silicene, *ex situ* Raman measurements show neither the modes, characteristic for the ordered phases, nor the ones of disordered 2D layers (ID mode). Therefore, it indicates that *ex situ* Raman measurements are incapable to be utilized for the investigation of silicene, while the proper protection of the 2D Si sheets has yet to be found.

The disordered nature of "$(2\sqrt{3}\times2\sqrt{3})$" structure is surprisingly unusual, since it is known that high temperature deposition results in the structures with the better crystalline quality. The same consideration applies to the high-temperature treatment, which can improve the crystalline order of the classic semiconductors like bulk silicon [122]. In order to test this assumption, the Raman spectra of the "$(2\sqrt{3}\times2\sqrt{3})$" structure were recorded during the post-annealing of the sample (Fig. 4.14).

The Raman spectrum recorded at RT has both 2D Si-related A bands as well as a prominent L(T)O phonon. During the annealing at 280°C (which was also the deposition temperature of this sample) the Raman bands shift towards the low energies and synchronously broaden.

The spectrum recorded after cooling to room temperature exhibits the same modes, however, the intensity ratio is slightly changed: the bulk-Si phonon mode has enlarged while the intensity of the $A^2$ mode is decreased. Such evolution of the spectrum is in accordance with the interpretation of the 2D-to-3D phase transition, which the Si atoms experience at temperatures starting from 250°C. Hence, some amount of the Si atoms are dewetted from surface at 280°C forming the 3D phase. However, it is clear that the structure is not fully destroyed since the A modes are still visible in the spectrum. The Raman spectra of the sample annealed up to 520°C (the melting point of the Ag substrate in UHV) during as well as after heating show only one Raman band, which is the L(T)O phonon mode, suggesting the phase transition is complete. This proves that neither $(3 \times 3)/(4 \times 4)$ silicene, nor "$(2\sqrt{3}\times2\sqrt{3})$" structure are stable against high temperatures.

## "Mixed phase"

Once the Raman signature as well as the properties of "$(2\sqrt{3}\times2\sqrt{3})$" structure are investigated, the issue of the "mixed phase" can be explained to complete the picture of Si deposition on Ag(111). The sample with a "mixed phase" contains the 2D islands of two single-phase structures ($(3 \times 3)/(4 \times 4)$ silicene and "$(2\sqrt{3}\times2\sqrt{3})$") formed on the Ag(111) surface. Such sample can be prepared in the temperature range above 220°C and below 280°C. The domains of the subsidiary ($(\sqrt{7}\times\sqrt{7})R \pm 19.1°/(\sqrt{13}\times\sqrt{13})R \pm 13.9°$) phases can also accompany the single-phase structures. The Raman spectral signature of ($\sqrt{13}\times\sqrt{13}$) phases has not yet been addressed. The inability to grow this structure only and, thus, separate it from the dominant phases does not allow the systematic study of their vibrational properties. However, it can be conjectured that their manifestation in the Raman spectra is very similar to the one of epitaxial silicene. Such claim is corroborated by the fact of clear selection rules in epitaxial $(3 \times 3)/(4 \times 4)$ silicene. This would not be so if the ($\sqrt{13}\times\sqrt{13}$) domains contribute to the Raman bands observed unless such contribution is identical. Moreover, STM-based study shows that these subsidiary phases can be rationalized considering the high concentration of point defects in the silicene lattice. This can explain their appearance in STM images suggesting their analogous origin to epitaxial silicene, but of a defective kind. In such case, their Raman signature cannot be expected to contain sharp peaks, but broad and weak ones. In order to confirm such contemplation, the Raman measurements has to be performed on a single ($\sqrt{13}\times\sqrt{13}$) domain, which may be possible with *in situ* tip-enhanced Raman spectroscopy (TERS) method.
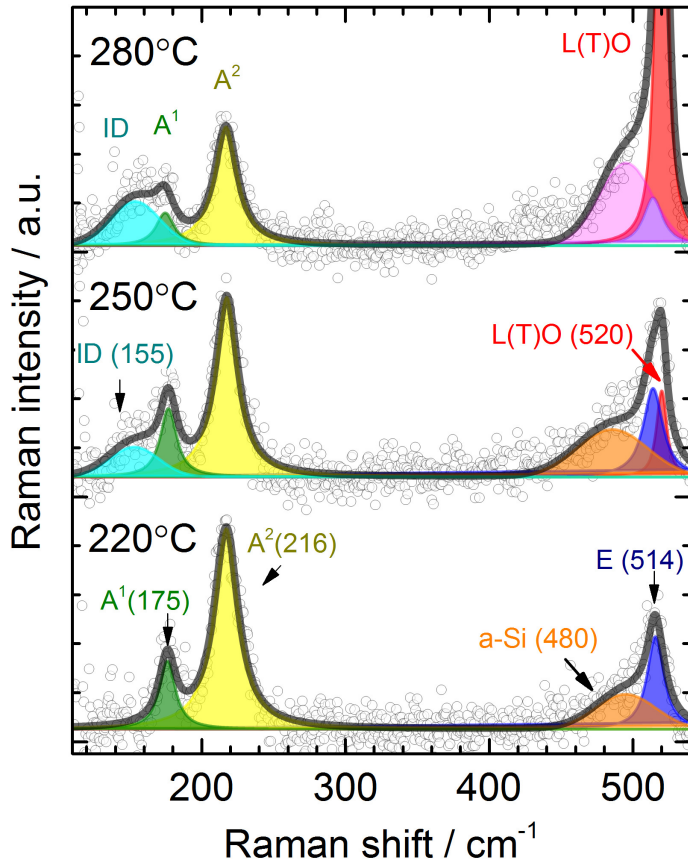
Figure 4.15: Fitted Raman spectra of silicene-related structures: dominant (3×3)/(4×4) (epitaxial silicene) (220°C), "mixed phase" (250°C), and "$(2\sqrt{3}\times2\sqrt{3})$" phase (280°C). The experimental data are shown as circles, whereas the smooth curves overlaid are the envelopes of all features observed and fitted. The spectral features are fitted with Voigt functions, where the Gaussian contribution of the peaks stems from the instrumental resolution (2.4 cm$^{-1}$).

Fitted Raman spectra of 2D Si layers prepared at three different deposition temperatures are shown in Fig. 4.15. At 220°C the spectrum of a dominant (3×3)/(4×4) silicene layer shows all the modes of epitaxial silicene as well as a small contribution from a-Si (orange curve). The Raman spectra after Si deposition at 250°C referred to a "mixed phase" are composed of six Raman bands. At a deposition temperature of 280°C a single "$(2\sqrt{3}\times2\sqrt{3})$" structure is observed. The spectrum of the sample prepared at 250°C exhibits the same Raman bands as those of epitaxial silicene (Fig. 4.15, bottom) plus two additional Raman modes at 155 and 520 cm$^{-1}$. The latter is consistent with the position of the L(T)O phonon mode of Si crystallites clearly visualized in AFM at higher deposition temperature (300°C). The presence of the ID mode in the Raman spectrum of the "mixed phase" suggests the co-formation of the "$(2\sqrt{3}\times2\sqrt{3})$" structure. The Raman spectrum of the "mixed phase" confirms the superposition of the 2D Si structures and Si crystallites.
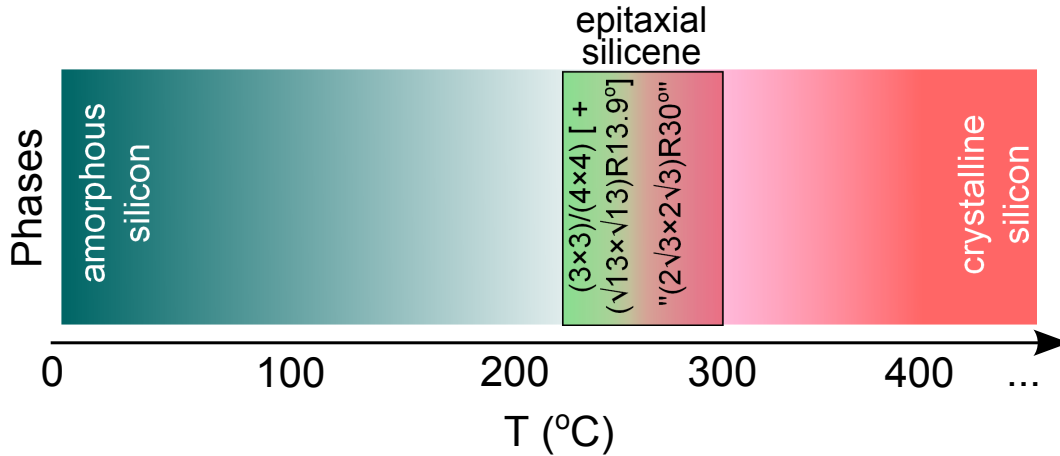
Figure 4.16: Reduced phase diagram of Si structures, which can be grown on the Ag(111) surface at various deposition temperatures.

## Phase diagram of Si deposition on Ag(111)

Based on the STM, LEED, and Raman results described above, a generic phase diagram for the formation of Si structures on the Ag(111) surface can be obtained (Fig. 4.16).

At low temperatures, *i.e.* from room temperature to ~150°C only amorphous Si is formed. In the temperature range between 200°C and 300°C 2D Si phases are formed, whereas at high temperatures above 300°C only 3D Si crystallites develop. In the narrow temperature window between 220°C and 280°C the metastable 2D Si phases are observed. Starting at 220°C a dominant (3×3)/(4×4) silicene phase is formed; it is characterized by two vibrational A modes at 175 and 216 cm$^{-1}$ and an E mode at 514 cm$^{-1}$. At higher temperatures an increasing mix of $(\sqrt{13}\times\sqrt{13})R13.9°$ domains and around 250°C also of the "$(2\sqrt{3}\times2\sqrt{3})$" structures are formed; all these ones show similar vibrational modes in the Raman spectra. Only the "$(2\sqrt{3}\times2\sqrt{3})$" structure shows the additional characteristic ID mode at 155 cm$^{-1}$ which stems from its inherent disorder. For preparation temperatures around 250°C the beginning of the co-development of diamond-like Si crystallites is observed; they further grow with increasing deposition temperatures. This scenario is in agreement with the LEED observations, which show that these different structures are simultaneously observed in this temperature range. For higher preparation temperatures, the contribution of the "$(2\sqrt{3}\times2\sqrt{3})R30°$" structure increases; it is mainly described by an appearance of the ID mode at 155 cm$^{-1}$. Correlatively, the features at 175 and 216 cm$^{-1}$, which are dominating in the spectrum of (3×3)/(4×4) silicene, decline gradually. This means that the evolution of

the Raman spectra for any multiple 2D phase regime can be simply explained by the weighted superposition of the Raman spectra of (3×3)/(4×4) silicene and of the "$(2\sqrt{3}\times2\sqrt{3})R30°$" structures.

Furthermore, the experimental results show that both 2D and 3D Si structures can coexist on the Ag (111) surface either due to their co-formation during the deposition or through a phase transition upon annealing of 2D Si phase [54]. For the understanding of a such complicated situation with the occurrence of several moieties on the same sample, Raman spectroscopy is demonstrated to be an indispensable tool to identify their different natures. It is especially true for the well-established signatures of amorphous or diamond-like Si. It is noteworthy that the incidence of the Raman band at 520 cm$^{-1}$ is a direct evidence of bulk Si crystallites, present on the Ag(111) surface, but not of a 2D layer as reported earlier [105, 119]. However, due to their possible co-existence, the occurrence of diamond-like Si crystallites does not exclude the presence of 2D Si layers on the Ag(111).

## 4.3  Summary

In this chapter, the Si deposition on Ag(111) was thoroughly investigated using *in situ* Raman spectroscopy, LEED, STM, and AFM techniques. It was shown that both 2D and 3D structures as well as their composites can be grown on the Ag(111) surface by varying the deposition temperature. The 2D Si layers, such as epitaxial $(3 \times 3)/(4 \times 4)$ silicene and the silicene-related "$(2\sqrt{3}\times2\sqrt{3})$" structure form in the temperature range from 220°C to 280°C. The intrinsic Raman spectral signature of epitaxial silicene on Ag(111) was identified. The properties, such as the phonon symmetries and their thermal coefficients, confirm the 2D nature of this first purely synthetic group IV elemental 2D material. Furthermore, it was shown that silicene is not just a Si-based copy of graphene, while its intrinsic buckling, modified by the silver (111) substrate, hosts interesting vibrational structure which differ to the flat case. The first-principles phonon calculations of $(3 \times 3)/(4 \times 4)$ silicene on Ag(111) system are in an excellent agreement with the experimental results. Furthermore, *in situ* Raman spectroscopy proves that the formation and the structural stability of the epitaxial silicene monolayer are limited. At 300°C a dewetting transition takes place and diamond-like Si nanocrystals are formed. The results confirm a close link between epitaxial (3×3)/(4×4) silicene and the silicene-related "$(2\sqrt{3}\times2\sqrt{3})R30°$" structure since both share similar spectral fingerprints. The ordered parts of the "$(2\sqrt{3}\times2\sqrt{3})R30°$" structure exhibit a

spectrum similar to that of the epitaxial (3×3)/(4×4) silicene, while the disordered parts yield a broad ID mode at 155 cm$^{-1}$. It was established that the Si deposition onto the Ag(111) surface in the range from 220 to 290°C usually results in the co-formation of 2D and 3D structures, whereas only moieties with $sp^3$ hybridized Si atoms are obtained outside this temperature range. According to these findings a phase diagram was generated reflecting the complicated interplay of the 2D and 3D moieties formation.

# *In situ* Raman spectroscopy of hydrogenated epitaxial silicene on Ag(111)

The identification of the Raman signatures of epitaxial silicene and silicene-related structures on Ag(111) provides a starting point for further studies of its functionalization by inorganic and organic compounds. Hydrogenation, introduced in the Chapter 2, is a first step towards the modification of epitaxial silicene, which might allow the functionalization and control of its characteristics. Here, Raman spectroscopy demonstrates a reliable way to not only identify hydrogenated silicene but also a method to test its stability and study the physical properties, such as vibrational and electronic structure. Primarily, the vibrational structure of hydrogenated silicene has to be revealed in order to serve for the investigation of other physical properties.

## 5.1   Hydrogenation of epitaxial $(3 \times 3)/(4 \times 4)$ silicene

In contrast to physisorbtion of epitaxial silicene on Ag(111), the hydrogen atoms are expected to chemisorb on the silicene layer [127–129]. This implies a covalent chemical bonding between the Si atoms and the H atoms. According to theoretical predictions [127, 130], H atoms would pull the Si atoms away from their positions in sublattices, which would increase the buckling of the silicene lattice by changing the hybridization state of the Si atoms to pure $sp^3$. Such significant structural modifications should be reflected in the corresponding

Raman spectra. In order to test this claim, a step-wise exposure of epitaxial $(3 \times 3)/(4 \times 4)$ silicene to atomic hydrogen was carried out. The evolution of the spectral profile during the hydrogenation is shown in Fig. 5.1(a).
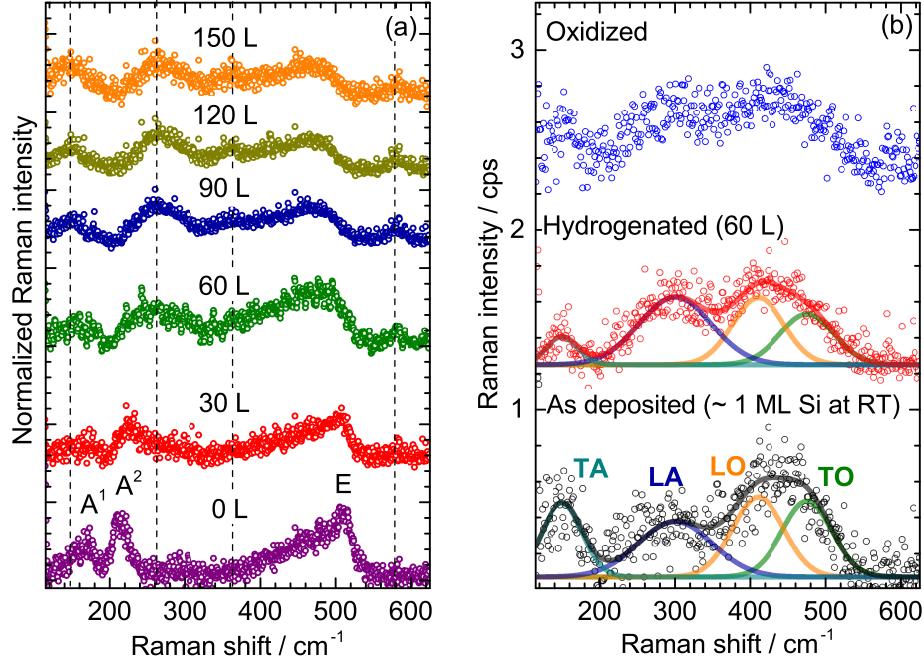


Figure 5.1: (a) Raman spectra of the epitaxial $(3 \times 3)/(4 \times 4)$ silicene recorded after the step-wise exposure to atomic hydrogen. The dashed vertical lines mark the positions of the new Raman bands as the result of hydrogenation. (b) Raman spectra of amorphous silicon before and after hydrogenation and subsequent oxidation. All spectra are stacked for clarity.

After Si deposition, a typical Raman spectrum of epitaxial silicene, which exhibits two A modes and one E mode, is obtained. The contribution of amorphous silicon (the low-energy shoulder of the E mode) is also detected. After the first hydrogenation step, a dose of 30 L, the Raman spectrum is altered in a peculiar manner: the $A^1$ mode vanished; the $A^2$ mode shifts towards higher energies, and the E mode shifts to lower energies. These trends can be solely attributed to the hydrogen adsorption on the silicene layer. Longer hydrogen exposure also reveals new bands emerging at doses of 60 L and 90 L at 147, 369, and 585 cm$^{-1}$. The Raman spectra recorded after even higher doses of 120 L and 150 L exhibit identical profiles, which suggests that the hydrogenation has reached the saturation. This is reasonable, since such an adsorption process is naturally self-limiting. According to the Raman results, the saturation dose should lie in the range of 90 - 120 L.

It is known that the sample prepared at 220°C also contains patches of amorphous silicon. Hence, the final spectrum also shows the Raman modes of a-Si, which might apparently alter due to the hydrogenation. In order to test this assumption, amorphous silicon clusters, grown on Ag(111) at room temperature, were hydrogenated using the same parameters as for the hydrogenation of $(3 \times 3)/(4 \times 4)$ silicene. The results are shown in Fig. 5.1(b). One can see that the Raman spectrum of hydrogenated a-Si clusters does change during H exposure. However, this concerns only relative intensities of the modes, but not their Raman shifts, as it is suggested by the fitting. Such modification of the Raman spectrum of a-Si upon hydrogenation has been reported previously [94]. Nevertheless, a-Si is rather stable against atomic hydrogen since it is less chemically reactive than silicene retaining no dangling bonds at the surface. Moreover, its surface protects the volume of the cluster for the hydrogen. Therefore even if hydrogen adsorbs at the surface, this does not disturb the cluster as a whole. The sample with hydrogenated a-Si was oxidized in order to test its chemical robustness. The Raman spectrum recorded after the oxidation is shown in Fig. 5.1(b) (top spectrum). It shows no significant difference to the one of hydrogenated a-Si, which suggests that neither hydrogen, nor oxygen chemically react with a-Si under given conditions. Thus, the Raman modes of amorphous Si can be excluded from the consideration.

Finally, the Raman spectrum of fully hydrogenated $(3 \times 3)/(4 \times 4)$ silicene shows distinct peaks at 147, 258, 369, and 585 cm$^{-1}$. However, some other peaks may be hidden under the broad background signal of a-Si. In order to enhance the Raman intensity of the silicene-related modes and reduce the signal of a-Si, epitaxial silicene was prepared at higher temperature (235°C), residing in a "dominant $(3 \times 3)/(4 \times 4)$ phase" (mainly $(3 \times 3)/(4 \times 4)$ structure and patches of the "$(2\sqrt{3} \times 2\sqrt{3})$" structure), shown in Fig. 5.2(a) (bottom spectrum). The corresponding LEED pattern is shown in Fig. 5.2(b). Both the LEED pattern and the Raman spectrum of the sample consistently confirm that a dominant $(4 \times 4)$ phase is formed. The picture of the hydrogenation of epitaxial silicene is also reproduced for the mixed phase samples. For low hydrogen exposure (25 L) a decrease of the relative intensities of the $A^1$ (175 cm$^{-1}$) and the E (514 cm$^{-1}$) Raman modes is observed. The $A^2$ mode, on the other hand, seemingly shifts towards higher energies by 4 cm$^{-1}$ and broadens. The latter can be explained by the mode asymmetry which is apparently related to the background, provided by the modes of hydrogenated amorphous silicon. The A modes are ascribed to an out-of-plane atomic motion of the Si atoms in the 2D lattice of epitaxial silicene. They are distinguished by their phase and by the contribution of the oppositely buckled Si atoms.
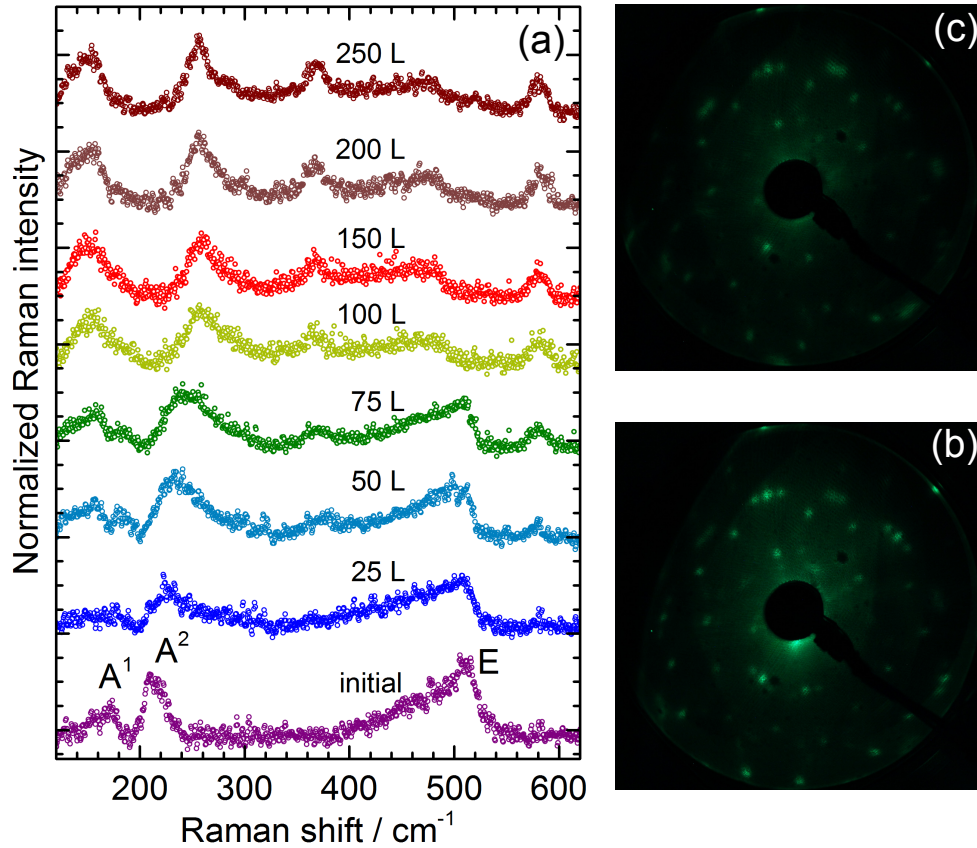
Figure 5.2: (a) Raman spectra of the dominant $(3 \times 3)/(4 \times 4)$ phase recorded after the step-wise exposure to the atomic hydrogen with a step of 25 Langmuir. The spectra are stacked for clarity. (b) LEED pattern of the dominant $(4 \times 4)$ phase as deposited and (c) after the H exposure with a dose of 250 L.

Namely, the $A^1$ mode is consistent with the in-phase motion of Si atoms and the larger eigenvectors of the down-buckled Si atoms, while the $A^2$ mode represents an out-of-phase atomic motion and a larger contribution from the up-buckled Si atoms (Fig. 5.3).
Assuming that the H atoms bind to the up-buckled Si atoms, one can explain the trends using the simple harmonic oscillator approximation. First, the mass of hydrogen is postulated to be negligible in comparison to the mass of the Si atoms. Therefore, it has to be assumed that the changes in the vibrational energy of A modes are related to the altered interaction between the Si atoms expressed in the change of the bond force constants. Hence, the stiffening of the out-of-phase $A^2$ mode testifies the presence of the additional restoring force, which acts upon the up-buckled Si atoms. The vanishing $A^1$ mode suggests that the H atoms conceal the $A^1$ type of motion and apparently forbid such vibration.
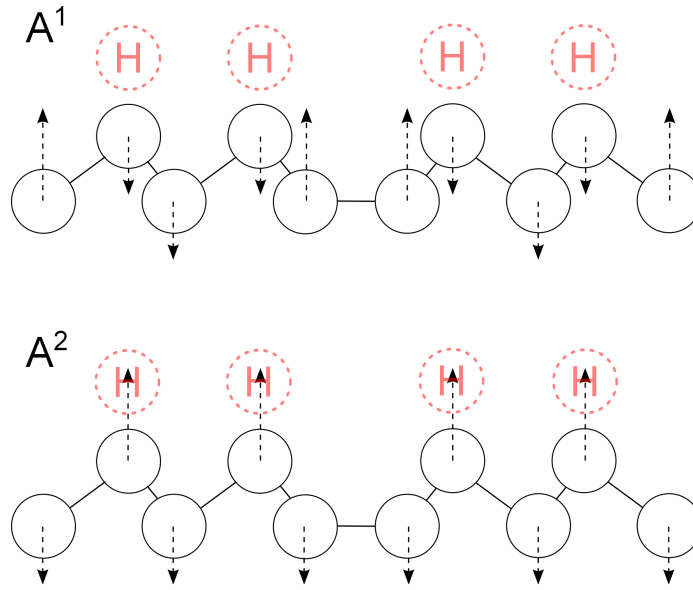
Figure 5.3: Schematic representation of the $A^1$ and $A^2$ vibrational modes, characteristic for $(3 \times 3)/(4 \times 4)$ silicene. The schemes show the unit cell and the H atoms in the side view.

The ID mode observed in the Raman spectrum, stems from the patches of the "$(2\sqrt{3} \times 2\sqrt{3})$" structure co-formed on Ag(111). The Raman spectrum, recorded after 50 L dose, exhibits the emergent band at 150 cm$^{-1}$, which can be related to the ID mode of the "$(2\sqrt{3} \times 2\sqrt{3})$" structure. Such association is corroborated by the large linewidth of 43 cm$^{-1}$, which manifests a short phonon lifetime and thus its relation to the disorder. This is possible due to the phonon scattering at the defects of the "$(2\sqrt{3} \times 2\sqrt{3})$" structure. According to the previous chapter, the Raman spectrum of the "mixed phase" also shows the small fraction of crystalline Si, which co-forms together with 2D Si layers. Since the preparation temperature was low, only small quantities of Si nanocrystallites were produced, therefore their incidence on the surface is non-uniform. This implies that there are areas on the sample, which are absolutely free of bulk-like Si. Otherwise, the Raman spectrum of the mixed phase might also contain the L(T)O phonon mode directly at 520 cm$^{-1}$. Such Raman band was observed to remain after the complete hydrogenation of the "mixed phase".

As the hydrogenation progresses, the $A^2$ Raman mode continues to shift in the direction of higher energies, reaching a position of 258 cm$^{-1}$ at the hydrogenation dose of 100 L. Judging from its lineshape, it apparently consists of several contributions. Nevertheless, it is assumed that the resulting Raman band at 258 cm$^{-1}$ originates from the former $A^2$ Raman mode. Such assumption is true if the symmetries of these modes are similar.

At the same time, the relative intensity of the E mode gradually decreases as well as its energy. At a H exposure of 100 L, no distinct E mode is detected. Lastly, the new Raman band at 585 cm$^{-1}$ is already present in the spectra from the lowest H dose and increases with an increasing H exposure. Such trend shows that this mode can serve as reliable marker of hydrogenation of epitaxial $(3 \times 3)/(4 \times 4)$ silicene.

## Raman signature of hydrogenated epitaxial $(3 \times 3)/(4 \times 4)$ silicene

As seen from the Raman spectra in Fig. 5.2(a), the hydrogenation saturates at an exposure of 100 L since the Raman spectra do not show any further changes. During the hydrogenation, the periodicity of the silicene lattice does not change at all, which can be seen from the LEED pattern, obtained after an H exposure of 250 L (Fig. 5.2(c)). The pattern contains the diffractions spots of the $(3 \times 3)/(4 \times 4)$ silicene, as well as the satellite phases. All spots, however, have lower intensity and slightly blurred when compared to the LEED pattern of the pristine silicene layer (Fig. 5.2(b)). This may be related to an increase of lattice defects, which may originate from possible local etching by the H atoms. Such etching of silicene was also observed in STM images, demonstrated in Ref. [131].

Evidently, all spectral bands of hydrogenated silicene have a rather broad linewidth (ca. 20 cm$^{-1}$). This is either an intrinsic property of the material, or a sign for defects in the layer. The latter is also possible due to the etching by hydrogen, which can lead to the complete amorphization of layers. Such outcome, however, can be ruled out by the presence of the diffraction spots of silicene, which appear in the LEED image. In order to answer this question as well as to understand the nature of the Raman modes, polarization-dependent Raman measurements were carried out. The scattering configurations are identical to the ones, introduced in the previous chapter.

The Raman spectrum of hydrogenated epitaxial silicene recorded in parallel configuration exhibits the bands at 147, 160, 258, 369, 480, and 585 cm$^{-1}$, while the spectrum, recorded in crossed configuration, shows only bands at 160, 480, and 585 cm$^{-1}$. Such behaviour can be explained in terms of selection rules defined by the Raman tensor for each mode. It turns out that the Raman tensors of the modes visible only in parallel geometry (at 147, 258, and 369 cm$^{-1}$) have only non-zero diagonal elements. Hence, these Raman bands are of the A-type symmetry. The Raman mode at 585 cm$^{-1}$, on the other hand, is present in both geometries and thus should be ascribed to the band of the E-type symmetry, characteristic for degenerate Raman bands. Hereinafter, it will be denoted as "E‴". The broad Raman bands at 160 and
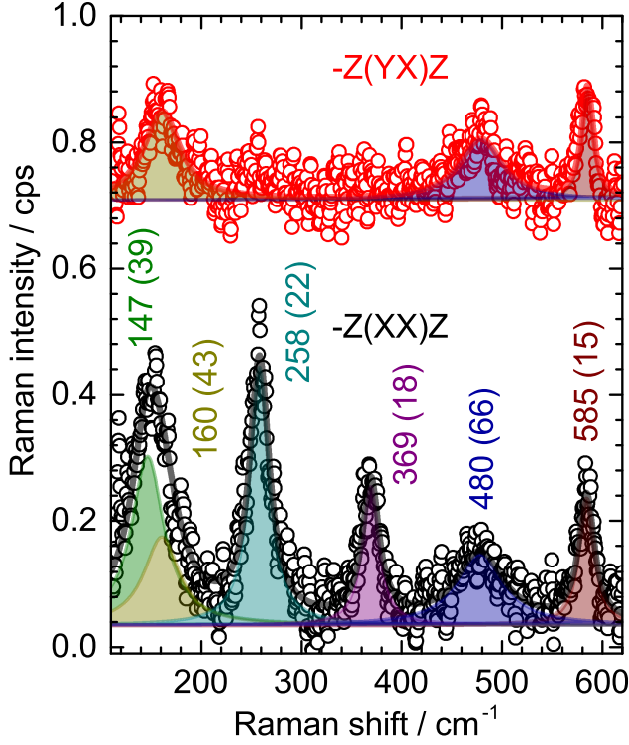
Figure 5.4: Raman spectra of the hydrogenated epitaxial $(3 \times 3)/(4 \times 4)$ silicene recorded in parallel (*-z(xx)z*) and crossed (*-z(yx)z*) configurations. The Raman spectrum of hydrogenated a-Si was subtracted. The bands are marked by position and FWHM. The spectra are stacked for clarity.

480 cm$^{-1}$ are also present in both spectra. Hence it would be natural to relate them to the E symmetry as well, however, their characteristics, such as a linewidth might suggest their relation to non-crystalline species. While the origin of the band at 160 cm$^{-1}$ remains unclear, the origin of the one at 480 cm$^{-1}$ could be related either to second order of the band at 258 cm$^{-1}$ or the former E mode (514 cm$^{-1}$). It is indispensable to understand the evolution of the Raman spectra of epitaxial silicene upon hydrogenation in order to comprehend its structural changes. In this respect, a former $A^2$ (216 cm$^{-1}$) mode evolves into the band at 258 cm$^{-1}$ (according to the symmetry considerations) and the former E mode might soften to the one at 480 cm$^{-1}$ while the lattice is presumably relaxed upon the hydrogenation. Generally, the presence of A and E modes in the Raman spectrum of hydrogenated epitaxial silicene validates its two-dimensional character. Hence it is safe to conclude that the hydrogenation does not induce a phase transition of the system to a bulk-like phase. According to the selection rules determined and STM measurements reported earlier [131], we suggest a trigonal symmetry group for the hydrogenated silicene. We consider the $C_3$ group, which is the most general one among all trigonal symmetry groups. The Raman tensors of this group are following:

$$A(z) = \begin{pmatrix} a & 0 & 0 \\ 0 & a & 0 \\ 0 & 0 & b \end{pmatrix}; \ ^1E = \begin{pmatrix} c & d & e \\ d & -c & f \\ e & f & 0 \end{pmatrix}; \ ^2E = \begin{pmatrix} d & -c & -f \\ -c & -d & e \\ -f & e & 0 \end{pmatrix}$$

While the attribution of the A symmetry to the Raman bands at 147, 258, and 369 cm$^{-1}$ is clear, the exact Raman tensor, corresponding to the E′ mode at 585 cm$^{-1}$, is unknown. To clarify the uncertainty, the Raman study in other scattering geometries should be performed. The origin of this E mode, however, can be related to the new type of vibration, which, for example, can be found in related systems, such as polysilanes. Additionally to other Raman bands of polysilanes, a Si-H bending mode is reported at 643.8 cm$^{-1}$ [132] and Si-H rocking band at 630 cm$^{-1}$ [133], which are close to the position of E′ mode. Such frequencies are emerging only in the presence of hydrogen atoms. They were not only observed in molecular systems, but also for hydrogen-doped bulk Si [134, 135]. However, the difference in energy between the above-mentioned vibrations and the E′ mode is significant, which implies that hydrogenated epitaxial silicene is a new Si system. It is important to note that neither the Si-H stretching modes around 2100 cm$^{-1}$ [135], nor other modes above 585 cm$^{-1}$ were observed in the spectra. The absence of the former is related to the insensitivity of the scattering geometry to such vibrations.

Despite that the underlying mechanism of the epitaxial silicene formation has not been fully understood yet, we can use the ratio of the Raman bands of different symmetries in order to determine the level of hydrogenation.
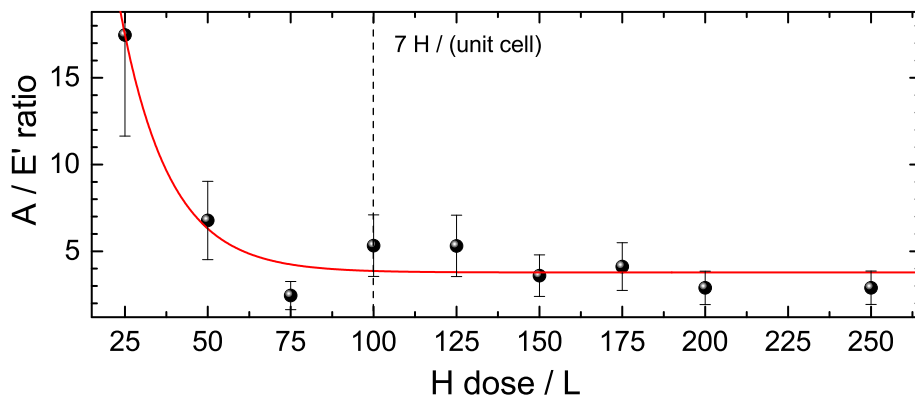


Figure 5.5: The ratio between A mode at 261 cm$^{-1}$ and E′ mode at 585 cm$^{-1}$ as a function of exposure of the atomic hydrogen to the epitaxial silicene.
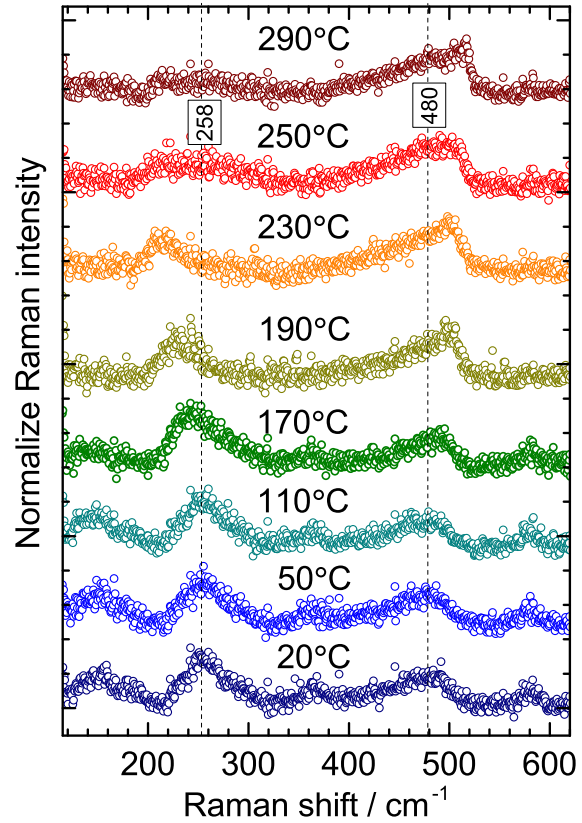
Figure 5.6: Series of normalized Raman spectra of the hydrogenated silicene, measured at increasing temperature. The vertical dashed lines mark the initial positions of the Raman bands of hydrogenated silicene.

Fig. 5.5 shows the ratio of the A mode at 258 cm$^{-1}$ to the E mode at 585 cm$^{-1}$ as a function of the exposure of epitaxial silicene to atomic hydrogen. The red curve is a fit of the ratio dependence on the dose of hydrogen. This dependence has an exponential behaviour and, therefore, corresponds to the classical chemisorption process. Since the monomolecular adsorption is a self-limiting process, we expect a particular hydrogen dose at which saturation is reached. Here, a dose of 100 (± 5) L is found to be the saturation point. Therefore, the hydrogenation level by using the A-to-E′ ratio can be determined. The ratio could also, in principle, reflect the average number of Si atoms per unit cell. To confirm such assumption, the exact mechanism of hydrogenation should be unravelled first.

## Dehydrogenation of $(3 \times 3)/(4 \times 4)$ silicene

Although the structure of epitaxial silicene is modified upon hydrogenation, it can be shown that such changes are reversible if the sample is heated to a certain temperature.
Figure 5.6(a) shows the Raman spectra of hydrogenated silicene at increasing temperatures. The Raman bands related to the hydrogenated system remain visible up to approximately

170°C. Their intensities mostly decrease. The thermal behaviour of the bands, however, is not the identical. The A-type mode at 258 cm$^{-1}$ and the broad band around 480 cm$^{-1}$ have the opposite trends of the shift upon heating (Fig. 5.7). At the next heating steps (190°C and
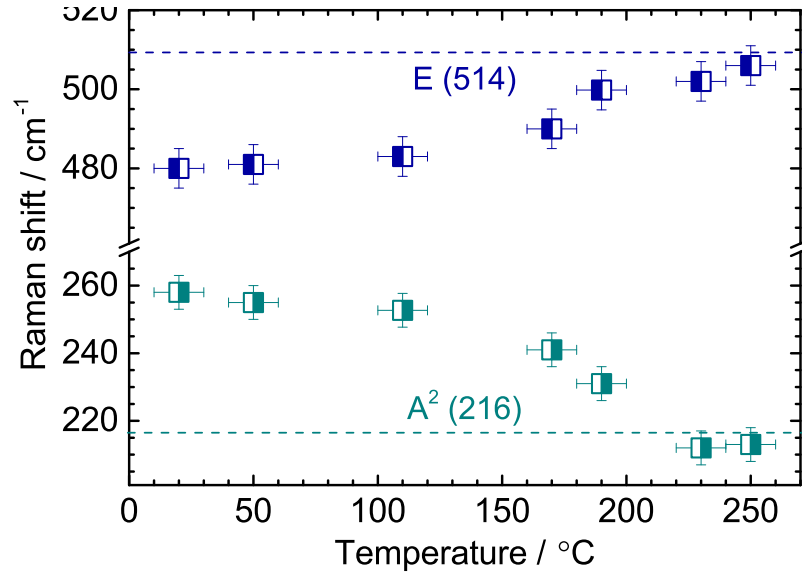


Figure 5.7: The Raman shift of the bands at 258 and 480 cm$^{-1}$ as a function of temperature.

230°C), these features dominate the Raman spectrum, which acquires the lineprofile similar to the one of epitaxial silicene. For a temperature of 250 °C, the position of E mode is at around 506 cm$^{-1}$, in excellent agreement with the temperature shift observed for pristine $(3 \times 3)/(4 \times 4)$ silicene in the previous chapter. At the same time, the other Raman bands of hydrogenated epitaxial silicene (147, 369, and 585 cm$^{-1}$) entirely disappear . The resulting Raman spectrum is the one of pristine epitaxial silicene. The only mode, which is absent after heating is the A$^1$ mode (175 cm$^{-1}$). This can indicate that epitaxial silicene has lower crystalline quality after the dehydrogenation which is supported by the previous results [131]. If the temperature increases further, the Si atoms are expected to dewet from the silver surface and form the Si crystallites. Otherwise, the hydrogenation can be repeated after the sample cooling to room temperature. It is remarkable that the E mode of epitaxial silicene recovers after the desorption of the hydrogen atoms justifying its relation to the E mode of epitaxial silicene. As for the latter, such softening of the E mode upon hydrogenation can also suggest the reduction of the charge density in the silicene lattice. Such interpretation stems from the predictions of the $sp^2$-to-$sp^3$ hybridization transition of Si atoms. Indeed, hydrogen is expected to increase the buckling of the silicene lattice, pulling the Si atoms

away from the lattice plane. In this case, the $sp^2$-to-$sp^3$ ratio of the "mixed hybridization" decreases, because of the increase of the $sp^3$ component. Such trend is observed in DFT calculations of free-standing silicene, where the buckling of 0.44 Å in pristine case is almost doubled to 0.72 Å in hydrogenated silicene [30]. Another important observation is the temperature of the dehydrogenation process. According to the experiment, the temperature is found to be ±230°C and is equal to the energy of 43 meV. Such energy would be insufficient to break a normal Si-H bond, which usually has a bonding energy around 3.16 eV [30]. While the temperature of dehydrogenation suggests that the hydrogen atoms are physisorbed on the silicene surface, the Raman results are evident for a chemisorption. Here, two important factors could play a role. Firstly, the supporting silver substrate could reduce the dissociation energy for hydrogen atoms due to the strong hybridization [49]. According to DFT simulations of hydrogenated epitaxial silicene, such energy is found to be 2.5 eV [136]. This energy is smaller than 3.16 eV but it is still large in comparison to the experimental value. On the other hand, silver surfaces are well-known for their catalytic capabilities, therefore, the dehydrogenation could occur in a catalytic manner, which implies the reduction of the disassociation barrier, but not the bond energy. Moreover, it was simulated for free-standing silicene that the lattice vacancy-type of defects can substantially reduce the energy barrier from 2.23 eV (pristine silicene) to 0.71 eV [137]. Such low energy can allow the smooth hydrogenation/dehydrogenation at elevated temperatures.

## Chemical stability of hydrogenated $(3 \times 3)/(4 \times 4)$ silicene

In order to test the chemical stability of hydrogenated epitaxial silicene against ambient atmosphere, Raman spectra were recorded after the oxidation of the material. Fig. 5.8 shows the Raman spectra of the pristine and hydrogenated epitaxial silicene before and after oxidation in the loadlock of UHV chamber via venting it by air-$N_2$ mixture for 30 minutes. Due to the fact that all Raman features, assigned to hydrogenated silicene, vanish upon the oxidation and only the broad features of the amorphous silicon remain in the spectrum after the oxidation, a simple conclusion can be drawn: the hydrogenated silicene is not air-stable similarly to its pristine form. Such outcome can be explained by the low dissociation energy of H-Si bonds in hydrogenated silicene. Despite the premises to use the hydrogen passivation in order to protect silicene from oxidation, it is clear that the H atoms cannot fully fulfil this need. It is well-known that the H-passivated Si surfaces are also not fully air-stable. On the other hand, the hydrogenation of free-standing silicene is predicted to increase the stability

of its lattice [127]. Moreover, it creates an energy barrier of 0.27 eV for the O atoms to adsorb on the surface of hydrogenated free-standing silicene [138], which will also hinder the oxygen migration but not the association with the bridge sites. Overall, the protection of epitaxial silicene in ambient atmosphere remains a challenge. At the same time, protected silicene may not retain the property of reversible hydrogenation/dehydrogenation, which could be utilized for hydrogen storage.

## Electronic structure of hydrogenated $(3 \times 3)/(4 \times 4)$ silicene

Along with the vibrational structure of hydrogenated epitaxial silicene, its electronic structure can also be probed by Raman spectroscopy by varying the excitation energy of the incident light. When the excitation energy is close to a real electronic transition, the electrons are promoted to the conduction band, enhancing the Raman cross section. This increases the probability of the scattering events adding up to the intensity of the Raman bands. In the case of epitaxial silicene, Raman scattering is always resonant one due to the inherent metallic character [48]. Silicane, however, is predicted to be a direct semiconductor [30]. Moreover, the size of the band gap is dependent on the level of hydrogenation, *i.e.* a number of the H atoms bonded to the silicene lattice [129]. Double-side hydrogenated free-standing silicene can exhibit a band gap of about 3 eV [139]. In order to examine such possibility,
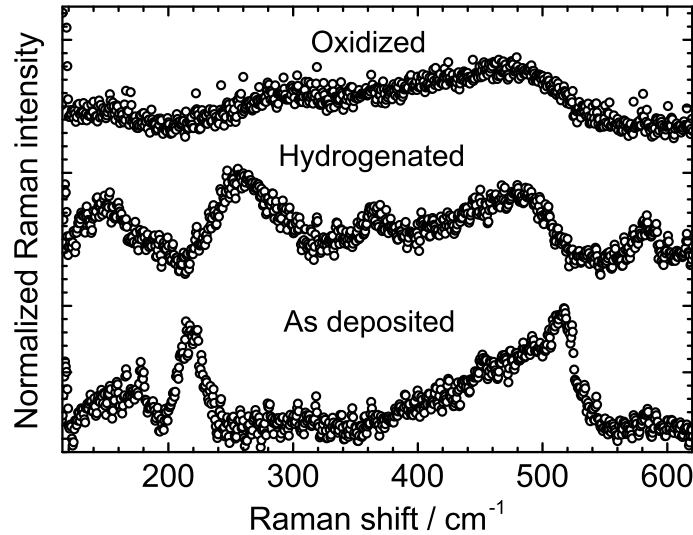


Figure 5.8: Normalized Raman spectra of epitaxial silicene, recorded after deposition, hydrogenation, and consequent oxidation.

the excitation-dependent Raman measurements of the epitaxial silicene after hydrogenation were performed with the excitation energies close to the predicted values. The results are shown in Fig. 5.9(a).
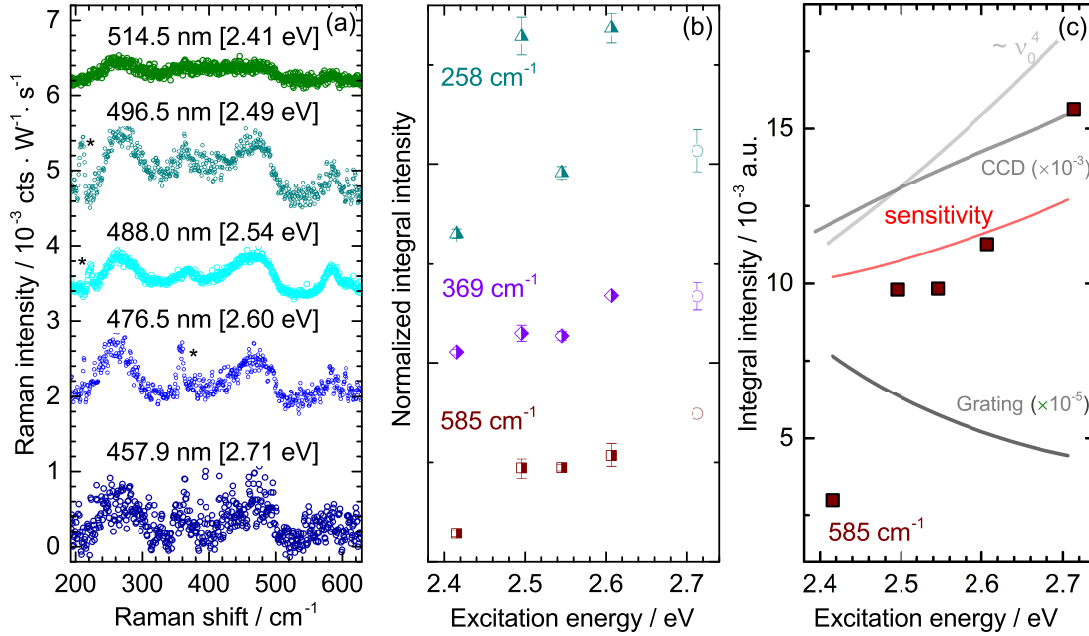


Figure 5.9: (a) Excitation energy dependent Raman spectra of hydrogenated epitaxial silicene in the range from 2.41 to 2.71 eV. The plasma lines of Ar laser are marked with asterisks. (b) Excitation profiles (integral intensity) of the distinct Raman modes of hydrogenated epitaxial silicene obtained from the fitting of the Raman spectra. The profiles are weighted by the laser power and recording parameters (normalized) and stacked. The points at 2.71 eV are left blank due to ubiquitous result of the fitting. (c) The contribution of the intensity factors plotted together with the integral intensity of exemplary Raman mode at 585 cm$^{-1}$. Units are chosen as arbitrary in order to simplify the comparison between contributions to the intensity of the Raman mode.

The Raman spectra were normalized by the integration time and the power of a particular laser lines in order to extract the actual Raman intensity. The signal-to-noise ratio differs for each spectrum due to the variation of the laser power of the different excitation wavelengths. Nevertheless, one can see that the Raman spectra are reproducible. Moreover, the positions of the Raman modes do not disperse with on the excitation energy. Such non-dispersivity of the Raman bands underlines the crystalline quality of hydrogenated silicene. In order to evaluate the dependence of the Raman mode intensity on the excitation energy, the integral area of each mode was extracted. Noteworthy, the Raman bands which do not

belong to hydrogenated silicene but amorphous silicon are left out from the consideration. When working with excitation profile, the great care should be taken in order to extract the actual Raman signal from the spectra, in which the instrumental sensitivity is unavoidably included. According to the consideration in the Chapter 3, the intensity of the Raman mode is factorized by the sensitivity of the spectrometer, $\nu^4$ dependence of the Raman scattering cross section ($\nu$ is the frequency of the excitation light), laser power density. The product sensitivity is shown in Fig. 5.9(c) (red curve). The trend qualitatively differs from the excitation profile of the E′ mode. This sensitivity curve was subtracted from all excitation profiles, which are shown in Fig. 5.9(b). The ascending Raman intensity towards higher excitation energies hints on the presence of the allowed optical transitions. Ideally, the excitation profiles should outline the electronic spectra. However, the direct comparison for epitaxial silicene is not possible, since any spectra, which contain the information about its electronic structure, have been not measured yet.

Although DFT simulations clearly show the non-zero electronic band gap, the presence of the supporting Ag substrate does not allow to directly compare our results with these predictions. However, the semimetal-to-semiconductor transition of epitaxial silicene upon hydrogenation can be expected also in the epitaxial system. Such assumption is corroborated by the excitation profiles. At the same time, the electronic structure of hydrogenated epitaxial $(3 \times 3)/(4 \times 4)$ silicene has been neither simulated, nor investigated yet by other methods. The closest system to the experimental case simulated is the so-called half-hydrogenated silicene (in which hydrogen binds only at one side of the silicene lattice), which exhibits either a band gap of 1.79 eV [130], or high density of states at Fermi level (no band gap) [129]. The difference in values originates from the different DFT methods used. In any case, the possible low-energy electronic transitions are out of reach for the range of the available excitation energies, therefore, the resonance behaviour observed should describe the high-energy electronic transition lying much above the opened band gap. In order to confirm that band gap opening for hydrogenated epitaxial silicene, excitation-dependent Raman measurement for the pristine $(3 \times 3)/(4 \times 4)$ silicene were also carried out (Fig. 5.10(a)).

The Raman spectra of epitaxial silicene exhibit two A and one E modes. The contribution of a-Si is subtracted. The normalization procedure is identical to that of hydrogenated silicene. The excitation profiles are depicted in Fig. 5.10(b). In contrast to hydrogenated silicene, they exhibit no dependence on the excitation energy. This is not surprising for a semimetallic
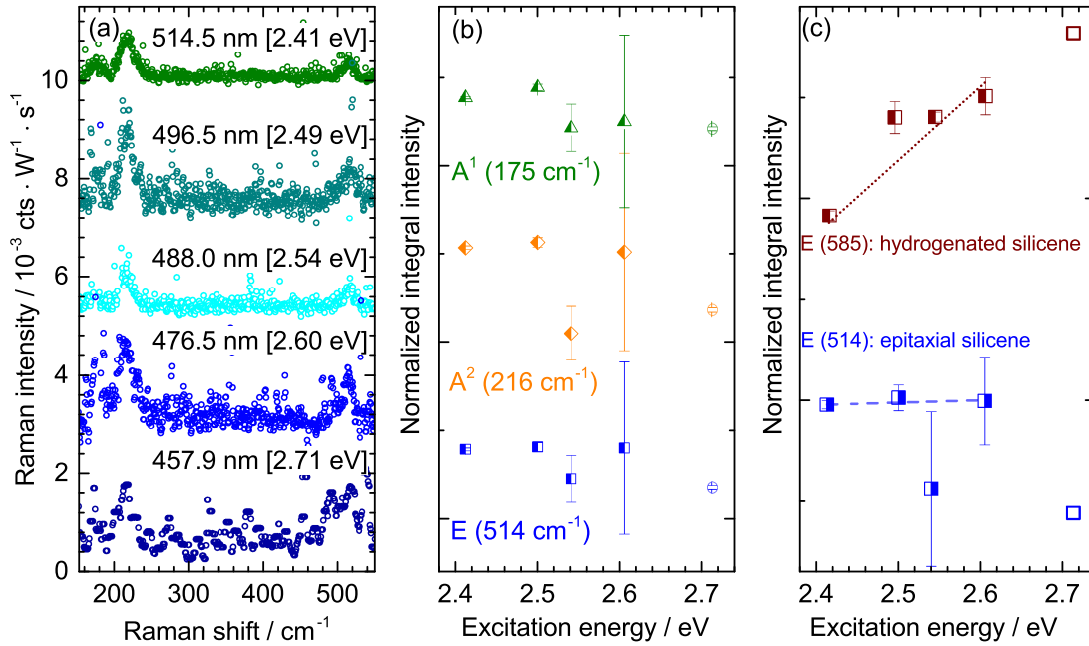
Figure 5.10: (a) Excitation energy dependent Raman spectra of epitaxial silicene in the range from 2.41 to 2.71 eV. The contribution of a-Si is subtracted. (b) Excitation profiles (integral intensity) of the distinct Raman modes of epitaxial silicene obtained from the fitting of the Raman spectra. The profiles are normalized and stacked. The points at 2.71 eV are left blank due to ubiquitous result of the fitting. (c) Excitation profiles (integral intensity) for the Raman modes of epitaxial 4×4 silicene (E mode, 514 cm$^{-1}$) and hydrogenated silicene (E mode, 585 cm$^{-1}$). The dashed lines are the actual fits. Open points are neglected for the fit.

material. To compare, the integral intensity of E and E′ modes are plotted as a function of the excitation energy (Fig. 5.10(c)). Both the experimental points and their linear fits suggest a difference between the excitation profiles. The last point (at 2.71 eV) is neglected in the fit due to the large error originating from the poor signal-to-noise ratio of the corresponding Raman spectrum. The semiconductor nature of hydrogenated silicene can only be surmised judging from the resonant dependence of its Raman modes. Due to narrow range of possible excitation energies, such excitation dependence is not considered to be conclusive.

A possible band gap opening can be also probed by photoluminescence (PL). A PL band is expected in the visible spectral region for free-standing silicene [127]. Such response was not observed for hydrogenated silicene in the range of 1.3 - 2.4 eV. The upper limit is set by the excitation wavelength, while the bottom limit is set by the low sensitivity of the spectrometer in near-IR region. In any case, this is reasonable to expect a PL band in this energy range.

The possible reasons of its absence need to be discussed. Firstly, the lack of PL band cannot imply a zero band gap. The band gap opening has been already demonstrated by ARPES results for the "$(2\sqrt{3}\times2\sqrt{3})$" structure [140]. The gap size around 1 eV was shown to be considerably lower than the calculated one, which, in the case of the optical spectroscopy in the visible range, would be unreachable. Also the interaction of hydrogenated silicene with a substrate has to be considered, which apparently altered after hydrogenation but does not vanish. Moreover, the metal substrate can be a good acceptor of the hot electrons, generated in hydrogenated silicene by the laser. Therefore, in order to understand the underlying reason of the absent photoluminescence, the substrate interaction must be thoroughly studied by DFT simulations and tested experimentally by using other, non-metallic, substrates.

## 5.2  Hydrogenation of the "$(2\sqrt{3}\times2\sqrt{3})$" structure

In the case of the hydrogenated epitaxial $(3\times3)/(4\times4)$ silicene, such functionalization turned out to exhibit interesting structural and electronic modifications, which also helped to resolve some of the questions concerning the pristine material. In this respect, the hydrogenation of the "$(2\sqrt{3}\times2\sqrt{3})$" structure is important to be investigated since hydrogenation of another 2D Si structure may occur differently. The Raman spectroscopy results are shown in Fig. 5.11. The spectrum of the pristine "$(2\sqrt{3}\times2\sqrt{3})$" structure exhibits all the Raman modes discussed above, *i.e.* the ones of the epitaxial silicene as well as the relatively intense ID mode at 155 cm$^{-1}$. Within the first hydrogenation steps, the trend is similar to the hydrogenation of the $(3 \times 3)/(4 \times 4)$ silicene. Namely, the $A^1$ mode vanishes and the $A^2$ mode shifts towards higher energy and becomes broader. At the same time, the ID mode shifts to the position of 143 cm$^{-1}$, retaining the broad linewidth of 40 cm$^{-1}$. The dominant band at 520 cm$^{-1}$ originates from the nanocrystalline bulk Si formed on the silver surface during the deposition. It expectedly remains unaltered upon the hydrogenation. The other Raman band at 585 cm$^{-1}$ appears in the Raman spectrum at a dose of 30 L. Its intensity is rather low due to the small amount of well-ordered, silicene-like, areas of the "$(2\sqrt{3}\times2\sqrt{3})$" structure [39]. At the saturation dose of 100 L, the spectral features of the "$(2\sqrt{3}\times2\sqrt{3})$" sheets appear as broad bands at 143 and 250 cm$^{-1}$ as well as low-intense modes at 369 and 585 cm$^{-1}$. The corresponding LEED pattern (Fig. 5.12, inset) shows that the diffraction spots of the "$(2\sqrt{3}\times2\sqrt{3})$" structure has not been altered. This implies that the ordered areas retain the translation $(2\sqrt{3}\times2\sqrt{3})$ symmetry. However, the diffraction spots become blurred, in
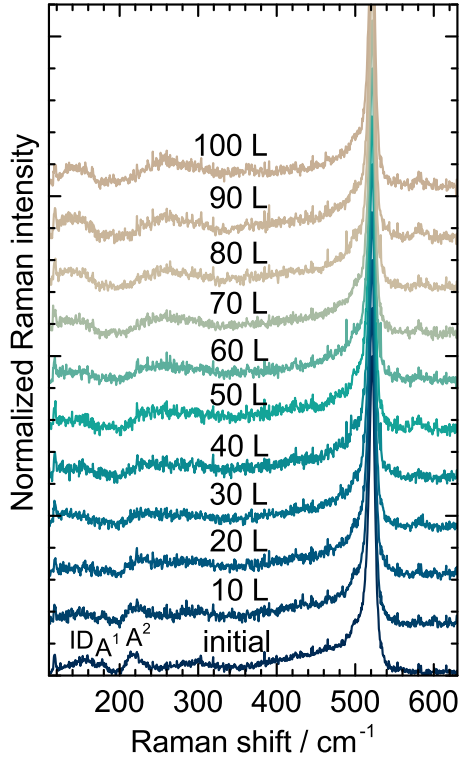
Figure 5.11: Normalized Raman spectra of the "$(2\sqrt{3}\times2\sqrt{3})$" structure upon the hydrogenation with a step of 10 L.

contrast to the sharp ones obtained from the unhydrogenated surface. It suggests the increase of the local disorder, induced by the hydrogen absorption. This disorder is explained by the "template effect". The starting structure is mostly disordered, therefore the hydrogenated layers also exhibit the irregular structure, expressed by very broad phonon modes and diffuse diffraction spots. This interpretation contradicts the STM results demonstrated for the hydrogenated "$(2\sqrt{3}\times2\sqrt{3})$" structure [140], which, however, are not conclusive due to the local character of the STM measurements. Indeed, the STM topography image shows the unordered areas as well as purely defected zones. Despite this, the presence of low-intense bands at 369 and 585 cm$^{-1}$ points out to the structural similarities between $(3\times3)/(4\times4)$ and "$(2\sqrt{3}\times2\sqrt{3})$" phases. This is in good agreement with the previous interpretation.

The Raman spectra of the hydrogenated structure of the three distinct growth regimes ($(3\times3)/(4\times4)$, "mixed phase", and the "$(2\sqrt{3}\times2\sqrt{3})$" structure) can be compared (Fig. 5.12). The resemblance of the Raman modes at 145, 258, 369, and 585 cm$^{-1}$ is clearly visible in all three cases. These bands can be considered as the true markers of hydrogenated epitaxial silicene on Ag(111). The other common feature is the broad background, which is related to already amorphous or amorphidized Si on the surface. Lastly, the presence of the Raman mode at 520 cm$^{-1}$ upon the hydrogenation is unchanged as the hydrogen
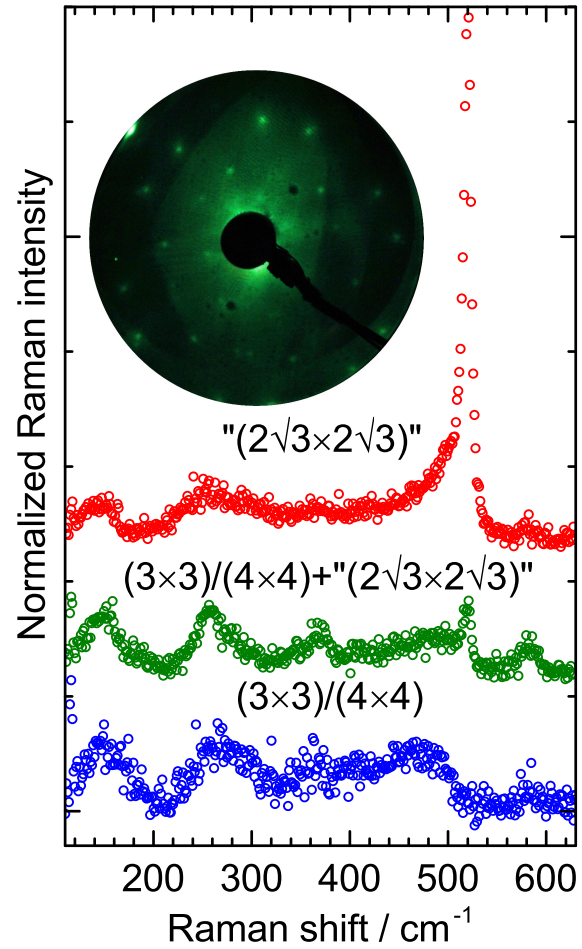
Figure 5.12: Normalized Raman spectra of the hydrogenated $(3 \times 3)/(4 \times 4)$ silicene, the "$(2\sqrt{3}\times2\sqrt{3})$" structure and the "mixed phase". Inset: the LEED pattern of the "$(2\sqrt{3}\times2\sqrt{3})$" structure after 100 L of atomic hydrogen exposure.

can passivate the surface of the crystallites but does not disrupt their inner structure. The intensity of this mode is in excellent agreement with the generic phase diagram presented in the previous chapter.

## 5.3 Summary

In summary, it was shown that *in situ* Raman spectroscopy can successfully probe the hydrogenation of the epitaxial silicene on Ag(111). It was found that the hydrogenation leads to a strong structural modification observed by a significant change in the spectral signature of hydrogenated silicene. The presence of sharp symmetric Raman modes suggests highly ordered Si:H structure, which was assigned to the $C_3$ symmetry group. In order to determine the degree of hydrogenation the ratio between Raman features with different symmetries was used in a qualitative manner. Despite the atomic rearrangement upon hydrogenation,

it is partly reversible, yielding the possibility of hydrogenation/dehydrogenation cycles at relatively low temperatures. The temperature of this transition indicates the possible presence of catalytic processes, which take place on the silver surface. Due to the reduced Si-H interaction, the protection of silicene layers via hydrogen passivation has no effect. The excitation-dependent Raman study showed the probable semimetal-semiconductor transition upon hydrogenation, however, more evidence is required. The hydrogenated "$(2\sqrt{3}{\times}2\sqrt{3})$" structure exhibits the spectrum that partly resembles the one of hydrogenated $(3 \times 3)/(4 \times 4)$ silicene, but also contains the signs of its amorphization. This shows the presence of the "template effect" when silicene-related structures on Ag(111) are exposed to hydrogen.

# *In situ* Raman spectroscopy of the multilayer Si structures on Ag(111)

The 2D Si structures at the monolayer coverage suffer from the substantial interaction with the supporting substrate. In order to weaken it, the interlayer can be introduced to play a role of the interface buffer. Epitaxial silicene is among the possible candidates due to the ease of its growth on Ag(111) and good lattice matching. The resulting system implies the formation of the stacked silicene layers. The Si surface with the $(\sqrt{3}\times\sqrt{3})$R30° periodicity was shown to form on epitaxial silicene/Ag(111) and interpreted as the multi-layer silicene due to the constant height of the terraces. Despite the clear appearance of this phase in STM images, the various experimental data and their interpretation are still discussed controversially. In order to unravel the nature of this structure, *in situ* Raman measurements of the $(\sqrt{3}\times\sqrt{3})$R30°Si/Ag(111) system were carried out.

## 6.1 *In situ* **Raman observation of the $(\sqrt{3}\times\sqrt{3})$R30° Si structure formation**

In order to grow "multi-layer silicene", Si deposition has to be prolonged beyond the 1 nominal ML coverage. Due to the inherent Stranski-Krastanov growth, the Si$(\sqrt{3}\times\sqrt{3})$R30°-Ag(111) structure forms the cascading islands [28]. Therefore, it is expected that the $(\sqrt{3}\times\sqrt{3})$R30° structure is to be found at any coverage above 1 ML. It was experimentally determined that a closed "second layer" can be obtained after 10 nominal ML Si deposition [81]. Interestingly, the multi-layer coverages feature only one surface of $(\sqrt{3}\times\sqrt{3})$R30°
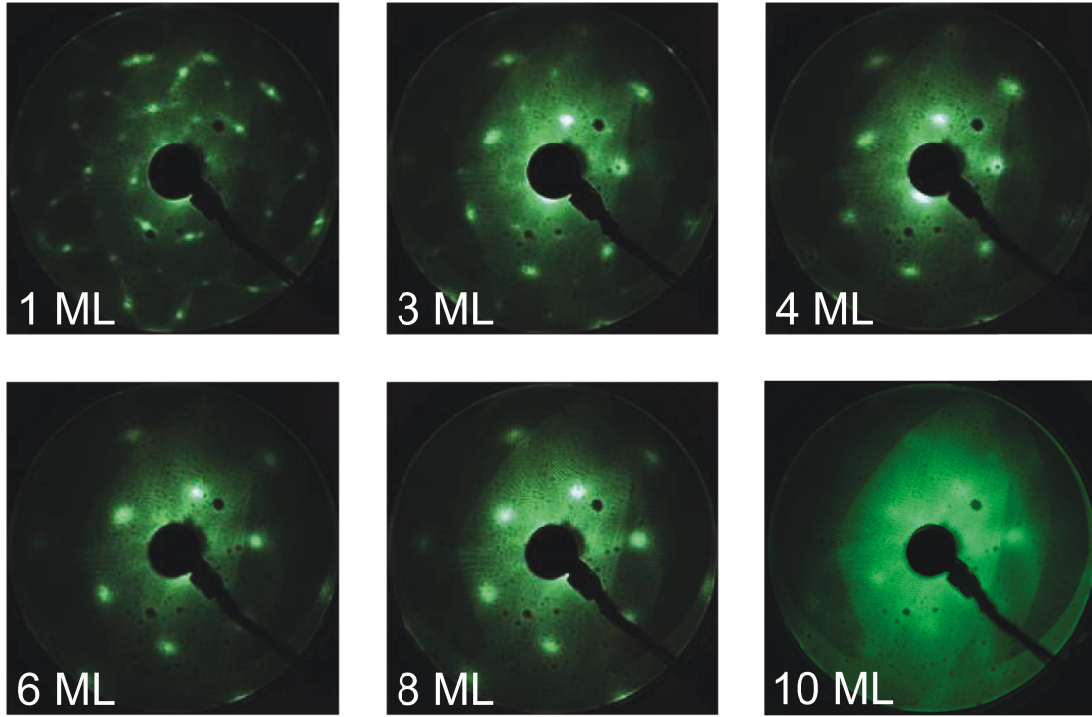
Figure 6.1: LEED patterns of the samples recorded after the Si deposition of the nominal MLs. $E_{el}$ = 32 eV.

symmetry, in contrast to the monolayer regime comprising $(3 \times 3)/(4 \times 4)$ and "$(2\sqrt{3} \times 2\sqrt{3})$" structures. Such situation greatly simplifies the identification of its Raman signature. The LEED patterns of step-wise growth of Si/Ag(111) are shown in Fig. 6.1. The LEED pattern of 1 ML Si deposition shows the diffraction spots of the dominant $(3 \times 3)/(4 \times 4)$ phase, explained in the Chapter 4. At a coverage of 3 nominal ML, the diffraction spots, which are related to the $(\sqrt{3} \times \sqrt{3})$R30° Si structure appear while the ones of $(3 \times 3)/(4 \times 4)$ silicene gently vanish. The intensity of the former suggest a significant amount of the corresponding islands formed. Nevertheless, the presence of the $(4 \times 4)$-related spots is clearly interpreted showing that the first $(\sqrt{3} \times \sqrt{3})$R30° Si layer is not closed yet. Within each next deposition step the size of the $(\sqrt{3} \times \sqrt{3})$-related diffraction spots seemingly increases, while their intensity remains unchanged. The reason of such constant intensity can be assumed as if the amount of this structure does not change with higher Si deposition. This would be possible if the $(\sqrt{3} \times \sqrt{3})$R30° Si structure retains only at the surface. The blurring of the diffraction spots is a sign of a partial disorder. The island type of growth of $(\sqrt{3} \times \sqrt{3})$R30° Si structure is clear, when looking at the LEED pattern, obtained after 10 ML deposition. The weak spots of first $(3 \times 3)/(4 \times 4)$ silicene layer are still present, while the ones of
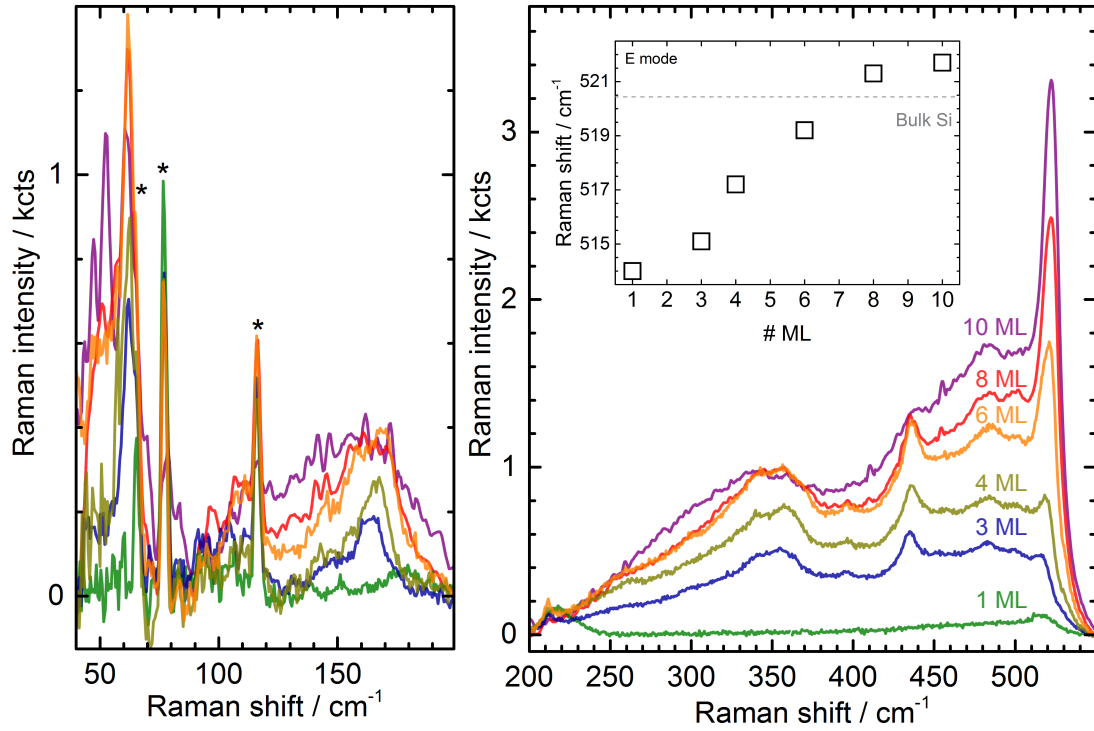
Figure 6.2: Raman spectra of the samples recorded within the Si deposition at step of the nominal MLs. Left panel shows the spectral region from 40 cm$^{-1}$ to 200 cm$^{-1}$. Laser plasma lines are marked with asterisks. Right panel shows the spectral region from 200 cm$^{-1}$ to 550 cm$^{-1}$. Inset: the position of the spectral band around 520 cm$^{-1}$ as a function of nominal MLs.

(√3×√3)R30° Si layers look similarly to the previous step of 8 ML deposition. This shows that the sensitivity of LEED drops for such complicated multi-layer cases since almost all information comes from the sample surface.

The *in situ* Raman measurements were performed after each deposition step (Fig. 6.2). The Raman spectrum of the 1 ML coverage fully reproduces the signature of epitaxial $(3 \times 3)/(4 \times 4)$ silicene. At the next step (3 nominal MLs), the spectrum is entirely altered, which is certainly related to the appearance of the (√3×√3)R30° structure on the surface. The intensity of some Raman bands and the overall background increases after each next deposition step. The most intense Raman bands at 62 cm$^{-1}$ and the one around 515 cm$^{-1}$ gradually rise. At the same time, the Raman bands around 160, 350, 430, and 480 cm$^{-1}$ has relatively constant intensity fixed above the increasing broad background features. Such unclear behaviour does not allow all Raman bands to be attributed to the formation of the "multi-layer" structure. Lastly, the Raman spectrum at a coverage of 10 ML shows only weak

distinct peaks, except the ones which resemble the signatures of the bulk-like species, namely, a-Si and c-Si, which were thoroughly explained in the previous chapters. The former is manifested by the pronounced background, while the latter can be recognized by the intense Raman mode at 520 cm$^{-1}$. The corresponding LEED pattern of 10 ML deposition shows that the ($\sqrt{3}\times\sqrt{3}$)R30° Si structure is weakly present on the surface, which is in agreement with the Raman results. The relative intensity of other peaks is greatly reduced, which can be explained considering that they are related to the surface only. In order to find the pure signature of the ($\sqrt{3}\times\sqrt{3}$)R30° Si structure and to exclude the ones of the bulk-like Si, their manifestation in the spectra should be subtracted. For this, they will be discussed first. According to the Raman results explained in the Chapter 4, the growth of 2D Si structures on Ag(111) is usually accompanied by the formation of Si structure with only $sp^3$ hybridized Si. Such situation is even more favourable at higher coverages, since the influence of the substrate is reduced within each next Si layer. Therefore, their formation is mainly governed by the interaction between the Si atoms. If the energy of the Si atoms is not enough to form a crystalline lattice, they will likely form an amorphous phase. Indeed, its presence can already be observed by the Raman spectra of > 3 ML coverages. The signature of a-Si is a set of the broad spectral bands at 150, 310, 410, and 480 cm$^{-1}$. They can be surmised in the broad background of all spectra in Fig.6.2 except the one at 1 ML. At the same time, the crystalline Si is also possible to form, since the substrate temperature during Si deposition is rather close to that of Si atoms dewetting (encountered in the Chapter 4). That is why it is obvious to assign the band around 520 cm$^{-1}$ to the L(T)O phonon mode of bulk Si. It is thought peculiar that its position actually deviates from the usual 520 cm$^{-1}$. The evolution of the spectral band, to which the L(T)O phonon mode contributes is shown in the inset of Fig. 6.2. One can see that starting from the position of the E mode at 514 cm$^{-1}$, this band shifts towards higher energies up to 521.5 cm$^{-1}$ with increasing Si deposition. Judging from the energy position of the L(T)O mode, it can be assumed that the difference to the one of Si single crystal can be associated with the compressive strain experienced by the crystallites in the presence of the ($\sqrt{3}\times\sqrt{3}$)R30° Si islands. Another interpretation is based on the fact that its position can vary from 520 cm$^{-1}$ to 523 cm$^{-1}$ in the Raman spectra of the ($\sqrt{3}\times\sqrt{3}$)R30° Si structure, which could be a sign of the superposition of the spectral contributions: one contribution originates from the Si nanocrystallites, while the other is related to the ($\sqrt{3}\times\sqrt{3}$)R30° Si structure itself. However, in both cases, Raman spectroscopy confirms the presence of Si nanocrystallites on the surface. The analogous conclusions have
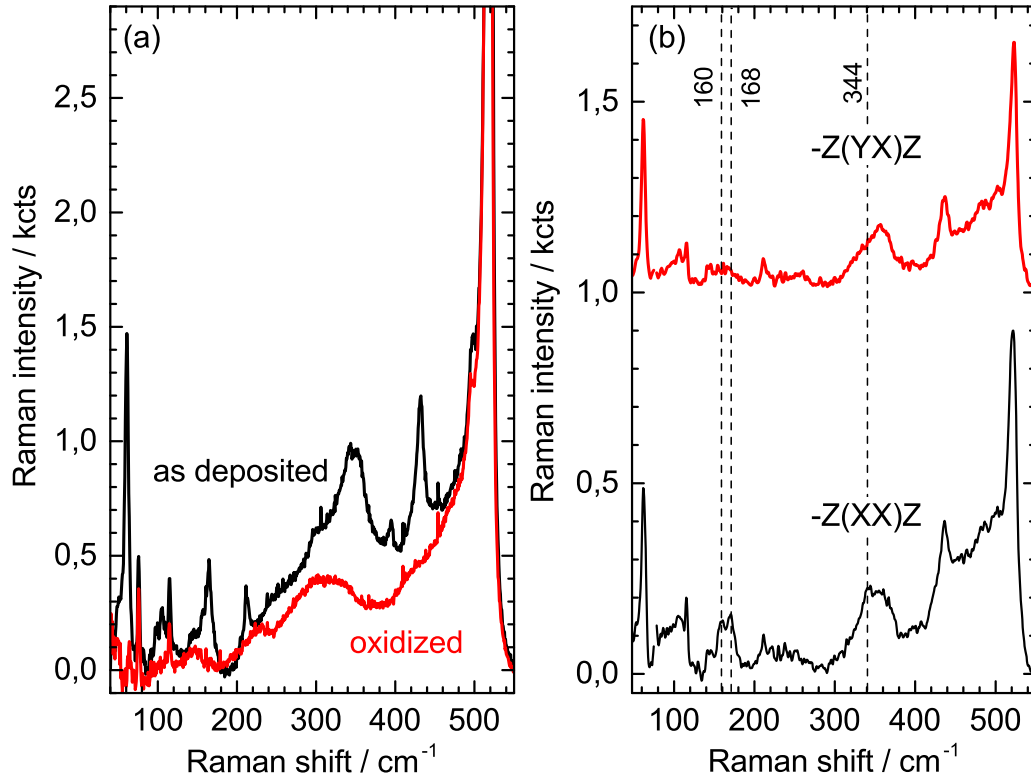
Figure 6.3: (a) Raman spectra of the sample with the 3 nominal ML of Si deposition before and after the oxidation. (b) Polarization-dependent Raman spectra recorded in parallel (-z(xx)z) and crossed (-z(yx)z) scattering configurations.

been already drawn from X-ray emission and absorption spectroscopy (XES and XAS) [79], IV-LEED [73, 75], and metastable atom electron spectroscopy (MAES) [76] measurements of similar samples. If the spectral contributions of a-Si and c-Si are excluded, the other Raman bands, which can be seen in the Raman spectra of the samples with 3-8 nominal MLs, are attributed to the $(\sqrt{3}\times\sqrt{3})$R30° Si structure.

In order to confirm the interpretation about the co-formation of 2D and 3D Si phases as well as to identify what Raman bands exactly belong to the $(\sqrt{3}\times\sqrt{3})$R30° Si structure, the oxidation of the samples was performed using a nitrogen-rich atmosphere, while venting the loadlock of the UHV chamber. The results are shown in Fig. 6.3(a). It is clearly seen that only the spectral contributions of a-Si and c-Si to the Raman spectrum remain after oxidation. First, this shows the assignment of the background and L(T)O phonon mode is absolutely correct. Secondly, such outcome greatly supports the assumption about a surface-like nature of the $(\sqrt{3}\times\sqrt{3})$R30° Si structure, which, being a surface, degrades

under ambient conditions due to the chemical interaction with oxygen, water and other molecular species. The oxidized 2D structure also exhibits broad bands around 230 cm$^{-1}$ and 300 cm$^{-1}$, which cannot be related to the familiar 3D Si species. These modes underline defective, non-crystalline, nature of the oxidate, when compared to an ordered ($\sqrt{3} \times \sqrt{3}$)R30° Si structure. The air-stability of "multi-layer silicene" was claimed by the study based on the *ex situ* Raman results, which supposedly showed that the structure is stable over a period of 24 hours [141]. It is obviously incorrect. Nevertheless, the wrong methodology of stability test was used later in Ref. [142], showing that the 2D layer can withstand the oxidation "up to 6 days". The reason for these erroneous interpretations lies in the incorrect mode assignment. Namely, it was mistakenly interpreted that the band around 520 cm$^{-1}$ belongs to the signature of multi-layer silicene. Hence, the oxidation of the samples prepared at higher Si coverages destroys the surface, but not the Si crystallites. They are only partially oxidized, predominantly on the surface and can be still detected in the Raman spectrum. This case shows how important to know the actual Raman spectrum of the material prior to the interpretation of its physical properties. In the case of 2D Si layers, this can be carried out using *in situ* Raman spectroscopy, which clearly showed that neither monolayer, nor "multi-layer" silicene are air-stable.

To determine the Raman selection rules for the modes of the ($\sqrt{3} \times \sqrt{3}$)R30° structure, polarization-dependent Raman spectra were recorded in parallel (*-z(xx)z*) and crossed (*-z(yx)z*) scattering configurations. Unlike monolayer epitaxial silicene, the multi-layer counterpart does not exhibit clear selection rules for its Raman bands. This may be related to the rotational distribution of the islands. Almost all Raman modes remain fully visible in crossed configuration. However, the bands located at 160, 168, and 344 cm$^{-1}$ are partially suppressed in the crossed geometry. These modes are polarized. The two low-energy modes are consistent with the previous results on epitaxial silicene, where the polarized modes found in this range were assigned to out-of-plane phonons. It is presumed that the Raman bands at 154 and 168 cm$^{-1}$ have a strong out-of-plane motion component similarly to other 2D Si layers. However, since the structural model is not yet confirmed, the exact symmetry group is unknown. However, it is safe to suggest that such structure has either 3- or 6-fold symmetry according to its appearance in LEED and STM [28]. Hence, the Raman-active phonons can have either an A, or an E symmetry. It implies that all other modes, which are not of A symmetry, can be either E modes or might originate from two-phonon Raman scattering. The exact symmetry assignment of the Raman modes related to the ($\sqrt{3} \times \sqrt{3}$)R30°
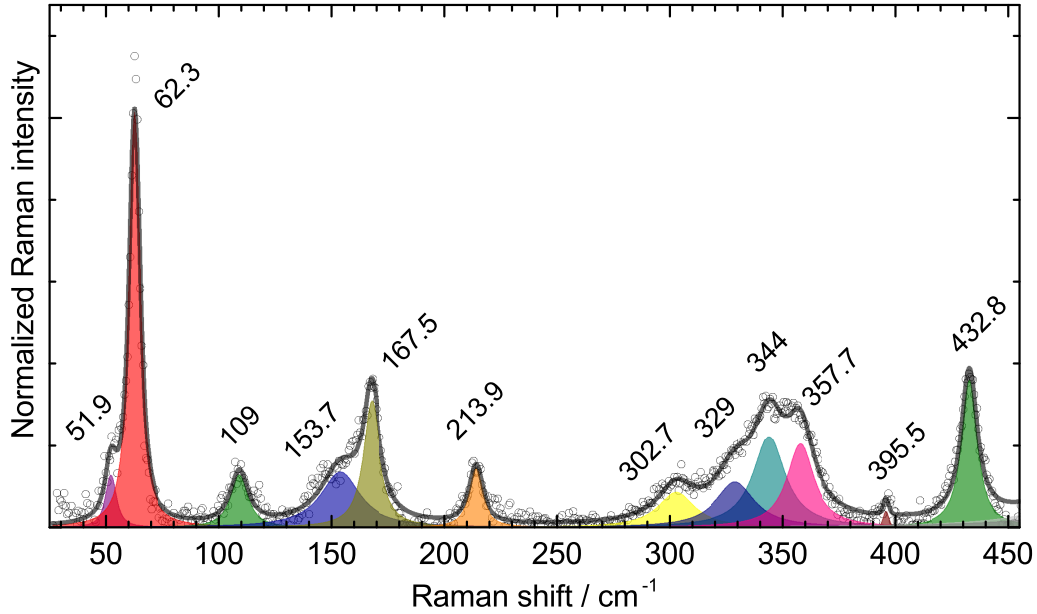
Figure 6.4: (a) Raman spectrum of the ($\sqrt{3}\times\sqrt{3}$)R30° structure obtained after the subtraction with the spectrum of the oxidized sample. It is shown together with the fitted components, marked by the spectral position.

structure will be possible when the exact structure is revealed and confirmed by *ab initio* methods aiming at the agreement of the vibrational properties.

## 6.2 Raman signature of the ($\sqrt{3}\times\sqrt{3}$)R30° Si on Ag(111)

The oxidation of the ($\sqrt{3}\times\sqrt{3}$)R30° Si structure not only shows that this structure is chemically unstable under ambient atmosphere which greatly contradicts previous reports [141, 142], but can also be used to separate its spectral signature from the co-existent species in the sample. This is done by the subtraction of the Raman spectrum of an oxidized sample from the one of the non-oxidized layer. The result of this procedure is shown in Fig. 6.4. The differential spectrum exhibits 12 Raman bands, which can entirely be attributed to the ($\sqrt{3}\times\sqrt{3}$)R30° Si structure. Their characteristics such as their frequencies and linewidths are listed in Table 6.1. In contrast to epitaxial $(3 \times 3)/(4 \times 4)$ silicene, the ($\sqrt{3}\times\sqrt{3}$)R30° Si structure exhibits more spectral bands, which suggests that its structure is more complicated as well as a possible interlayer coupling. In fact, it is indeed decoupled from the silver substrate electronically [81], however, it should still strongly interact with the underlying silicene layer. Among all Raman bands, which are assigned to this structure, two of them

99

Table 6.1: Raman modes of the $(\sqrt{3}\times\sqrt{3})$R30° structure on Ag(111)

| Raman shift, cm$^{-1}$ | 51.9 | 62.3 | 109.0 | 153.7 | 167.5 | 213.9 | 302.7 |
|---|---|---|---|---|---|---|---|
| FWHM, cm$^{-1}$ | 5.8 | 6.0 | 9.2 | 21.0 | 9.0 | 7.4 | 19.6 |
| Raman shift, cm$^{-1}$ | 328.9 | 343.9 | 357.7 | 395.5 | 432.8 | | |
| FWHM, cm$^{-1}$ | 20.7 | 17.0 | 14.5 | 2.9 | 8.4 | | |

have a very distinct appearance in the spectrum. These bands are found at 62.3 and 432.8 cm$^{-1}$. Their intensity is directly proportional to the amount of $(\sqrt{3}\times\sqrt{3})$R30° Si structure in the samples. The Raman spectra of this structure, measured *in situ* were reported earlier showing some of the Raman bands shown in the Table 6.1 [106, 142]. The direct comparison between two experiments would, however, be not correct due to the different experimental conditions, most importantly, the temperature. However, it can be assumed that the bands found in the range from 300 to 450 cm$^{-1}$ are similar to the Raman bands at 343.9, 357.7, 395.5, and 432.8 cm$^{-1}$. These bands were attributed to the defects on the edges of the 2D islands and suggested to support the buckled nature of silicene [106]. It is important to note that the authors consider the $(\sqrt{3}\times\sqrt{3})$R30° Si structure as a monolayer phase, while epitaxial $(3 \times 3)/(4 \times 4)$ silicene serves as a buffer layer.

The most intense Raman mode of the $(\sqrt{3}\times\sqrt{3})$R30° Si structure is found at 62.3 cm$^{-1}$. This frequency corresponds to the energy of 7.7 meV. Such low-energy phonon has to be associated with a massive collective mode rather than a mode of the separate atoms. Indeed, the mode with a similar energy is found for the Si(111)-(7×7) surface reconstruction, and assigned to an acoustic Rayleigh wave back-folded to the centre of the Brillouin zone [143]. The Rayleigh wave is a surface acoustic wave, which includes both transversal and longitudinal motion of several surface layers along the propagation direction [144]. Judging from the intensity of this mode, all islands of the $(\sqrt{3}\times\sqrt{3})$R30° symmetry must host such mode, contributing to the Raman spectrum. Another aspect is a backfolding effect itself, which is common for the surface reconstructions. If the acoustic phonon branches of the $(\sqrt{3}\times\sqrt{3})$R30° structure and Si(111)-(7×7) surface reconstruction appear at the same energy at $\Gamma$ after the backfolding, this can give a strong hint towards the similarity of these systems. The matching energy and other mode characteristics should imply the similarity of these systems, while the coincidence of the Rayleigh modes is a quite unique.

# 6.3   Raman signature of the ($\sqrt{3}\times\sqrt{3}$)R30°Ag on Si(111)

In order to test the assumption of the similarity of the "multi-layer silicene" and the Ag-reconstructed bulk Si surface, the Ag($\sqrt{3}\times\sqrt{3}$)R30°/Si(111) samples were prepared and investigated by *in situ* Raman spectroscopy. The ($\sqrt{3}\times\sqrt{3}$) surface reconstruction is well-known for metals to form on a Si(111) surfaces [77, 145]. The Si(111)-(7×7) reconstruction was prepared first and then 1 ML of Ag was deposited onto this surface. The corresponding Raman spectra are shown in Fig. 6.5(a,b). The spectra were measured in parallel and crossed scattering configurations before and after Ag/Si(111) was aged in low vacuum. Such surface deterioration is crucially important here, since the contribution of the bulk crystal in the Raman spectrum is much stronger than the one of its surface. Hence, the separation of the signal, originating from the surface structure, via subtraction of the spectrum of an aged surface is indispensable. In this respect it is important to note that the Raman intensity of the surface phonons is about three orders of magnitude lower than the one of the first-order phonon modes. On other hand, the Raman modes of the ($\sqrt{3}\times\sqrt{3}$)R30° Si structure on Ag(111) (also "Si/Ag(111)") are clearly visible in the Raman spectrum even without subtraction. Such high Raman intensity is obviously unusual for the surface phonons. The intensity of the Raman modes of ($\sqrt{3}\times\sqrt{3}$)R30° Si structure is much higher that the one of the Raman modes of $(3 \times 3)/(4 \times 4)$ silicene, which cannot be matched even if one considers the triple amount of Si on the surface. This can be related to the enhancement of Raman scattering of the ($\sqrt{3}\times\sqrt{3}$)R30° Si structure on Ag(111). Among the existing effects, the most probable candidates are the surface-enhanced Raman scattering (SERS) and the resonance Raman scattering (RRS). They will be discussed later in this chapter.

Indeed, the Raman bands of Ag/Si(111) in the spectra, obtained after the subtraction procedure, were hardly visible in the raw Raman spectra. The differential spectra for both scattering configurations are shown in Fig. 6.5(c). The band positions and linewidths of the modes are obtained from a fitting procedure and listed in Table 6.2. From comparison of the Raman modes of the ($\sqrt{3}\times\sqrt{3}$)Ag/Si(111) and ($\sqrt{3}\times\sqrt{3}$)Si/Ag(111), it is clear that their positions are predominantly matching: 10 out of 12 modes of Si/Ag(111) system can be found in the spectral signature of Ag/Si(111) system. At the same time, not all the Raman modes of the former system are visible in the Raman spectra of the ($\sqrt{3}\times\sqrt{3}$)R30° Si structure. Interestingly, the shared characteristic of these peaks is their large linewidth. From the fitting (Fig. 6.5(c)), it can be seen that these modes account
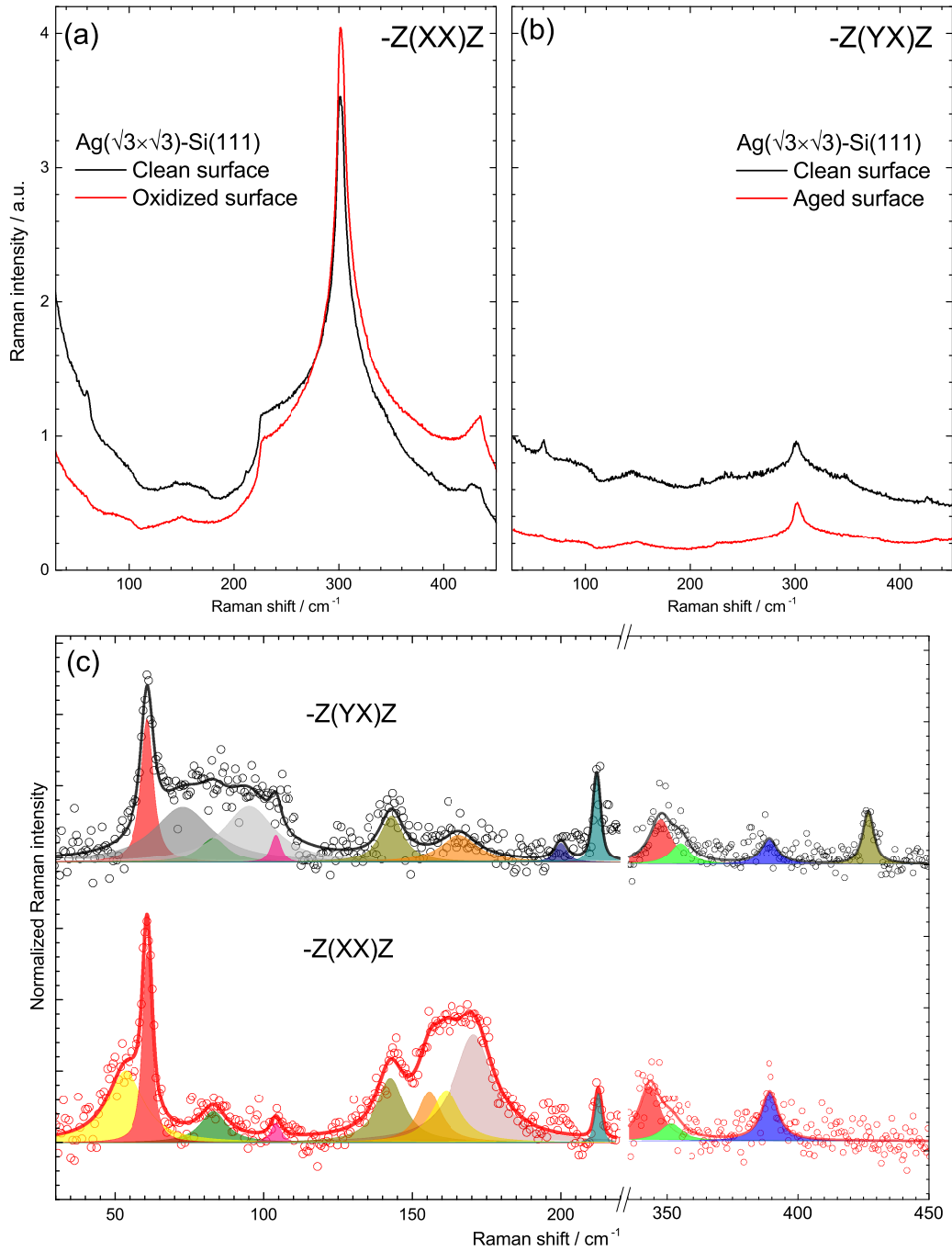
Figure 6.5: (a) Raman spectra of the Ag($\sqrt{3}\times\sqrt{3}$)-Si(111) sample before and after oxidation in parallel (-z(xx)z) configuration. (b) Raman spectra of the Ag($\sqrt{3}\times\sqrt{3}$)-Si(111) sample before and after oxidation in crossed (-z(yx)z) configuration. (c) Fitted intensity differences between the Ag($\sqrt{3}\times\sqrt{3}$)-Si(111) and the surface oxidized, obtained for both scattering configurations. The range from 220 cm$^{-1}$ to 320 cm$^{-1}$ is omitted due to the subtraction artefact of the 2TA phonon mode. The sample preparation and Raman measurements were performed by Dr. E. Speiser and Dr. P. Vogt.

Table 6.2: Polarization-dependent Raman modes of $(\sqrt{3}\times\sqrt{3})$Ag on Si(111)

| -z(xx)z configuration | | -z(yx)z configuration | | $(\sqrt{3}\times\sqrt{3})$Si/Ag(111) |
|---|---|---|---|---|
| $\omega$, cm$^{-1}$ | FWHM, cm$^{-1}$ | $\omega$, cm$^{-1}$ | FWHM, cm$^{-1}$ | $\omega$, cm$^{-1}$ |
| 51.3 | 11.6 | - | - | 51.9 |
| 60.7 | 4.3 | 60.8 | 5.1 | 62.3 |
| - | - | 72.7 | 24.0 | - |
| 83.6 | 11.6 | 83.0 | 11.4 | - |
| - | - | 95.0 | 21.0 | - |
| 104.4 | 3.6 | 104.0 | 4.0 | 109.0 |
| 143.3 | 10.0 | 143.1 | 9.5 | - |
| 159.2 | 16.0 | - | - | 153.7 |
| - | - | 165.7 | 15.3 | 167.5 |
| 171.1 | 13.5 | | | - |
| 199.5 | 4.9 | 200.0 | 4.9 | - |
| 212.5 | 2.7 | 212.0 | 3.3 | 213.9 |
| - | - | - | - | 302.7 |
| - | - | - | - | 328.9 |
| 343.4 | 9.3 | 347.5 | 10.1 | 343.9 |
| 351.5 | 10.4 | 355.0 | 9.5 | 357.7 |
| 389.2 | 7.7 | 389.0 | 7.6 | 395.5 |
| - | - | 426.8 | 5.1 | 432.8 |

for the broad spectral features, therefore their relation to the Ag($\sqrt{3}\times\sqrt{3}$)R30°/Si(111) is questionable. The only non-matching bands of Si/Ag(111) system are the ones at 303 and 329 cm$^{-1}$. Due to their authentic origin, they can be considered as the markers of the structural distinction of the $(\sqrt{3}\times\sqrt{3})$R30° Si structure. Otherwise, their appearance could also be an artefact of subtraction. In order to resolve this issue, the support of DFT simulations for the possible models should be carried out. At the moment, the results of the *in situ* Raman measurements clearly suggest the structural similarity of Si/Ag(111) and Ag/Si(111) systems. Additionally, taking into account that $(\sqrt{3}\times\sqrt{3})$ type of reconstruction is more favourable for Ag than Si atoms and that such reconstruction was never discovered for the silicon surfaces, we conclude that "multi-layer silicene" is actually a silver-terminated Si surface. Such conclusion concurs with the interpretations based on the results obtained by other techniques [73, 75, 76]. The claims of the wrong preparation conditions would concern the Si crystallites, which, indeed, form at higher temperatures, however, these samples also contain bulk-like Si, which forms underneath the $(\sqrt{3}\times\sqrt{3})$R30°Ag/Si quasi-2D structure [79, 80]. *In situ* Raman spectroscopy provide the way to separate different Si compounds from consideration.
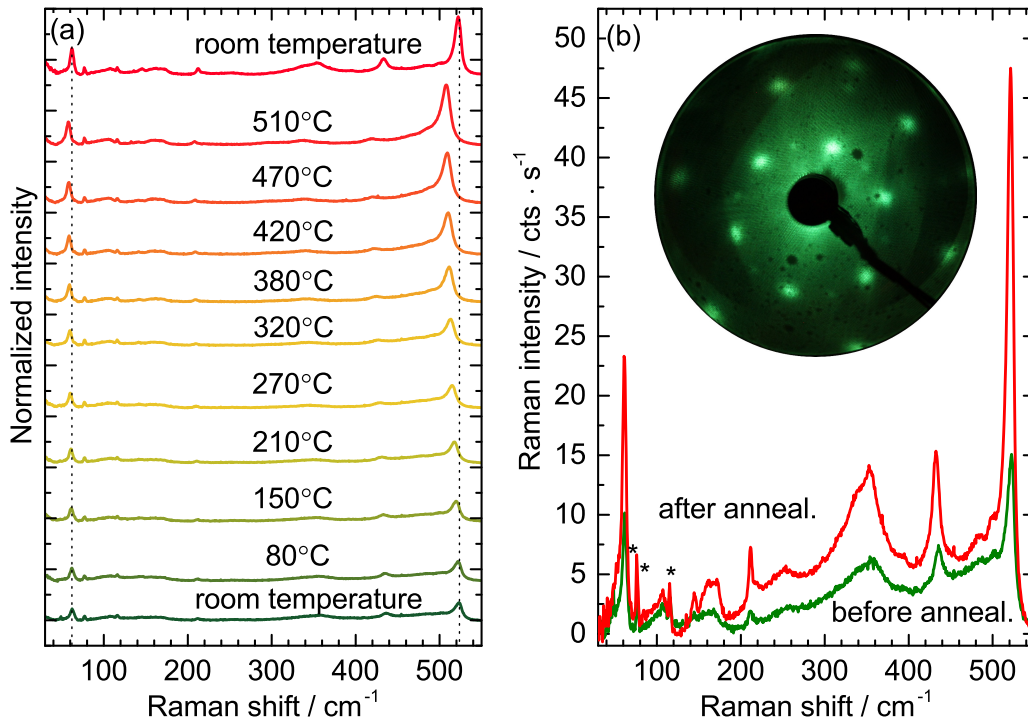
Figure 6.6: (a) Series of Raman spectra of the $(\sqrt{3}\times\sqrt{3})$R30° structure recorded at varying temperature up to 510°C. Top Raman spectrum was recorded at room temperature after the annealing. (b) The initial and final Raman spectra of the $(\sqrt{3}\times\sqrt{3})$R30° structure. Inset: the LEED pattern, which corresponds to the post-annealed sample. $E_{el}$ = 32 eV.

## 6.4 Physical and chemical properties of $(\sqrt{3}\times\sqrt{3})$R30° Si structure

In order to support the interpretation of the character of the $(\sqrt{3}\times\sqrt{3})$R30° Si structure as well as to study its physical and chemical properties, following experiments were carried out.

### Thermal properties of Si/Ag(111) system

The thermal stability of Si/Ag(111) was probed via the post-annealing experiment with the sample heated to 520°C. The results are shown in Fig. 6.6(a). The Raman spectra, recorded at higher temperatures remain seemingly unaltered during the sample heating. Two dominant Raman modes at 62 and 521 cm$^{-1}$ are clearly visible in all Raman spectra presented. They shift towards lower energies at higher temperatures following the anharmonicity-related temperature dependence of a Raman mode in semiconductor. The same trend is observed

for other modes, present in the spectra. At first glance it may not be clear that the 2D-to-3D phase transition takes place around 300°C. In order to illustrate it, the Raman spectra of the sample before and after annealing are plotted together (Fig. 6.6(b)). The Raman modes of the annealed sample have higher intensity and are significantly narrowed. It is a clear evidence that the post-annealing of the ($\sqrt{3}\times\sqrt{3}$)R30° Si/Ag(111) system leads to the increase of its amount, which originates from the formation of bigger islands of the same character. Moreover, the crystallinity of this structure is improved by high temperature. Moreover, the intensity of the mode at 521 cm$^{-1}$ is also increased. This is the main indication of the phase transition. Due to the fact that the Raman modes of the ($\sqrt{3}\times\sqrt{3}$)R30° Si structure are distinct after annealing, it can be safely concluded that this structure is thermally stable up to 520°C. It is also confirmed by the presence of corresponding diffraction spots in the LEED pattern of the ($\sqrt{3}\times\sqrt{3}$)R30° structure after annealing (Fig. 6.6). At the same time, the intensity of L(T)O phonon mode suggests increased amount of Si crystallites. This can be either a result of phase transition of first silicene layer or of the metal-mediated crystallization. Moreover, the position of the L(T)O mode changes to 520 cm$^{-1}$, while before annealing it was located at 523 cm$^{-1}$. Such discrepancy can be explained by the different origin of this mode before and after annealing.

In order to unravel the true origin of this band, its thermal behaviour is analysed. To add the reference, the analysis of another dominant Raman mode of the ($\sqrt{3}\times\sqrt{3}$)R30° Si structure was performed. The results are shown in the Fig. 6.7. Fig. 6.7(a,b) shows the detailed Raman spectra in the ranges around the bands at 62 cm$^{-1}$ and 523 cm$^{-1}$, respectively. The bands shift and broaden modes when the temperatures increases. Both effects are caused by the anharmonicity effects of the crystal. One can clearly see that instead of usual intensity drop upon heating, the Raman intensity of both modes gains proportionally. It is mainly related to the aforementioned increase in the overall amount of structure as well as improved crystallinity. Another observation is a sudden change of the rate of the shift for the mode at 523 cm$^{-1}$ (Fig. 6.7(b)). To illustrate this clearly, the mode position is plotted as a function of temperature (Fig. 6.7(d)). The mode position of the spectral band at 62 cm$^{-1}$ is plotted in a similar manner (Fig. 6.7(c)). The linear dependence of the mode shifting, which is observed in both cases, is expected in this range of elevated temperatures. The experimental points are coloured, showing the position of the modes before (black) and after (red) the phase transition, which takes place around 300°C [54, 102]. The colour-coded sets of the shifting were fitted with the linear equation: $\omega' = \omega_0 + \chi \cdot T$, where $\omega_0$ is the position of
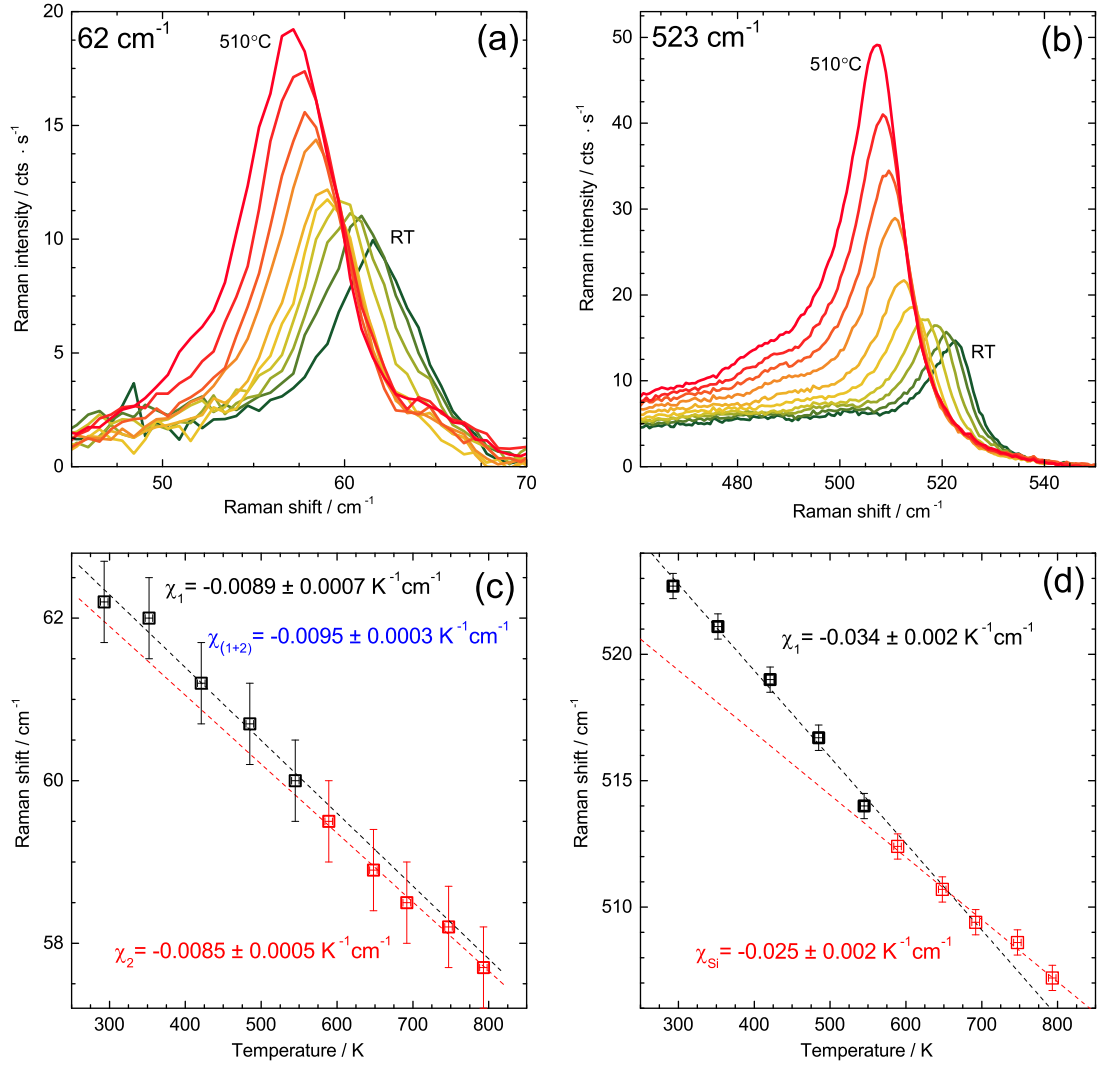
Figure 6.7: Detailed Raman spectra of the "multi-layer silicene" in the range around the bands at (a) 62 cm$^{-1}$ and (b) 523 cm$^{-1}$ recorded in a post-annealing experiment. Raman shift of the mode at bands at (c) 62 cm$^{-1}$ and (d) 523 cm$^{-1}$ as a function of temperature. The experimental points are shown as squares (black: before the phase transition, red: after the phase transition). The dashed lines are the actual fits of the coloured sets.

the Raman mode at 0 K, $\chi$ is thermal coefficient of the mode, and T is the temperature (in K). This fit provides the value of the thermal coefficient for a particular mode. The thermal coefficients of the mode at 62 cm$^{-1}$ before and after the phase transition are identical within the error range, which is also confirmed by the cumulative fit ($\chi_{(1+2)}$). On the other hand, the thermal coefficients of the mode at 523°C differ before and after the transition point. The thermal coefficient after the phase transition at 300°C conforms to the one of a bulk Si mode. Moreover, it is clear that extrapolation of the fit to room temperature demonstrates that its position is 520 cm$^{-1}$. The thermal coefficient below 300°C is closer to the values, inherent to the 2D objects, such as epitaxial silicene or silicon surface. Therefore, this fact is in favour of the relation of this Raman band to the $(\sqrt{3}\times\sqrt{3})R30°$ structure. Moreover, this mode was previously reported for the "multi-layer silicene" [141]. The different thermal coefficients of the Rayleigh wave and the E mode hint on the different origin of these oscillations: collective mode is less sensitive to the temperature change than the light-weight L(T)O phonon mode. Knowing the behaviour of the Raman modes upon heating, it is finally possible to draw parallels between the $(\sqrt{3}\times\sqrt{3})$ Si structure and the one formed after Si monolayer deposition annealing at high (> 300°C) temperatures as observed by Raman spectroscopy. One can notice that the Raman spectra shown in Fig. 4.3 and Fig. 4.8(d) exhibit the spectral signatures identical to the one of the $(\sqrt{3}\times\sqrt{3})R30°$ Si structure on Ag(111). Due to the high thermal stability of this system, it is no surprise that it can be encountered when Si deposited at high temperatures, or after the annealing of epitaxial $(3 \times 3)/(4 \times 4)$ silicene, along with the Si nanocrystallites. Therefore, it can be suggested that at the temperatures > 300°C the Ag atoms obtain the kinetic energy enough to dissociate from the surface of the silver crystal impinging on the Si layers. Such process was already mentioned in the Chapter 4 as the metal-mediated crystallization. It is, however, interesting that metal atoms form a highly symmetric structure on top of the Si atoms, while the rest of the Si atoms undergoes the transition to the Si(111)-type of surface, the two-atom layer of which, indeed, resembles the honeycomb lattice of free-standing silicene. Such bilayer model for the Ag-terminated Si island was also considered as a possible explanation of the $(\sqrt{3}\times\sqrt{3})R30°$ Si structure on Ag(111) [27, 70]. It does not include the silver toplayer, however, it might explain what is formed underneath it. The *in situ* Raman results also showed the non-negligible differences between the $(\sqrt{3}\times\sqrt{3})$Si/Ag(111) and the $(\sqrt{3}\times\sqrt{3})$Ag/Si(111) systems. Such dissimilarity must hold since the Si atoms, deposited onto the Ag(111) surface, cannot form the Si(111) single crystals. This is not possible due to the very low deposition temperature as well as

the low amount of the Si atoms, which is required to form bulk Si unit cells. Moreover, the Stranski-Krastanov type of growth of the $(\sqrt{3}\times\sqrt{3})$R30° structure shows its pseudo-layered character with a very well defined layer height of 0.31 nm [28], which is lower than the size of the bulk Si unit cell (0.54 nm). Although the presence of the silver atoms on top of the Si lattice is not a desired outcome, its controlled growth and thorough investigation can lead to the broad range of the applications, envisioned by the theoretical predictions [146–150].

## Ion bombardment of the Si/Ag(111) system

The following experiments can show that the system, in fact, belongs to the semiconductor surfaces/semiconductor-metal interfaces much more than to a 2D material. The Raman spectrum of a protypic 2D material, graphene, exhibit one peculiar spectral feature, the so-called "D band", assigned to the lattice motion, allowed in the presence of lattice defects [151]. Its Raman intensity is directly proportional to the number of point defects, which allows the quantitative analysis. It is noteworthy that such useful information is purely based on the unique structure and the symmetry of the 2D honeycomb material. The analogue of the D band of epitaxial silicene has not been discovered yet, possibly due to the low Raman signal of this mode. This is not the case for "multi-layer silicene" structure, where the Raman signal is highly intense to see the weak spectral features such as a defect-related mode. In order to induce such defects in the Si/Ag(111), the ion bombardment was used. Such experiments gave the reproducible method to quantify the defect density in a monolayer graphene estimated from the intensity of the D band [152]. Ion bombardment was performed in the loadlock chamber on the UHV vessel using $Ar^+$ ions accelerated by an ion gun with a kinetic energy of 1.5 keV at the partial pressure of $10^{-5}$ mbar. These parameters were adapted from the bombardment experiment, carried out for graphene, taking into account the structural differences between graphene and silicene. Each bombardment cycle took 10 seconds. The Raman measurements of the $(\sqrt{3}\times\sqrt{3})$R30° structure during the step-wise bombardment cycles are shown in Fig. 6.8. The spectra were normalized to the intensity of the L(T)O mode. Such normalization is reasonable since its intensity decreases much slower than those of the surface phonons.

The initial Raman spectrum of the sample shows the signature of the $(\sqrt{3}\times\sqrt{3})$R30° structure. The decrease of the mode intensity within the bombardment is evident implying the reduction of the structure volume probed. Thus, the ions which were supposed to create the point defects in the silicene lattice, destroy the structure instead. At the final step (after 15
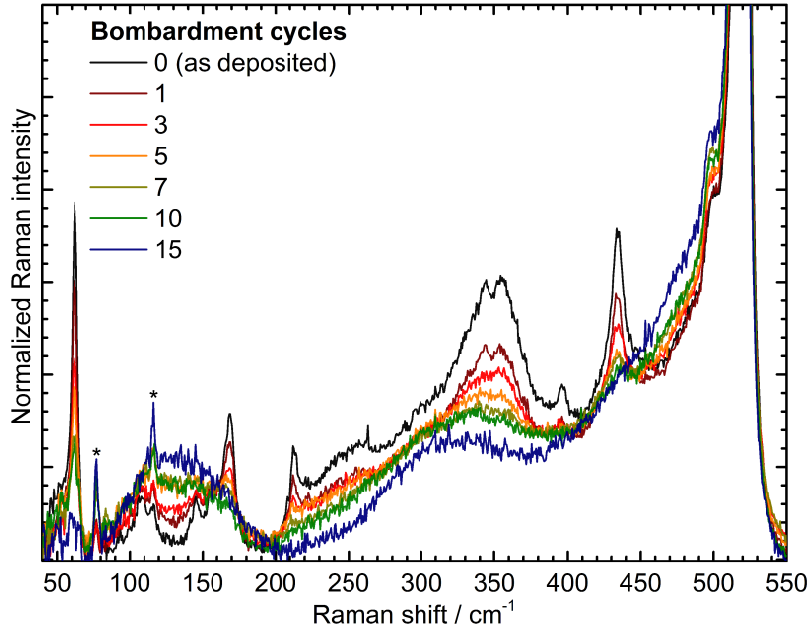
Figure 6.8: Normalized Raman spectra of the $(\sqrt{3}\times\sqrt{3})R30°$ structure before and after step-wise Ar$^+$ ion bombardment. Bombardment cycle implies the exposure of the sample to the beam of high-energetic (1.5 keV) Ar ions at the pressure of $10^{-5}$ mbar for 10 seconds.

bombardment cycles) the Raman spectrum of the sample resembles the one of the oxidized $(\sqrt{3}\times\sqrt{3})R30°$ multi-layer (Fig. 6.3(a)). It exhibits the spectral signatures of amorphous and crystalline silicon species. One can clearly see that the Raman band at 150 cm$^{-1}$ consistent with the TA phonon mode of a-Si distinctly grows within each next bombardment. Indeed, the energy of the Ar$^+$ ions as well as duration of the bombardment are not sufficient to clean off the Si nanocrystallites, which are more robust than the Si surface. Eventually, the defect-related modes, appearing in the Raman spectrum within bombardment, have no relation to the 2D Si layers, but the to 3D Si clusters.

## Excitation-dependent Raman measurement of the Si/Ag(111) system

The excitation-dependent Raman spectra of the $(\sqrt{3}\times\sqrt{3})R30°$ structure are shown in Fig. 6.9. It follows from the metallic character of "multi-layer silicene", demonstrated by ARPES [81] and XAS/XES experiments [79], that only a $I \sim (\nu_0)^4$ type of the dependence of the Raman intensity on the excitation energy is expected. However, neither intensity enhancement, nor any dispersivity of the modes of the $(\sqrt{3}\times\sqrt{3})R30°$ structure is observed in the Raman measurements. On the other hand, the Raman intensity enhancement for the L(T)O phonon
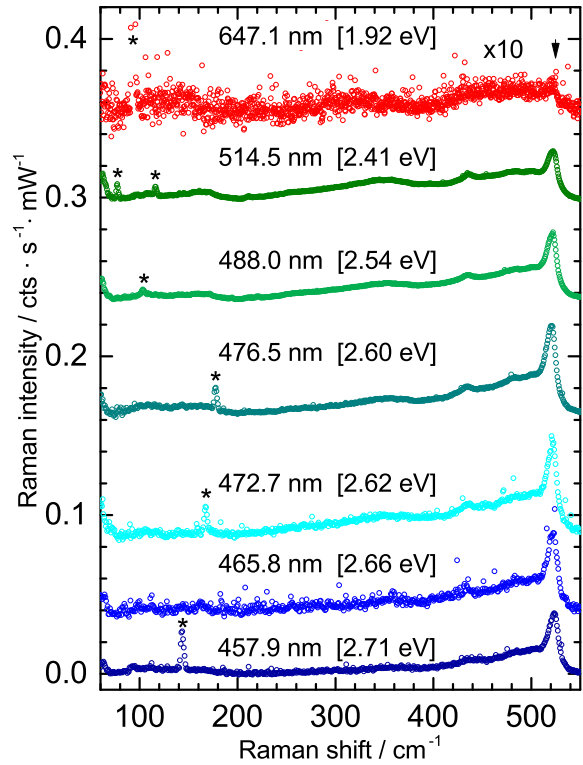
Figure 6.9: Excitation-dependent Raman spectra of the ($\sqrt{3}\times\sqrt{3}$)R30° structure. The Raman intensity is normalized by the power of the particular laser line and the exposure time. The plasma lines are marked with the asterisks.

mode of diamond-like Si is due to a resonance around 2.6 eV. Such behaviour is explained by the upshift of the energy levels in Si nanocrystallites due to the quantum confinement [153]. It is noteworthy that the excitation energy of 1.91 eV, which was shown to match the energy resonance for Si surface states [154], does not lead to the enhancement of the Raman intensity of the Si/Ag(111) system. However, the Raman spectrum recorded under this excitation unexpectedly shows a weak L(T)O mode. The absence of RRS implies another reason for high Raman intensity of the "multi-layer silicene". In this respect it is important to recall that resonance is one of the possible mechanisms for the enhancement. Another one, which can be applied for such samples, is SERS. Indeed, silver is known to host plasmons, which can enhance the Raman signal by the creation of an additional oscillating electric field [155]. Moreover, the range of the plasmon frequencies in silver nanostructures overlays the region of the Ar$^+$ laser lines. The Raman scattering enhancement can originate from the silver islands, which are located below the Si layers.

## Hydrogenation of the Si/Ag(111) system

Finally, the hydrogenation of the "multi-layer silicene" was probed by *in situ* Raman spectroscopy yielding the results, which consistently support its surface-like nature. The
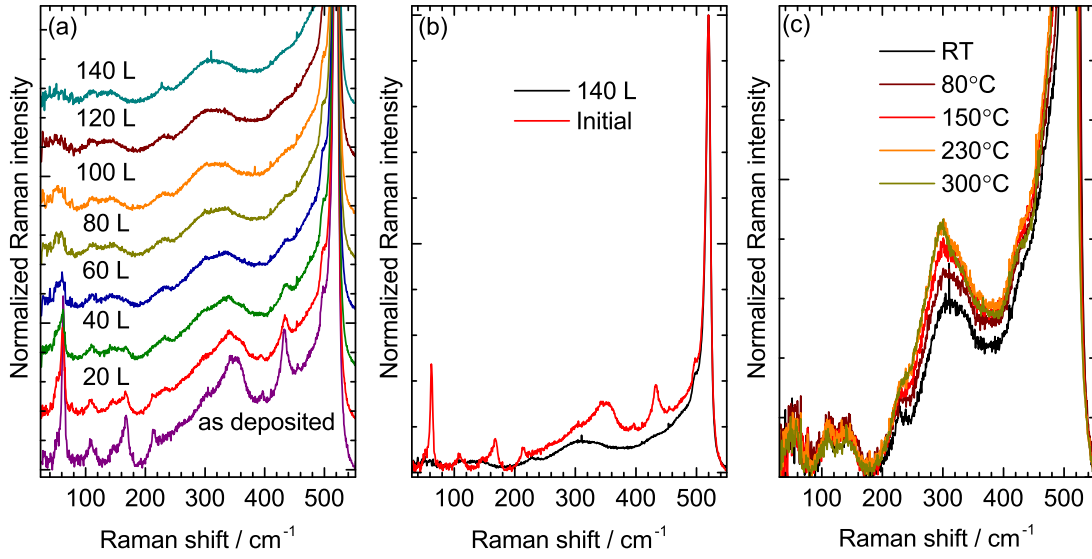
Figure 6.10:  (a) Raman spectra of the ($\sqrt{3}\times\sqrt{3}$)R30° structure within the step-wise hydrogenation. (b) Normalized Raman spectra of pristine ($\sqrt{3}\times\sqrt{3}$)R30° structure and the one after the exposure to 140 L of atomic hydrogen.  (c) Normalized Raman spectra of hydrogenated "multi-layer silicene" recorded during the heating to the elevated temperatures.

hydrogenation of the crystal was carried out in the same fashion explained in the previous chapter. The results are shown in Fig. 6.10(a). It is clear from the Raman spectrum recorded at low hydrogen coverages (20 L, 40 L) that the intensity of the Raman modes, related to the "multi-layer silicene" drops when compared to the one of the pristine layers. The Raman bands of interest almost vanish after a dose of 60 L. Apparently, the highly reactive atomic hydrogen can bind to the silver atoms or etch them. While the only change in the spectra is the intensity drop (no shifts were detected), one can assume that H atoms etch the surface atoms destroying the reconstruction. Hydrogen can easily bind to the Si atoms in a 2D material. At the same time, the interaction of silver and hydrogen can result in a hydride formation (under special conditions [156]), but due to its low stability, it quickly dissociates. Hence, the H atoms take the silver atoms away, reducing the stability of the Si layer underneath. Eventually, this process disrupts the structure of the ($\sqrt{3}\times\sqrt{3}$)R30° phase at the dose of 100 L. Further hydrogenation does not alter the a-Si and c-Si species present on the surface (Fig. 6.10(b)). The residual Raman bands around 110 and 250 cm$^{-1}$ can be related to the amorphidized ($\sqrt{3}\times\sqrt{3}$)R30° structure.  The amorphization of the quasi-2D Si layers can be confirmed by impossibility of its dehydrogenation, which is, on the contrary, possible for epitaxial $(3 \times 3)/(4 \times 4)$ silicene. The corresponding Raman spectra

111

of hydrogenated "multi-layer silicene" recorded at elevated temperatures are shown in Fig. 6.10(c). The annealing of such sample does not lead to the reformation of the spectrum of silicene, but the crystallization of the bulk Si, according to the increase of the Raman intensity of the LA phonon of Si. With this, it can be concluded that the hydrogenation of the Si/Ag(111) system is not successful.

## 6.5 Summary

It this chapter, the Raman signature of the $(\sqrt{3}\times\sqrt{3})$R30° Si structure was revealed. The results of the *in situ* monitoring of its growth suggest its surface-like character. This entirely disagrees with the existing concept of the layered system and proves it wrong. Such interpretation is greatly corraborated by the comparison of the spectral signatures of Si/Ag(111) system with the inverse one, Ag/Si(111). The Raman bands of the latter predominantly match the ones of the $(\sqrt{3}\times\sqrt{3})$R30° Si structure, which allows the conclusion of their common origin, *i.e.* "multi-layer silicene" is a Ag-terminated Si surface. This inference is supported by the *in situ* Raman measurements of the samples upon annealing, ion bombardment, and hydrogenation. Excitation-dependent Raman measurements hint on the absence of any resonant Raman scattering but the presence of the surface Raman enhancement mechanism naturally occurring for Si/Ag(111) system.

# Summary

Silicene is a 2D, one-atom-thin, honeycomb crystal with unique physical and chemical properties, the understanding of which will allow a qualitative leap for microtechnology and other areas and shedding the light onto the exotic phenomena in solid state physics. The synthesis of silicene is based on the epitaxial growth of 2D Si sheets on supporting, predominantly, metallic substrates.

In this work, the growth of epitaxial $(3 \times 3)/(4 \times 4)$ silicene and silicene-related 2D structures on the Ag(111) surface was thoroughly investigated from the perspective of Raman spectroscopy. It is based on the vibrational properties of matter and provides a great tool for the investigation of 2D materials. This method is especially powerful in their identification and monitoring the structural modifications upon the external influence. The vibrational signatures of epitaxial silicene and silicene-related structures were discovered and interpreted. Through the accurate analysis of the Raman spectra, the 2D nature of epitaxial $(3 \times 3)/(4 \times 4)$ silicene was confirmed. Mode assignment based on the mode symmetries was found in an excellent agreement with corresponding DFT calculations. The physical and chemical stability of epitaxial silicene were probed by post-annealing and oxidation and monitored by *in situ* Raman spectroscopy monitoring. This demonstrates the usefulness of Raman scattering as a precise measure of the state of 2D material. The 2D Si structure with the "$(2\sqrt{3}\times2\sqrt{3})$" symmetry was shown to exhibit a Raman mode at $155\,\mathrm{cm}^{-1}$, which is characteristic for the inherent disorder of this structure, while other components of the spectral signature were found identical to the ones of epitaxial silicene. Such partial resemblance of the signatures allowed to interpret the "$(2\sqrt{3}\times2\sqrt{3})$" structure as a defective epitaxial silicene. The co-existence of 2D and 3D Si structures was firstly observed by

Raman spectroscopy results allowing to consistently clarify most of the discrepancies in experimental findings reported previously. The co-formation of 2D layers together with 3D Si nanoparticles at temperatures > 250°C was suggested from the *in situ* Raman measurements and confirmed by *ex situ* AFM measurements. By the combination of Raman results with data obtained by LEED and AFM techniques, the generic phase diagram was suggested showing that certain 2D and 3D Si phases are always co-formed on the Ag(111) surface, which greatly depends on the preparation temperature regime during Si deposition.

The functionalization of epitaxial silicene layers by atomic hydrogen was performed in order to investigate its chemical stability as well as to search for modifications of the electronic structure of hydrogenated silicene, predicted by DFT calculations. *In situ* Raman monitoring clearly showed that the hydrogenation leads to a significant rearrangement of the silicon lattice resulting in the symmetry reduction. The relation of the ratio of the Raman modes to the H dose was suggested. Despite these substantial changes upon hydrogenation, it was shown to be reversible at elevated temperatures around 250°C. Such possibility of alternating low-energy hydrogenation/dehydrogenation makes epitaxial silicene suitable for the hydrogen storage. Excitation-dependent Raman measurements showed a change in the electronic structure of hydrogenated epitaxial silicene, namely a presence of the high-order optical transition, which was not detected for pristine epitaxial silicene. The exposure of other silicene-related structures to atomic hydrogen showed the "template effect", which can explain why the hydrogenation of the inherently disordered "$(2\sqrt{3}\times2\sqrt{3})$" structure produces the irregular hydrogenated 2D layers.

The Raman measurements of the "multi-layer silicene", the Si structure with a $(\sqrt{3}\times\sqrt{3})$R30° symmetry, which forms at above the monolayer coverage, demonstrated the drastic structural differences between mono- and multi-layer sheets. Its spectral signature exhibit a more complex pattern than the one of epitaxial silicene, which is the result of a strong individual interaction between Si and Ag atoms in close vicinity. The co-formation of bulk Si phases such as amorphous and crystalline Si clusters, which was determined by *in situ* Raman monitoring during the growth, becomes more favourable and even dominating at high Si coverages. This, however, does not interfere with the $(\sqrt{3}\times\sqrt{3})$R30° structure, suggesting its surface-like character, which was confirmed by the investigation of its chemical instability. The comparison with the Ag $(\sqrt{3}\times\sqrt{3})$ reconstruction on the Si(111) surface showed that both systems exhibit very similar spectral signatures, from which it was concluded that the "multi-layer silicene" is the Ag-terminated Si surface. On the other hand, its vibrational

properties slightly differ from the ones of the Ag($\sqrt{3} \times \sqrt{3}$)/Si(111) system, which, considering significantly different electronic properties, give a hint on the unique atomic arrangement of this structure, which allows it to share the characteristics of 3D and 2D Si structures.

# Bibliography

[1]  G. E. Moore, IEEE Solid-State Circuits Society Newsletter **11**, 33 (2006).

[2]  L. Landau and E. Lifshitz, *Statistical Physcis. P.1*, vol. 5 (Fizmatlit, 2005), ISBN 5-9221-0054-8.

[3]  A. K. Geim and K. S. Novoselov, Nature Materials **6**, 183 (2007).

[4]  M. Xu, T. Liang, M. Shi, and H. Chen, Chemical Reviews **113**, 3766 (2013).

[5]  T. R. S. A. of Sciences, *The 2010 nobel prize in physics - press release* (2010).

[6]  M. Orlita, C. Faugeras, P. Plochocka, P. Neugebauer, G. Martinez, D. K. Maude, A.-L. Barra, M. Sprinkle, C. Berger, W. A. de Heer, et al., Physical Review Letters **101** (2008).

[7]  Y.-W. Son, M. L. Cohen, and S. G. Louie, Physical Review Letters **97**, 216803 (2006).

[8]  Y. Zhang, T.-T. Tang, C. Girit, Z. Hao, M. C. Martin, A. Zettl, M. F. Crommie, Y. R. Shen, and F. Wang, Nature **459**, 820 (2009).

[9]  F. Schwierz, in *Graphene and beyond: two-dimensional materials for transistor applications*, edited by T. George, A. K. Dutta, and M. S. Islam (2015), p. 94670W.

[10]  B. K. Teo and X. H. Sun, Chemical Reviews **107**, 1454 (2007).

[11]  K. Takeda and K. Shiraishi, Physical Review B **50**, 14916 (1994).

[12]  G. G. Guzman-Verri and L. C. Lew Yan Voon, Physical Review B **76**, 075131 (2007).

[13] S. Cahangirov, M. Topsakal, E. Akturk, H. Sahin, and S. Ciraci, Physical Review Letters **102**, 236804 (2009).

[14] F. P. Bundy, Journal of Geophysical Research **85**, 6930 (1980).

[15] P. Vogt, P. De Padova, C. Quaresima, J. Avila, E. Frantzeskakis, M. C. Asensio, A. Resta, B. Ealet, and G. Le Lay, Physical Review Letters **108**, 155501 (2012).

[16] G. Le Lay, E. Salomon, and T. Angot, Europhysics News **47**, 17 (2016).

[17] M. Houssa, A. Dimoulas, and A. Molle, Journal of Physics: Condensed Matter **27**, 253002 (2015).

[18] N. D. Drummond, V. Zolyomi, and V. I. Fal'ko, Physical Review B **85**, 075423 (2012).

[19] B. Huang, H. J. Xiang, and S.-H. Wei, Physical Review Letters **111**, 145502 (2013).

[20] M. Ezawa, Physical Review Letters **109**, 055502 (2012).

[21] M. Ezawa, New Journal of Physics **14**, 033003 (2012).

[22] M. Ezawa, Physical Review Letters **110**, 026603 (2013).

[23] W.-F. Tsai, C.-Y. Huang, T.-R. Chang, H. Lin, H.-T. Jeng, and A. Bansil, Nature Communications **4**, 1500 (2013).

[24] P. Yu and M. Cardona, *Fundamentals of Semiconductors: Physics and Materials Properties* (Springer Science & Business Media, 2013), ISBN 978-3-662-03848-2.

[25] A. C. Ferrari, Solid State Communications **143**, 47 (2007).

[26] A. Resta, T. Leoni, C. Barth, A. Ranguis, C. Becker, T. Bruhn, P. Vogt, and G. Le Lay, Scientific Reports **3**, 2399 (2013).

[27] S. Cahangirov, V. O. Özçelik, A. Rubio, and S. Ciraci, Physical Review B **90**, 085426 (2014).

[28] P. Vogt, P. Capiod, M. Berthe, A. Resta, P. De Padova, T. Bruhn, G. Le Lay, and B. Grandidier, Applied Physics Letters **104**, 021602 (2014).

[29] K.-G. Zhou, F. Withers, Y. Cao, S. Hu, G. Yu, and C. Casiraghi, ACS Nano **8**, 9914 (2014).

[30] L. C. L. Y. Voon, E. Sandberg, R. S. Aga, and A. A. Farajian, Applied Physics Letters **97**, 163114 (2010).

[31] J. Sivek, H. Sahin, B. Partoens, and F. M. Peeters, Physical Review B **87**, 085444 (2013).

[32] G. van Miert and C. M. Smith, Physical Review B **93**, 035401 (2016).

[33] A. H. Castro Neto, F. Guinea, N. M. R. Peres, K. S. Novoselov, and A. K. Geim, Reviews of Modern Physics **81**, 109 (2009).

[34] L. Pauling, *General Chemistry* (Dover Publications, New York, 1988), 3rd ed., ISBN 978-0-486-65622-9.

[35] C.-L. Lin, R. Arafune, K. Kawahara, N. Tsukahara, E. Minamitani, Y. Kim, N. Takagi, and M. Kawai, Appl. Phys. Express **5**, 045802 (2012).

[36] B. Feng, Z. Ding, S. Meng, Y. Yao, X. He, P. Cheng, L. Chen, and K. Wu, Nano Lett. **12**, 3507 (2012).

[37] A. Fleurence, R. Friedlein, T. Ozaki, H. Kawai, Y. Wang, and Y. Yamada-Takamura, Phys. Rev. Lett. **108**, 245501 (2012).

[38] L. Meng, Y. Wang, L. Zhang, S. Du, R. Wu, L. Li, Y. Zhang, G. Li, H. Zhou, W. A. Hofer, et al., Nano Lett. **13**, 685 (2013).

[39] Z.-L. Liu, M.-X. Wang, C. Liu, J.-F. Jia, P. Vogt, C. Quaresima, C. Ottaviani, B. Olivieri, P. D. Padova, and G. L. Lay, APL Materials **2**, 092513 (2014).

[40] H. Liu, J. Gao, and J. Zhao, The Journal of Physical Chemistry C **117**, 10353 (2013).

[41] F. Bao-Jie, L. Wen-Bin, Q. Jing-Lan, C. Peng, C. Lan, and W. Ke-Hui, Chinese Physics Letters **32**, 037302 (2015).

[42] Z. Li, H. Feng, J. Zhuang, N. Pu, L. Wang, X. Xu, W. Hao, and Y. Du, Journal of Physics: Condensed Matter **28**, 034002 (2016).

[43] M. J. Allen, V. C. Tung, and R. B. Kaner, Chemical Reviews **110**, 132 (2010).

[44] P. Pflugradt, L. Matthes, and F. Bechstedt, Physical Review B **89**, 035403 (2014).

[45] Calculated with C2PK and QUANTUM ESPRESSO., URL `https://www.cp2k.org/exercises:2015_ethz_mmm:bs`.

[46] W. Humphrey, A. Dalke, and K. Schulten, Journal of Molecular Graphics **14**, 33 (1996).

[47] C.-L. Lin, R. Arafune, K. Kawahara, M. Kanno, N. Tsukahara, E. Minamitani, Y. Kim, M. Kawai, and N. Takagi, Physical Review Letters **110**, 076801 (2013).

[48] N. W. Johnson, P. Vogt, A. Resta, P. De Padova, I. Perez, D. Muir, E. Z. Kurmaev, G. Le Lay, and A. Moewes, Advanced Functional Materials **24**, 5253 (2014).

[49] S. Cahangirov, M. Audiffred, P. Tang, A. Iacomino, W. Duan, G. Merino, and A. Rubio, Physical Review B **88**, 035432 (2013).

[50] M. Satta, S. Colonna, R. Flammini, A. Cricenti, and F. Ronci, Physical Review Letters **115**, 026102 (2015).

[51] M. X. Chen, Z. Zhong, and M. Weinert, Physical Review B **94**, 075409 (2016).

[52] E. Scalise, M. Houssa, G. Pourtois, B. van den Broek, V. Afanas'ev, and A. Stesmans, Nano Research **6**, 19 (2013).

[53] X. Li, J. T. Mullen, Z. Jin, K. M. Borysenko, M. Buongiorno Nardelli, and K. W. Kim, Physical Review B **87**, 115418 (2013).

[54] D. Solonenko, O. D. Gordan, G. L. Lay, H. Şahin, S. Cahangirov, D. R. T. Zahn, and Patrick Vogt, 2D Materials **4**, 015008 (2017).

[55] G. Nilsson and G. Nelin, Physical Review B **6**, 3777 (1972).

[56] J. Maultzsch, S. Reich, C. Thomsen, H. Requardt, and P. Ordejón, Physical Review Letters **92**, 075501 (2004).

[57] M. Mohr, J. Maultzsch, E. Dobardžić, S. Reich, I. Milošević, M. Damnjanović, A. Bosak, M. Krisch, and C. Thomsen, Physical Review B **76**, 035439 (2007).

[58] R. Fei and L. Yang, Applied Physics Letters **105**, 083120 (2014).

[59] W. Kohn, Physical Review Letters **2**, 393 (1959).

[60] S. Piscanec, M. Lazzeri, F. Mauri, A. C. Ferrari, and J. Robertson, Physical Review Letters **93**, 185503 (2004).

[61] Z.-L. Liu, M.-X. Wang, J.-P. Xu, J.-F. Ge, G. L. Lay, P. Vogt, D. Qian, C.-L. Gao, C. Liu, and J.-F. Jia, New Journal of Physics **16**, 075006 (2014).

[62] P. Moras, T. O. Mentes, P. M. Sheverdyaeva, A. Locatelli, and C. Carbone, Journal of Physics: Condensed Matter **26**, 185001 (2014).

[63] D. Solonenko, O. D. Gordan, G. L. Lay, H. Şahin, S. Cahangirov, D. R. T. Zahn, and P. Vogt (2017), unpublished.

[64] R. Arafune, C.-L. Lin, K. Kawahara, N. Tsukahara, E. Minamitani, Y. Kim, N. Takagi, and M. Kawai, Surface Science **608**, 297 (2013).

[65] H. Jamgotchian, Y. Colignon, B. Ealet, B. Parditka, J.-Y. Hoarau, Christophe Girardeaux, B. Aufray, and J.-P. Bibérian, Journal of Physics: Conference Series **491**, 012001 (2014).

[66] H. Liu, H. Feng, Y. Du, J. Chen, K. Wu, and J. Zhao, arXiv:1512.08860 [cond-mat] (2015), arXiv: 1512.08860.

[67] P. D. Padova, P. Vogt, A. Resta, J. Avila, I. Razado-Colambo, C. Quaresima, C. Ottaviani, B. Olivieri, T. Bruhn, T. Hirahara, et al., Applied Physics Letters **102**, 163106 (2013).

[68] E. Salomon, R. E. Ajjouri, G. L. Lay, and T. Angot, Journal of Physics: Condensed Matter **26**, 185003 (2014).

[69] S. Cahangirov, V. O. Özçelik, L. Xian, J. Avila, S. Cho, M. C. Asensio, S. Ciraci, and A. Rubio, Physical Review B **90**, 035448 (2014).

[70] P. Pflugradt, L. Matthes, and F. Bechstedt, Physical Review B **89**, 205428 (2014).

[71] H. Fu, J. Zhang, Z. Ding, H. Li, and S. Meng, Applied Physics Letters **104**, 131904 (2014).

[72] A. J. Mannix, B. Kiraly, B. L. Fisher, M. C. Hersam, and N. P. Guisinger, ACS Nano **8**, 7538 (2014).

[73] T. Shirai, T. Shirasawa, T. Hirahara, N. Fukui, T. Takahashi, and S. Hasegawa, Physical Review B **89**, 241403(R) (2014).

[74] G.-W. Lee, H.-D. Chen, and D.-S. Lin, Applied Surface Science **354, Part A**, 212 (2015).

[75] K. Kawahara, T. Shirasawa, C.-L. Lin, R. Nagao, N. Tsukahara, T. Takahashi, R. Arafune, M. Kawai, and N. Takagi, Surface Science **651**, 70 (2016).

[76] C.-L. Lin, T. Hagino, Y. Ito, K. Kawahara, R. Nagao, M. Aoki, S. Masuda, R. Arafune, M. Kawai, and N. Takagi, The Journal of Physical Chemistry C **120**, 6689 (2016).

[77] W. Mönch, *Semiconductor Surfaces and Interfaces* (Springer, Berlin ; New York, 2001), 3rd ed., ISBN 978-3-540-67902-8.

[78] Y. Borensztein, A. Curcella, S. Royer, and G. Prévot, Physical Review B **92**, 155407 (2015).

[79] N. W. Johnson, D. Muir, E. Z. Kurmaev, and A. Moewes, Advanced Functional Materials **25**, 4083 (2015).

[80] P. De Padova, A. Generosi, B. Paci, C. Ottaviani, C. Quaresima, B. Olivieri, E. Salomon, T. Angot, and G. L. Lay, arXiv preprint arXiv:1606.05919 (2016).

[81] P. D. Padova, J. Avila, A. Resta, I. Razado-Colambo, C. Quaresima, C. Ottaviani, Bruno Olivieri, T. Bruhn, P. Vogt, M. C. Asensio, et al., Journal of Physics: Condensed Matter **25**, 382202 (2013).

[82] L. Brillouin, Annales de Physique **9**, 88 (1922).

[83] C. V. Raman, Nature **121**, 619 (1928).

[84] G. Rajan, *Optical Fiber Sensors: Advanced Techniques and Applications* (CRC Press, 2015), ISBN 978-1-4822-2829-8.

[85] D. A. Long, *The Raman effect: a unified treatment of the theory of Raman scattering by molecules* (Wiley, Chichester ; New York, 2002), ISBN 978-0-471-49028-9.

[86] E. Smith and G. Dent, *Modern Raman spectroscopy: a practical approach* (J. Wiley, Hoboken, NJ, 2005), ISBN 978-0-471-49668-7 978-0-471-49794-3.

[87] L. Landau and E. Lifshitz, *Field theory*, vol. 2 (Fizmatlit, 2003), ISBN 5-9221-0056-4.

[88] R. C. Powell, *Symmetry, Group Theory, and the Physical Properties of Crystals*, vol. 824 of *Lecture Notes in Physics* (Springer New York, New York, NY, 2010), ISBN 978-1-4419-7597-3 978-1-4419-7598-0.

[89] T. C. Damen, S. P. S. Porto, and B. Tell, Physical Review **142**, 570 (1966).

[90] I. Horcas, R. Fernandez, J. M. Gomez-Rodriguez, J. Colchero, J. Gomez-Herrero, and A. M. Baro, Review of Scientific Instruments **78**, 013705 (2007).

[91] J. M. Walls, *Methods of Surface Analysis: Techniques and Applications* (CUP Archive, 1990), ISBN 978-0-521-38690-6.

[92] N. W. Ashcroft and N. D. Mermin, *Solid state physics* (Holt, Rinehart and Winston, New York, 1976), ISBN 978-0-03-083993-1.

[93] G. Prévot, R. Bernard, H. Cruguel, and Y. Borensztein, Applied Physics Letters **105**, 213106 (2014).

[94] T. Ishidate, K. Inoue, K. Tsuji, and S. Minomura, Solid State Communications **42**, 197 (1982).

[95] Z. Iqbal and S. Veprek, Journal of Physics C: Solid State Physics **15**, 377 (1982).

[96] X. L. Wu, G. G. Siu, S. Tong, X. N. Liu, F. Yan, S. S. Jiang, X. K. Zhang, and D. Feng, Applied Physics Letters **69**, 523 (1996).

[97] X. Xu, J. Zhuang, Y. Du, H. Feng, N. Zhang, C. Liu, T. Lei, J. Wang, M. Spencer, T. Morishita, et al., Scientific Reports **4**, 7543 (2014).

[98] A. G. Silva, K. Pedersen, Z. S. Li, and P. Morgen, Thin Solid Films **520**, 697 (2011).

[99] J. F. Allison, D. J. Dumin, F. P. Heiman, C. W. Mueller, and P. H. Robinson, Proceedings of the IEEE **57**, 1490 (1969).

[100] T. J. Konno and R. Sinclair, Philosophical Magazine Part B **71**, 163 (1995).

[101] C. Zhang and C. W. Bates Jr., Thin Solid Films **517**, 5783 (2009).

[102] A. Acun, B. Poelsema, H. J. W. Zandvliet, and R. v. Gastel, Applied Physics Letters **103**, 263119 (2013).

[103] H. Jamgotchian, B. Ealet, Y. Colignon, H. Maradj, J.-Y. Hoarau, J.-P. Biberian, and B. Aufray, Journal of Physics: Condensed Matter **27**, 395002 (2015).

[104] N. W. Johnson, D. I. Muir, and A. Moewes, Scientific Reports **6**, 22510 (2016).

[105] E. Cinquanta, E. Scalise, D. Chiappe, C. Grazianetti, B. van den Broek, M. Houssa, M. Fanciulli, and A. Molle, The Journal of Physical Chemistry C **117**, 16719 (2013).

[106] J. Zhuang, X. Xu, Y. Du, K. Wu, L. Chen, W. Hao, J. Wang, W. K. Yeoh, X. Wang, and S. X. Dou, Physical Review B **91**, 161409(R) (2015).

[107] H. Richter, Z. P. Wang, and L. Ley, Solid State Communications **39**, 625 (1981).

[108] J. Menéndez and M. Cardona, Physical Review B **29**, 2051 (1984).

[109] J.-A. Yan, R. Stein, D. M. Schaefer, X.-Q. Wang, and M. Y. Chou, Physical Review B **88**, 121403(R) (2013).

[110] P. Gori, O. Pulci, R. d. L. Vollaro, and C. Guattari, Energy Procedia **45**, 512 (2014).

[111] J. Ribeiro-Soares, R. M. Almeida, L. G. Cançado, M. S. Dresselhaus, and A. Jorio, Physical Review B **91**, 205421 (2015).

[112] S.-H. Chou, A. J. Freeman, S. Grigoras, T. M. Gentle, B. Delley, and E. Wimmer, The Journal of Chemical Physics **89**, 5177 (1988).

[113] I. Calizo, A. A. Balandin, W. Bao, F. Miao, and C. N. Lau, Nano Letters **7**, 2645 (2007).

[114] S. Sahoo, A. P. S. Gaur, M. Ahmadi, M. J.-F. Guinel, and R. S. Katiyar, The Journal of Physical Chemistry C **117**, 9042 (2013).

[115] T. R. Hart, R. L. Aggarwal, and B. Lax, Physical Review B **1**, 638 (1970).

[116] G. R. Berdiyorov and F. M. Peeters, **4**, 1133 (2013).

[117] I. H. Campbell and P. M. Fauchet, Solid State Communications **58**, 739 (1986).

[118] A. Molle, C. Grazianetti, D. Chiappe, E. Cinquanta, E. Cianci, G. Tallarida, and M. Fanciulli, Advanced Functional Materials **23**, 4340 (2013).

[119] L. Tao, E. Cinquanta, D. Chiappe, C. Grazianetti, M. Fanciulli, M. Dubey, A. Molle, and D. Akinwande, Nature Nanotechnology **10**, 227 (2015).

[120] S. Périchon, V. Lysenko, B. Remaki, D. Barbier, and B. Champagnon, Journal of Applied Physics **86**, 4700 (1999).

[121] P. Mishra and K. P. Jain, Physical Review B **62**, 14790 (2000).

[122] P. Mishra and K. P. Jain, Physical Review B **64**, 073304 (2001).

[123] M. Lazzeri, S. Piscanec, F. Mauri, A. C. Ferrari, and J. Robertson, Physical Review B **73**, 155426 (2006).

[124] W. Wan, Y. Ge, F. Yang, and Y. Yao, EPL (Europhysics Letters) **104**, 36001 (2013).

[125] H. Jamgotchian, Y. Colignon, N. Hamzaoui, B. Ealet, J. Y. Hoarau, B. Aufray, and J. P. Bibérian, Journal of Physics: Condensed Matter **24**, 172001 (2012).

[126] E. Cinquanta, G. Fratesi, S. dal Conte, C. Grazianetti, F. Scotognella, S. Stagira, C. Vozzi, G. Onida, and A. Molle, Physical Review B **92**, 165427 (2015).

[127] T. H. Osborn, A. A. Farajian, O. V. Pupysheva, R. S. Aga, and L. C. Lew Yan Voon, Chemical Physics Letters **511**, 101 (2011).

[128] M. Houssa, E. Scalise, K. Sankaran, G. Pourtois, V. V. Afanas'ev, and A. Stesmans, Applied Physics Letters **98**, 223107 (2011).

[129] S.-Y. Lin, S.-L. Chang, N. T. T. Tran, P.-H. Yang, and M.-F. Lin, Physical Chemistry Chemical Physics **17**, 26443 (2015).

[130] P. Zhang, X. D. Li, C. H. Hu, S. Q. Wu, and Z. Z. Zhu, Physics Letters A **376**, 1230 (2012).

[131] J. Qiu, H. Fu, Y. Xu, A. Oreshkin, T. Shao, H. Li, S. Meng, L. Chen, and K. Wu, Physical Review Letters **114**, 126101 (2015).

[132] Y. Kumai, S. Shirai, E. Sudo, J. Seki, H. Okamoto, Y. Sugiyama, and H. Nakano, Journal of Power Sources **196**, 1503 (2011).

[133] P. Vora, S. A. Solin, and P. John, Physical Review B **29**, 3423 (1984).

[134] M. Cardona, physica status solidi (b) **118**, 463 (1983).

[135] C. Stuhlmann, G. Bogdanyi, and H. Ibach, Physical Review B **45**, 6786 (1992).

[136] D. H. Sahin and D. S. Cahangirov (2016), private communication.

[137] Q. G. Jiang, W. C. Wu, J. F. Zhang, Z. M. Ao, Y. P. Wu, and H. J. Huang, RSC Adv. **6**, 69861 (2016).

[138] G. Liu, X. L. Lei, M. S. Wu, B. Xu, and C. Y. Ouyang, Journal of Physics: Condensed Matter **26**, 355007 (2014).

[139] V. Zolyomi, J. R. Wallbank, and V. I. Fal'ko, 2D Materials **1**, 011005 (2014).

[140] W. Wang, W. Olovsson, and R. I. G. Uhrberg, Physical Review B **93**, 081406 (2016).

[141] P. De Padova, C. Ottaviani, C. Quaresima, B. Olivieri, P. Imperatori, E. Salomon, T. Angot, L. Quagliano, C. Romano, A. Vona, et al., 2D Materials **1**, 021003 (2014).

[142] Y. Du, J. Zhuang, J. Wang, Z. Li, H. Liu, J. Zhao, X. Xu, H. Feng, L. Chen, K. Wu, et al., Science Advances **2**, e1600067 (2016).

[143] M. Liebhaber, U. Bass, P. Bayersdorfer, J. Geurts, E. Speiser, J. Räthel, A. Baumann, S. Chandola, and N. Esser, Physical Review B **89**, 045313 (2014).

[144] W. M. Telford, L. P. Geldart, and R. E. Sheriff, *Applied Geophysics* (Cambridge University Press, 1990), ISBN 978-0-521-33938-4.

[145] C. T. Chan, K. M. Ho, and K. P. Bohnen, in *Handbook of Surface Science*, edited by W. N. Unertl (North-Holland, 1996), vol. 1 of *Physical Structure*, pp. 101–136.

[146] L. Chen, H. Li, B. Feng, Z. Ding, J. Qiu, P. Cheng, K. Wu, and S. Meng, Physical Review Letters **110** (2013).

[147] J. Liu and W. Zhang, RSC Advances **3**, 21943 (2013).

[148] B. Huang, H.-X. Deng, H. Lee, M. Yoon, B. G. Sumpter, F. Liu, S. C. Smith, and S.-H. Wei, Physical Review X **4**, 021029 (2014).

126

[149] Z.-X. Guo and A. Oshiyama, Physical Review B **89**, 155418 (2014).

[150] B. Bishnoi and B. Ghosh, Computational Materials Science **85**, 16 (2014).

[151] A. C. Ferrari and D. M. Basko, Nature Nanotechnology **8**, 235 (2013).

[152] M. M. Lucchese, F. Stavale, E. H. M. Ferreira, C. Vilani, M. V. O. Moutinho, R. B. Capaz, C. A. Achete, and A. Jorio, Carbon **48**, 1592 (2010).

[153] S. Öğüt, J. R. Chelikowsky, and S. G. Louie, Physical Review Letters **79**, 1770 (1997).

[154] S. Wippermann and W. G. Schmidt, Surface Science **603**, 247 (2009).

[155] S. Schlücker, Angewandte Chemie International Edition **53**, 4756 (2014).

[156] E. Pietsch and F. Seuferling, Naturwissenschaften **19**, 573 (1931).

# Acknowledgements

# Lebenslauf

## Dmytro Ihorovych Solonenko

*Education*

**since November 2013**  PhD candidate
Insitute of Physics, Chemnitz University of Technology, Chemnitz, Germany.

**September 2011 – June 2013**  Master of Science (M.Sc.)
Theoretical and Mathematical Physics, National University of "Kyiv-Mohyla Academy", Kyiv, Ukraine.

Thesis: *Spectral Properties and Application of Ultrasmall Nanoparticles CdS and CdSe.*

**September 2009 – June 2011**  Bachelor (minor)
Biology/Biological Sciences, National University of "Kyiv-Mohyla Academy", Kyiv, Ukraine.

**September 2007 – June 2011**  Bachelor of Science (B.Sc.)
Physics, National University of "Kyiv-Mohyla Academy", Kyiv, Ukraine.

Thesis: *Photoluminescence of Colloidal Nanoparticles ZnO in Polymeric Matrix.*

**September 1999 - June 2007**  Secondary education
City Liceum, Zhytomyr, Ukraine.

*Experience*

**November 2013 – Present**  Scientific Employee

Semiconductor Physics group, Institute of Physics, Chemnitz University of Technology, Chemnitz, Germany.

**July 2013 – September 2013**  Guest Researcher

Semiconductor Physics group, Institute of Physics, Chemnitz University of Technology, Chemnitz, Germany.

**June 2012 – June 2013**  Engineer

Photochemistry group, Institute of Physical Chemistry NAS of Ukraine, Kyiv, Ukraine.

**September 2011 – May 2012**  Trainee

Photochemistry group, Institute of Physical Chemistry NAS of Ukraine, Kyiv, Ukraine.

*Awards*

- Best oral presentation at 65$^{\text{th}}$ Course "Epioptics XIII - Silicene I" of the International School of Solid State Physics in Erice, Italy.

# Publications

[1] D. Solonenko, O. D. Gordan, G. L. Lay, H. Sahin, S. Cahangirov, D. R. T. Zahn, and P. Vogt. 2D vibrational properties of epitaxial silicene on Ag(111). *2D Materials*, 4(1): 015008, 2017.

[2] D. Solonenko, O. D. Gordan, A. Milekhin, M. Panholzer, K. Hingerl, and D. R. T. Zahn. Interference-enhanced Raman scattering of F 16 CuPc thin films. *Journal of Physics D: Applied Physics*, 49(11):115502, 2016.

[3] A. E. Raevskaya, O. L. Stroyuk, Ya. V. Panasiuk, V. M. Dzhagan, D. I. Solonenko, S. Schulze, and D. R. T. Zahn. A new route to very stable water-soluble ultra-small core/shell CdSe/CdS quantum dots. *Nano-Structures & Nano-Objects*, 2016. doi: 10.1016/j.nanoso.2015.12.001.

[4] A. E. Raevskaya, O. L. Stroyuk, D. I. Solonenko, V. M. Dzhagan, D. Lehmann, S. Ya Kuchmiy, V. F. Plyusnin, and D. R. T. Zahn. Synthesis and luminescent properties of ultrasmall colloidal CdS nanoparticles stabilized by Cd(II) complexes with ammonia and mercaptoacetate. *Journal of Nanoparticle Research*, 16(10):1–10, September 2014.

[5] V. M. Dzhagan, M. Ya. Valakh, C. Himcinschi, A. G. Milekhin, D. Solonenko, N. A. Yerukov, A. E. Raevskaya, O. L. Stroyuk, and D. R. T. Zahn. Raman and Infrared Phonon Spectra of Ultrasmall Colloidal CdS Nanoparticles. *The Journal of Physical Chemistry C*, 118(33):19492–19497, August 2014.